UNIVERSITÀ DEGLI STUDI DI MODENA E REGGIO

EMILIA

DIPARTIMENTO DI INGEGNERIA “ENZO FERRARI"

PhD SCHOOL

Industrial and Environmental Engineering

Ingegneria Industriale e del Territorio

XXXVII CYCLE

Three-Dimensional CFD Modelling of PEM Fuel Cells and Electrolyzers

Advisor:

Prof. Alessandro d’Adamo

Candidate:

Giuseppe Corda

PhD School Director:

Prof. Alberto Muscio

Abstract

Polymer Electrolyte Membrane Fuel Cells (PEMFCs) have emerged over the past two decades as a highly promising technology for clean energy conversion, attracting significant attention in automotive and micro-cogeneration sectors. Their appeal lies in attributes such as high efficiency and power density, low emissions, relatively low operating temperatures (below 100 °C), rapid start-up capabilities, and modularity. These advantages position PEMFCs as key components in the transition toward sustainable energy systems. However, challenges persist, notably in water management, which critically impacts performance and durability by affecting membrane hydration and overall cell efficiency.

This thesis presents a comprehensive study aimed at enhancing the understanding and modelling of PEM fuel cells and electrolyzers through detailed three-dimensional numerical simulations. The research begins with an in-depth examination of the state of the art in fuel cells, focusing on their components—such as the polymer electrolyte membrane, catalyst layers, gas diffusion layers, and bipolar plates—and the materials used in their construction. Understanding the roles and interactions of these components is crucial for identifying factors that influence performance and for guiding the development of effective modelling approaches.

Building on this foundation, the study explores various modelling techniques applicable to the simulation of these devices, including multiphase models and electrochemical models. Multiphase models account for the simultaneous presence of gas and liquid phases within the cell, essential for accurately representing water/gas transport and distribution. Electrochemical models describe the reactions at the electrodes, incorporating kinetics, mass transport, and charge conservation principles. These models are vital for capturing the complex physical and chemical processes occurring within PEM fuel cells and electrolyzers.

The core of the research involves applying selected modelling approaches to a single-channel PEM fuel cell case from existing literature. Three-dimensional Computational Fluid Dynamics (CFD) simulations are conducted, with results validated against

experimental data to ensure accuracy and reliability. A key aspect investigated is the effect of porous media compression resulting from the assembly phase. Compression of the gas diffusion layers and catalyst layers during assembly alters their physical properties, such as porosity and permeability, affecting reactant distribution and overall cell performance. By incorporating strain correlations from the literature into the simulations, the study examines how mechanical deformation impacts the behavior of the porous media and, consequently, the fuel cell's efficiency.

An additional focus is placed on the thermal management of a full-scale PEM fuel cell and its impact on performance. Effective thermal management is essential for maintaining optimal operating temperatures, which influence reaction kinetics, membrane hydration, and overall system efficiency. This study integrates thermal modelling to assess heat generation and dissipation within the cell, evaluating the influence of various cooling strategies and thermal conductivities of cell components. Results highlight the critical role of thermal management in enhancing the performance and durability of real-scale fuel cells, offering insights into design improvements for future applications.

Extending the modelling approach, the research simulates a full cell of a PEM electrolyzer based on literature sources. Numerical results are compared with experimental findings from the original studies, providing deeper insights into the performance and modelling aspects of these devices. The simulations highlight critical factors affecting electrolyzer efficiency, such as gas evolution dynamics and mass transport limitations, enhancing our understanding of how to optimize these systems for hydrogen production.

The insights gained can inform future efforts to optimize device performance, reduce costs, and promote the wider adoption of PEM technologies in the pursuit of global energy sustainability.

Keywords: Polymer Electrolyte Membrane Fuel Cell, PEM Electrolyzer, Water Management, Computational Fluid Dynamics, Performance Optimization

Summary

***Index* of Figures**

Index of Tables

1 Introduction[1]

1.1 Polymer Electrolyte Membrane Fuel Cell

Polymer electrolyte membrane fuel cells (PEMFCs) represent a highly efficient class of electrochemical devices that facilitate the direct conversion of reactant chemical energy into electrical energy. The operation of PEMFCs involves simultaneous redox reactions taking place at the anode and cathode. At the anode, the fuel undergoes oxidation, releasing electrons that are subsequently transferred to the cathode through an external circuit. Reduction reactions occur at the cathode, leading to the generation of electric current and enabling the efficient conversion of chemical energy into usable electrical power.

Compared to traditional energy conversion systems, fuel cells offer a multitude of advantages. Their direct collection and conversion of electrons from chemical reactions eliminate the need for intermediate steps such as heat exchange or mechanical work, resulting in high energy conversion efficiencies. This characteristic positions fuel cells as attractive alternatives to conventional internal combustion and steam engines. Moreover, fuel cells operate with minimal to no pollutant emissions, thereby offering a clean and environmentally friendly solution to combat the pollution challenges faced by contemporary industries.

Among various types of fuel cells, polymer electrolyte membrane fuel cells (PEMFC) have garnered significant attention due to their unique attributes. PEMFCs exhibit quick start-up capabilities, enabling prompt power generation when required. Additionally, they possess high power density, allowing for the delivery of substantial electrical output within compact systems. These features are particularly advantageous for applications with space and weight constraints, making PEMFCs viable power sources for portable and mobile devices. Furthermore, PEMFCs demonstrate rapid response to load changes, rendering them suitable for applications characterized by dynamic power demands. The low operating temperature of PEMFCs further enhances their versatility, ensuring safer

[1] Note to the reader: unless otherwise stated, the main reference source is [1] Barbir, F. PEM Fuel Cells, Theory and practice. s.l.. : Elsevier, 2005

operation and facilitating integration into diverse systems. The modularity and system robustness of PEMFCs contribute to their reliability and scalability, supporting their use in transportation, stationary power generation, and portable applications.

In summary, PEMFCs, with their efficient electrochemical conversion, minimal emissions, and distinct operational characteristics, hold tremendous promise for a wide range of energy applications. This introduction highlights the key features and advantages of PEMFCs, positioning them as a compelling choice for next-generation power sources.

1.1.1 Components

In *Figure 1*Figure 1Figure 1Figure 1Figure 1, the schematic picture of a PEM fuel cell is illustrated. At the heart of this device lies the polymer membrane. This membrane plays a crucial role in enabling the transport of protons (H+) and water while effectively blocking the passage of electrons and gas species. Positioned between the anode and cathode, it enables the functioning of the fuel cell.

The anode catalyst layer (CLa), located on one side, serves as the site for the oxidation reaction, while the cathode catalyst layer (CLc), on the other side, catalyzes the reduction reaction. These electrodes are in direct contact with a diffusive layer known as the Gas Diffusion Layer (GDL). The GDL, with its porous structure, allows for the diffusion of reactants to reach the catalytic sites while also providing the necessary electrical connectivity to the bipolar plates.

The bipolar plates are solid components, whose primary purpose is to enable the series connection of multiple cells within the fuel cell stack. Additionally, they are engineered to create a well-defined pathway for the reactant gases, ensuring their efficient flow throughout the cell.

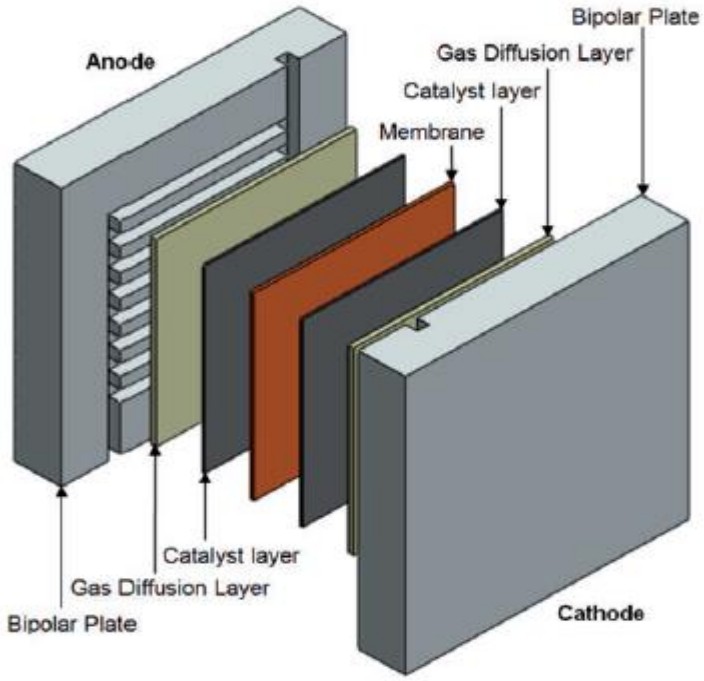

Figure 1 – Fuel Cell components

- Membrane

A PEMFC membrane needs to possess certain characteristics to function effectively in a fuel cell environment. These include high proton conductivity, acting as a barrier against gaseous species, and exhibiting chemical and mechanical stability. Perfluorocarbonsulfonic acid (PSA) ionomer, typically composed of tetrafluoroethylene (TFE) and various perfluorosulfonate monomers, is commonly used as the membrane material in PEM fuel cells. Nafion, developed by Dupont, is a well-known example of such a membrane and utilizes perfluorosulfonylfluoride ethyl-propyl-vinyl ether (PSEPVE). The chemical structure of a perfluorosulfonate ionomer like Nafion is depicted in *Figure 2*.

The ionically bonded SO_3H group in the membrane's side chain consists of an SO_3^- ion and an H^+ ion, giving rise to the term "ionomer" for this type of structure. Due to their ionic nature, the ends of the side chains tend to form clusters within the overall membrane structure. Although the Teflon-like backbone is highly hydrophobic, the sulphonic acid at

the end of the side chain is strongly hydrophilic. This results in the creation of hydrophilic regions around the clusters of sulphonated side chains. Consequently, these materials have a relatively high-water absorption capacity (up to 50% by weight in some cases). The movement of H^+ ions within well-hydrated regions enables these materials to exhibit proton conductivity.

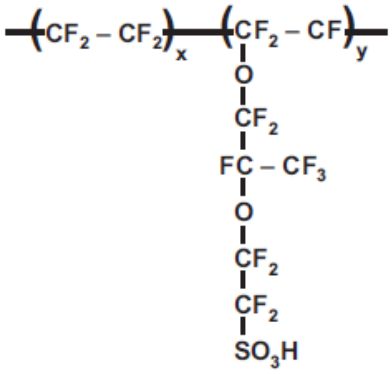

Figure 2 - Chemical structure of a perfluorosulfonate ionomer.

- Catalyst Layer

The CL is located between the diffusion layer and the membrane. This component acts as a porous medium with a thickness of several tens of microns. It is the site where electrochemical reactions take place. The generated current in the fuel cell directly depends on the speed of the electrochemical reactions, which can produce high current if fast or lower current if slower. To increase the speed and efficiency of the electrochemical reactions, a catalyst is used. These reactions occur at the triple phase boundary, which refers to the interface where oxygen, H^+ ions, and electrons e^- are simultaneously available in the presence of the catalyst. The catalyst, composed of platinum nanoparticles dispersed on a carbon-based support, acts as the active phase for the electrochemical reactions. Its role is to decrease the activation energy barrier for half-cell reactions and increase the overall rate of conversion of reactants into products, thereby improving performance. Electrons are conducted to or from the GDL through the solid carbon matrix, while positive ions can travel to or from the membrane through the ionomer fibers. The empty pore space in this domain is quite limited and serves as a pathway for reactant flow.

- Gas Diffusion Layer

The GDL is located between the bipolar plate and the catalyst layer and is a porous medium several hundred microns thick. Its primary function is to establish a connection between the channel and the CL, enabling the flow of reactants and products of electrochemical reactions in both directions. Additionally, it plays a crucial role in allowing electrical connectivity between the BP and the CL, ensuring the passage of electrons to the external circuit. Furthermore, the gas diffusion layer assists in conducting the heat generated during electrochemical reactions from the CL to the BP.

To fulfil these functions effectively, the gas diffusion layer must exhibit sufficient porosity to accommodate the flow of both reactant gases and product water, even though these fluxes move in opposite directions. Both through-plane and in-plane diffusion are important, depending on the flow field design. In addition, the gas diffusion layer must possess good electrical and thermal conductivity in both the in-plane and through-plane directions, with minimal interfacial or contact resistance. The pore size of the GDL facing the CL should be appropriately controlled due to the discrete nature of the CL composed of small particles.

The GDL should strike a balance between rigidity to support the MEA (Membrane Electrode Assembly) effectively and flexibility to maintain good electrical contacts. Carbon-fiber materials, such as carbon fiber papers and carbon fabrics, are particularly well-suited to meet these somewhat conflicting requirements and are commonly employed in this role.

In *Figure 3* are reported two different GDL fabrication types.

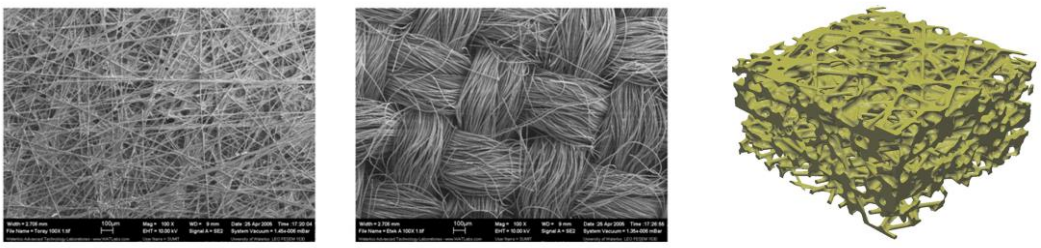

Figure 3 - Two different GDL fabrication types: (a) carbon paper (Toray 090) and (b) woven carbon cloth (E-Tek Cloth "A"). (c) Reconstructed 3D view of GDL structure of uncompressed carbon paper using phase contrast tomographic microscopy. [2]

- Bipolar Plates

The Bipolar Plates electrically connect the anode of one cell to the cathode of the adjacent cell. This component serves to electrically connect the cells in series, separate the gases of neighboring cells, provide structural support, enable the dissipation of thermal power generated by the cell during operation, and ensure the most uniform distribution of reactants possible. The latter requirement is fulfilled by the flow field pattern created on the bipolar plate, which can take various forms. Given the functions this component must fulfill, it is necessary for the material used in its production to be electrically and thermally conductive, resistant, lightweight, cost-effective, easily workable, and corrosion-resistant. Lightweight is particularly desirable in transportation applications, where an increase in weight impacts the overall efficiency of the system. One of the early choices for bipolar plates in PEM fuel cells was graphite due to its chemical stability. However, its inherent porosity required impregnation to make it impermeable, which increased complexity and cost. Metallic plates are also used but require protective coatings to resist corrosion. Carbon composite plates, made with thermoplastics or thermoset resins, offer stability but may have leaching issues. The choice of materials and manufacturing processes must consider properties such as conductivity, tolerances, warping, and skinning effect. Graphite/composite plates exhibit excellent chemical stability but are bulkier and more brittle compared to metallic plates. Though their conductivity is lower, the resistive losses are manageable.

A typical BP is shown in *Figure 4*.

Figure 4 - Bipolar Plates with flow channels.

1.1.2 Working principles

A polymer electrolyte membrane fuel cell (PEMFC) operates based on the following working principles:

Anode: At the anode catalyst layer of the fuel cell (CLa), hydrogen gas (H_2) is supplied. The hydrogen molecules undergo a catalytic oxidation reaction, typically facilitated by a platinum-based catalyst. This reaction splits the hydrogen molecules into protons (H^+) and electrons (e^-).

$$H_2 \rightarrow 2H^+ + 2e^-$$

The protons produced at the anode can easily pass through the electrolyte membrane, driven by their positive charge. Meanwhile, the electrons are unable to pass through the membrane and are forced to follow an external circuit, creating an electric current.

Cathode: At the cathode catalyst layer of the fuel cell (CLc), oxygen gas (O_2) from the air is supplied. The oxygen molecules undergo a reduction reaction, again facilitated by a catalyst (often platinum-based), in which they combine with protons and electrons from the external circuit to form water (H_2O).

$$2H^+ + 2e^- + \frac{1}{2}O_2 \rightarrow H_2O$$

By combining the anode and cathode reactions, the overall reaction of the PEMFC can be expressed as follows:

$$H_2 + {}^1/_2\, O_2 \rightarrow H_2O$$

This overall reaction represents the conversion of hydrogen and oxygen into water, accompanied by the release of electric energy and heat, as represented in *Figure 5*.

The exothermic nature of the cathode reaction generates heat, which needs to be managed to maintain proper operating temperatures. Additionally, water produced during the cathode reaction needs to be effectively removed from the fuel cell to prevent flooding and maintain efficient proton transport.

By leveraging the unique properties of the polymer electrolyte membrane and the catalytic reactions at the anode and cathode, a PEMFC enables the direct conversion of the chemical energy stored in hydrogen fuel into usable electrical energy, with water as the only byproduct.

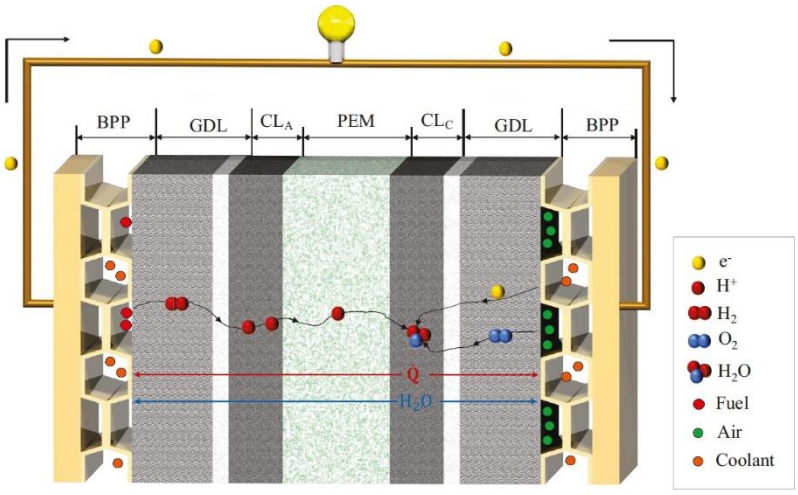

Figure 5 - Operation diagram of a PEM fuel cell

1.1.3 Applications

Fuel cells have been developed and utilized in various applications thanks to their interesting properties. These applications include:

- Transportation sector: Fuel cells are employed in the production of automobiles and trucks. Many automotive companies have already developed and demonstrated prototype vehicles, with several generations of fuel cell vehicles

already in existence. Fuel cells are also used in scooters, ships, aircraft, and utility vehicles such as forklifts and maintenance vehicles.

- Distributed power generation: Several companies are working on developing small-scale fuel cell power systems (1-10 kW) for domestic use, particularly in Japan and Germany. Some of these systems are combined with boilers to provide both electricity and heat.
- Backup power: Several companies made initial attempts to commercialize backup generators. These are regenerative fuel cells, which allow hydrogen to be used to generate electricity and vice versa, as the case may be. Hydrogen can be generated during periods of available electricity and converted back into electricity when needed.
- Portable power: Many companies are developing miniature fuel cells as a substitute for batteries in various electronic devices, including military and consumer electronics. In these cases, due to fuel storage challenges, most of them use methanol in direct methanol fuel cells or through micro-reformers in conventional PEM fuel cells.
- Space applications: Fuel cells continue to be used in the U.S. space program to provide power to space shuttles and other spacecraft.

In summary, fuel cells have found applications in transportation, distributed power generation, backup power, portable power, and space exploration due to their characteristics and advantages [1].

2 Introduction to the Finite Volume Method (FVM) Approach in Computational Fluid Dynamics

2.1 Mathematical Formulation of the Finite Volume Method

The Finite Volume Method (FVM) is a pillar of Computational Fluid Dynamics (CFD), employed to solve the partial differential equations (PDEs) that govern fluid flow, heat transfer, and mass transfer. The FVM is particularly favored for its ability to conserve fluxes across control volumes, making it inherently suitable for problems where conservation laws are critical. This method is applicable across a wide range of disciplines, from engineering to environmental science, due to its robustness and adaptability to complex geometries.

Unlike other numerical methods such as the Finite Difference Method (FDM) or the Finite Element Method (FEM), the FVM integrates the governing equations over discrete control volumes. This integration ensures that the flux entering and leaving a control volume is conserved, which is particularly important in fluid dynamics and heat transfer applications. The following sections delve into the mathematical formulation of the FVM, its discretization process, and its application to various fields.

2.1.1 Governing Equations in Integral Form

The foundation of the FVM is the integral form of the conservation laws. These laws are derived from the general conservation principles of mass, momentum, and energy, and are expressed in their integral forms over a control volume. Consider the general form of a conservation law for a scalar quantity ϕ, which could represent mass, momentum, energy, or any other conserved quantity:

$$\frac{\partial}{\partial t}\int_V \rho\varphi dV + \int_S \rho\varphi\, \boldsymbol{u} \cdot d\boldsymbol{A} = \int_S \Gamma_\varphi \nabla\varphi \cdot d\boldsymbol{A} + \int_V S_\varphi\, dV \qquad \text{Eq. 1}$$

where:

- ρ is the fluid density,

- ϕ is the conserved quantity,
- V is the control volume,
- S is the surface bounding the control volume,
- **u** is the velocity vector,
- Γ_φ is the diffusion coefficient associated with ϕ
- S_φ is the source term per unit volume.

This equation represents the conservation of ϕ, accounting for its rate of change within the volume V, convection across the surface S, diffusion across the surface S, and production or consumption within the volume V [3].

2.1.2 Discretization in the Finite Volume Method

The discretization process in FVM involves subdividing the computational domain into a finite number of control volumes (cells), typically arranged in a structured or unstructured grid. Each control volume is centered around a grid point, and the governing equations are applied to each control volume, resulting in a set of discrete algebraic equations [4].

2.1.3 Spatial Discretization

Consider a control volume V_i surrounding the grid point P, with neighboring grid points E, W, N, S, T, and B (corresponding to the east, west, north, south, top, and bottom faces, respectively). The integral conservation equation over V_i becomes:

$$\frac{\partial}{\partial t}(\rho_i \varphi_i V_i) + \sum_f \left(\rho_f \varphi_f \boldsymbol{u_f} \cdot \boldsymbol{dA_f}\right) = \sum_f \left(\Gamma_\varphi \nabla \varphi \cdot d\boldsymbol{A_f}\right) + S_{\varphi,i} V_i \qquad \text{Eq. 2}$$

where the summation is over all the faces f of the control volume i.

Convection Term

The convective flux through a face f is given by:

$$\Phi_f = \rho_f \varphi_f \boldsymbol{u_f} \cdot \boldsymbol{A_f} \quad \text{Eq. 3}$$

The value of φ_f at the face f is interpolated from the neighboring cell center values using schemes such as:

- Upwind Scheme: φ_f is taken from the upstream value.
- Central Difference Scheme: φ_f is the average of the values at the adjacent cell centers.

Diffusion Term

The diffusive flux through a face f is given by:

$$D_f = \Gamma_\varphi \nabla\varphi \cdot \boldsymbol{A_f} \quad \text{Eq. 4}$$

Using the gradient approximation between two adjacent cell centers P and E:

$$\nabla\varphi \cdot \boldsymbol{A_f} \approx \frac{\varphi_E - \varphi_P}{\delta x} \cdot A_f \quad \text{Eq. 5}$$

where δx is the distance between the cell centers P and E.

Source Term

The source term S_φ represents volumetric generation or absorption and is directly integrated over the control volume:

$$S_{\varphi,i} = S_\varphi V_i \quad \text{Eq. 6}$$

2.1.4 Temporal Discretization

For transient problems, the temporal derivative must also be discretized. Common schemes include the following [16].

Explicit Euler Scheme

The explicit Euler scheme is a first-order time integration method. It updates the solution based on the current known values. For a general time-dependent problem where φ_i is a scalar field (e.g., temperature, velocity component), the temporal derivative is discretized as:

$$\frac{\partial \varphi_i}{\partial t} \approx \frac{\varphi_i^{n+1} - \varphi_i^n}{\Delta t} \quad \text{Eq. 7}$$

In the explicit Euler scheme, the future value φ^{n+1} is calculated using the current value φ^n:

$$\varphi^{n+1} = \varphi^n + \Delta t R^n \quad \text{Eq. 8}$$

where R^n represents the residual or the sum of the fluxes (convective, diffusive, source terms, etc.) calculated at the current time step n.

- **Advantage**: The explicit scheme is straightforward and easy to implement.

- **Disadvantage**: It is conditionally stable, often requiring very small time steps (determined by the Courant-Friedrichs-Lewy (CFL) condition) to maintain stability [5].

Implicit Euler Scheme

The implicit Euler scheme is also a first-order method, but it involves solving for the future value implicitly, which means the method uses the unknown value at the next time step φ^{n+1} to update the solution:

$$\frac{\partial \varphi_i}{\partial t} \approx \frac{\varphi_i^{n+i} - \varphi_i^n}{\Delta t} \quad \text{Eq. 9}$$

In the implicit Euler scheme, this is rearranged as:

$$\varphi^{n+1} = \varphi^n + \Delta t R^{n+1} \quad \text{Eq. 10}$$

Here, R^{n+1} represents the residual calculated using the values at the next time step $n+1$, which means solving a system of equations to determine φ^{n+1}.

- **Advantage**: The implicit scheme is unconditionally stable, allowing larger time steps without violating stability conditions.

- **Disadvantage**: It requires solving a system of algebraic equations at each time step, which can be computationally expensive and complex.

2.1.5 Algebraic Equation System

The discretization of the governing equations leads to a system of algebraic equations of the form:

$$a_P \varphi_P = \sum a_{nb} \varphi_{nb} + b \quad \text{Eq. 11}$$

where a_P and a_{nb} are the coefficients related to the control volume P and its neighbors, and b is the contribution from the source terms and boundary conditions. The system is typically sparse, necessitating efficient solvers such as [5]:

- Gauss-Seidel Iteration
- Successive Over-Relaxation (SOR)
- Multigrid Methods
- Conjugate Gradient Methods

The choice of solver impacts both the convergence speed and computational efficiency.

2.1.6 Boundary Conditions in FVM

Boundary conditions are crucial for accurately solving the PDEs in FVM. Common types include:

- **Dirichlet Boundary Condition (Fixed Value):** Imposes a fixed value for φ at the boundary.
- **Neumann Boundary Condition (Fixed Gradient):** Specifies the gradient of φ normal to the boundary surface.
- **Robin Boundary Condition (Mixed):** A combination of Dirichlet and Neumann conditions.

For fluid dynamics problems, specific conditions such as no-slip (for velocity) at solid walls, and outflow or inflow conditions at domain boundaries, must be applied carefully to ensure realistic simulations.

In fuel cell (FC) simulations, additional considerations come into play due to electrochemical reactions and multiphase flows. For instance, boundary conditions should account for:

- **Humidity Control**: Membrane and reactant gases may require carefully prescribed humidity levels to represent real operating conditions.
- **Water Management**: Production, removal, and distribution of liquid water in catalyst layers and channels must be addressed, often leading to two-phase boundary conditions.

- **Temperature-Dependent Properties**: Heat transfer and temperature gradients can significantly influence reactant transport and reaction kinetics, necessitating appropriate thermal boundary settings.

By incorporating these FC-specific constraints, numerical models can more accurately capture the complex interplay of flow, species transport, and electrochemical reactions.

2.1.7 Applications of the Finite Volume Method

FVM's versatility makes it applicable to a broad spectrum of problems in engineering and science, such as:

Multiphase Flow Modelling

FVM is extensively used for modelling multiphase flows, where different fluid phases interact [6]. In the context of PEMFCs, FVM is particularly useful for simulating capillary action, phase change processes, and the complex interactions between liquid and gas phases [7] [8] [9]. The method ensures mass and energy conservation across interfaces, which is critical for accurately predicting phase distribution in porous media

Heat Transfer Analysis

FVM is ideal for solving heat transfer problems, whether in steady-state or transient conditions [10] [11] [12] [13] [14]. The method's ability to handle complex geometries and boundary conditions makes it suitable for applications ranging from the design of heat exchangers to thermal management in electronics and porous materials [15].

Fluid-Structure Interaction (FSI)

FVM coupled with structural solvers can be used to analyze Fluid-Structure Interaction (FSI) problems, where fluid flow impacts structural integrity, and vice versa. This is vital in aeroelasticity, biomechanics (such as blood flow in arteries), and civil engineering (e.g., wind forces on buildings).

Combustion and Reactive Flows

In combustion and reactive flow simulations, FVM handles the conservation of mass, momentum, energy, and species with precision. It is used in the design and optimization of combustion engines, analysis of pollutant formation, and in the chemical industry for simulating reactive processes.

Environmental Modelling

Environmental applications of FVM include modelling air and water pollution, groundwater flow, and the transport of contaminants. The method's ability to handle large-scale problems with varying spatial resolutions is invaluable in environmental engineering.

2.1.8 Advantages of the Finite Volume Method

The FVM offers several key advantages [4]:

1. **Conservation**: The FVM naturally conserves quantities like mass, momentum, and energy because it integrates the governing equations over control volumes. This makes it particularly reliable for fluid flow simulations.
2. **Flexibility with Complex Geometries**: FVM's compatibility with both structured and unstructured meshes allows it to handle complex geometries and boundary conditions more easily than methods like FDM.
3. **Stability and Robustness**: With appropriate discretization and time integration schemes, FVM is robust across a wide range of flow regimes, from incompressible to highly compressible flows, and from laminar to turbulent regimes.
4. **Versatility**: FVM can be applied to diverse physical phenomena, including fluid dynamics, heat transfer, mass transfer, and chemical reactions, making it a versatile tool in CFD.

2.1.9 Challenges and Limitations

Despite its strengths, FVM also has limitations [16]:

1. **Numerical Diffusion**: On coarse grids or with low-order interpolation schemes, FVM can suffer from numerical diffusion, especially in advection-dominated flows.
2. **Complexity in Higher-Order Schemes**: Implementing higher-order accuracy in the Finite Volume Method (FVM), particularly on unstructured grids, requires advanced reconstruction techniques and larger stencils for gradient and flux approximations. As a result, both the computational overhead and the complexity of the simulation increase significantly.
3. **Computational Cost**: For large-scale problems, especially those involving fine meshes or complex geometries, FVM can be computationally intensive.
4. **Handling of Moving Boundaries**: While FVM can handle complex stationary geometries well, problems involving moving boundaries require specialized techniques, such as Arbitrary Lagrangian-Eulerian (ALE) methods, which add to the complexity.

Recent Advances and Future Directions

Recent advances in FVM focus on improving accuracy and computational efficiency, including:

- **Higher-Order Schemes**: Techniques like Weighted Essentially Non-Oscillatory (WENO) schemes are being developed to improve accuracy while minimizing computational overhead [17].
- **Adaptive Mesh Refinement (AMR)**: AMR techniques allow for dynamic mesh refinement in regions with high gradients, improving accuracy without a proportional increase in computational cost [18].
- **Coupling with Other Methods**: Hybrid approaches that combine FVM with methods such as the Finite Element Method (FEM) or the Lattice Boltzmann Method (LBM) are increasingly explored to leverage the strengths of each technique in multi-physics simulations [19]. In particular, LBM excels in modelling flow and transport phenomena in porous media — due to its ability to handle complex pore structures at the microscale — making it a valuable counterpart to traditional FVM formulations [20].

- **Parallel Computing**: The development of parallel algorithms for FVM has enabled the solution of extremely large-scale problems, particularly in climate modelling, astrophysics, and large industrial applications.

The Finite Volume Method remains a foundational technique in CFD, prized for its conservation properties, flexibility, and robustness across a wide array of applications. While challenges remain, particularly in terms of numerical diffusion and computational cost, ongoing advancements continue to extend the method's capabilities. As computational power increases and new algorithms are developed, FVM is likely to remain a central tool in the simulation of fluid dynamics phenomena.

3 Numerical Modelling in PEMFC and PEMEC

3.1 Introduction of Mathematical Modelling for Multiphase Flows

3.1.1 Eulerian Multiphase Model (EMP)

The Eulerian Multiphase Model (EMP) represents a comprehensive approach to simulating systems involving multiple interacting fluid phases [21] [22]. Unlike the Mixture Multiphase Model (MMP), where fluid phases are treated as a single continuum, the EMP model handles each phase independently [23]. This method accounts for the distinct transport properties of each phase, providing a more accurate representation of the dynamics in highly saturated or complex systems where phase interactions are significant. The EMP model is particularly well-suited for systems where the relative motion between phases cannot be neglected, such as in fuel cell applications involving significant liquid water accumulation and transport [24].

In the context of Polymer Electrolyte Membrane Fuel Cells (PEMFCs), the Eulerian Multiphase Model is instrumental in accurately capturing the complex interactions between gas and liquid phases within the cell's porous components. These interactions are critical for predicting performance, particularly in the management of water transport and distribution, which are essential for maintaining optimal membrane hydration and preventing flooding or dehydration.

3.1.1.1 Governing Equations of the Eulerian Multiphase Model

The Eulerian Multiphase Model is formulated based on a set of conservation equations for mass, momentum, energy, and species for each individual phase [25]. In this model, the different phases (typically gas and liquid) are treated as interpenetrating continua, each described by its own set of governing equations. The interaction between the phases is modeled through source terms that represent momentum, mass, and energy transfer between the phases.

Mass Conservation Equation

For each phase *k*, the mass conservation (or continuity) equation can be expressed as:

$$\frac{\partial(\alpha_k \rho_k)}{\partial t} + \nabla \cdot (\alpha_k \rho_k \boldsymbol{u}_k) = \sum \quad \dot{m}_{kl} + S_q \qquad \text{Eq. 12}$$

where:

- α_k is the volume fraction of phase *k*,
- ρ_k is the density of phase *k*,
- $\boldsymbol{u}_k$ is the velocity vector of phase *k*,
- $\dot{m}_{kl}$ represents the mass transfer rate from phase *k* to phase *l*.
- S_q is the source term

Momentum Conservation Equation

The momentum equation for phase *k* is given by:

$$\frac{\partial(\alpha_k \rho_k \boldsymbol{u}_k)}{\partial t} + \nabla \cdot (\alpha_k \rho_k \boldsymbol{u}_k \boldsymbol{u}_k) = -\alpha_k \nabla p + \nabla \cdot (\alpha_k \overline{\overline{\boldsymbol{\tau}_k}}) + \alpha_k \rho_k \boldsymbol{g} + \boldsymbol{M}_{kl} + \boldsymbol{S}_k \qquad \text{Eq. 13}$$

where:

- p is the pressure shared by all phases,
- $\overline{\overline{\boldsymbol{\tau}_k}}$ is the stress tensor for phase k,
- **g** is the gravitational acceleration vector,
- $\boldsymbol{M}_{kl}$ represents the momentum exchange between phases *k* and *l*,
- $\boldsymbol{S}_k$ includes other source terms such as those arising from external forces or capillary effects.

The stress tensor τ_k typically accounts for viscous stresses within the phase, and the interphase momentum exchange $\boldsymbol{M}_{kl}$ is often modeled using empirical or semi-empirical

drag laws, which relate the momentum transfer to the relative velocity between the phases [22].

Energy Conservation Equation

The energy conservation equation for phase k is written as:

$$\frac{\partial(\alpha_k \rho_k E_k)}{\partial t} + \nabla \cdot (\alpha_k \rho_k E_k \boldsymbol{u}_k) = -\nabla \cdot (\alpha_k \boldsymbol{q}_k) + \alpha_k (\overline{\overline{\boldsymbol{\tau}_k}} : \nabla \boldsymbol{u}_k) + Q_{kl} + S_T \qquad \text{Eq. 14}$$

where:

- E_k is the total energy per unit mass for phase *k*,
- $\boldsymbol{q}_k$ is the heat flux vector for phase *k*,
- $\boldsymbol{Q}_{kl}$ represents the heat transfer between phases *k* and *l*,
- $\overline{\overline{\boldsymbol{\tau}_k}}$ è il tensore degli sforzi viscosi della fase *k,*
- S_T is the source term for energy, including contributions from chemical reactions and phase change.

The heat flux $\boldsymbol{q}_k$ includes both conductive and convective components, and the interphase heat transfer Q_{kl} may be described using empirical correlations that depend on the temperature difference between the phases and their relative velocities.

Species Conservation Equation

The species conservation equation for a species i in phase k is given by:

$$\frac{\partial(\alpha_k \rho_k Y_{i,k})}{\partial t} + \nabla \cdot \left(\alpha_k \rho_k Y_{i,k} \boldsymbol{u}_k\right) = -\nabla \cdot \left(\alpha_k \rho_k D_{i,k}^{eff} \nabla Y_{i,k}\right) + \dot{m}_{i,kl} + S_i \qquad \text{Eq. 15}$$

where:

- $Y_{i,k}$ is the mass fraction of species iii in phase k,

- $D_{i,k}^{eff}$ is the effective diffusion coefficient for species iii in phase k,
- $\dot{m}_{i,kl}$ represents the species mass transfer rate between phases k and l,
- S_i includes source terms such as those due to chemical reactions.

3.1.1.2 Application of the Eulerian Multiphase Model in PEMFCs

In PEMFCs, water management is crucial for achieving high performance and durability [26][27]. The challenge lies in maintaining sufficient hydration of the membrane while avoiding flooding, particularly in the gas diffusion layers (GDL) and catalyst layers (CL) [28]. The Eulerian Multiphase Model is particularly well-suited to address these challenges, as it allows for the simultaneous simulation of gas and liquid phases, capturing the intricate interactions between them.

Mass Transport in Multiphase Systems

In the GDL and CL, both oxygen and hydrogen gases need to be efficiently transported to the reaction sites while simultaneously managing the liquid water produced at the cathode [29]. The EMP model allows for the detailed analysis of these transport phenomena by solving the continuity equations for both gas and liquid phases. The volume fractions of the phases α_g and α_l can vary spatially and temporally, reflecting the dynamic nature of water generation and removal in the cell.

Momentum Exchange and Capillary Effects

The momentum exchange between the gas and liquid phases is critical for accurately predicting pressure drops and flow distribution within the cell [30]. The *Darcy–Forchheimer* relationship can be integrated into the momentum equations to account for the resistance offered by the porous structure of the GDL and CL. Additionally, capillary forces, which are a function of the surface tension and contact angle of the liquid within the porous media, can be included as source terms in the momentum equation. These capillary effects play a significant role in determining the saturation levels and distribution of liquid water in the GDL [31].

Heat and Species Transport

The heat generated by electrochemical reactions and ohmic losses needs to be effectively dissipated to maintain the PEMFC at an optimal operating temperature. The EMP model's energy conservation equations can capture the heat transfer between the phases and the solid components of the cell. The species conservation equations, on the other hand, are essential for modelling the transport of reactants (e.g., O_2 and H_2) and the removal of products (e.g., H_2O). The inclusion of electro-osmotic drag and back-diffusion in the species conservation equations provides a comprehensive picture of water transport within the membrane [32].

Modelling Phase Change

In low-temperature PEMFCs, water can exist in both vapor and liquid forms. The phase change between these forms is a key aspect of water management. The EMP model is capable of simulating phase transitions by including mass and energy transfer terms between the phases, which are governed by the local thermodynamic conditions. This capability is crucial for accurately predicting phenomena such as condensation in the gas flow channels or evaporation in the GDL.

3.1.1.3 Advantages and Challenges of the Eulerian Multiphase Model

The primary advantage of the EMP model lies in its ability to treat each phase independently, providing a detailed and physically accurate description of multiphase flows. This level of detail is particularly beneficial in the design and optimization of PEMFCs, where understanding the interactions between gas and liquid phases is crucial for improving efficiency and durability.

However, the EMP model is also computationally intensive due to the need to solve a set of conservation equations for each phase, along with the associated interphase interaction terms. These interaction terms, which include momentum, mass, and energy exchanges, must be accurately modeled to capture the true dynamics of the system. The complexity of the interphase interactions often requires the use of sophisticated numerical techniques and substantial computational resources, which can be a significant challenge, especially when dealing with large-scale or highly detailed simulations.

3.1.2 Mixture Multiphase Model (MMP)

The Mixture Multiphase Model (MMP) is a widely used approach in computational fluid dynamics (CFD) for simulating systems involving multiple fluid phases that are assumed to be miscible and in equilibrium [23][25]. Unlike the Eulerian Multiphase Model, where each phase is treated independently with its own set of conservation equations, the MMP model simplifies the problem by considering the different phases as a single mixed continuum. This assumption enables the simulation of multiphase flows with a reduced computational cost while still capturing the essential physics of phase interactions.

In the context of Polymer Electrolyte Membrane Fuel Cells (PEMFCs), the Mixture Multiphase Model is particularly useful for modelling the transport and distribution of water within the cell [33][34]. Water management is critical in PEMFCs to maintain membrane hydration and to avoid flooding in the gas diffusion layers (GDL) and catalyst layers (CL) [35]. The MMP model allows for the simulation of these processes by treating the gas and liquid phases as a mixture, simplifying the mathematical complexity while providing valuable insights into the cell's performance.

3.1.2.1 Governing Equations of the Mixture Multiphase Model

The Mixture Multiphase Model is based on a set of conservation equations for mass, momentum, energy, and species, where the fluid phases are assumed to move with a common velocity field [23]. This shared velocity assumption is a key characteristic of the MMP model, distinguishing it from more complex multiphase models that allow for relative motion between phases. The governing equations are solved for the mixture, with additional terms to account for the presence of multiple phases.

Mass Conservation Equation

The mass conservation equation for the mixture can be expressed as:

$$\frac{\partial \rho_{mix}}{\partial t} + \nabla \cdot (\rho_{mix} \boldsymbol{u}_{mix}) = S_m \qquad \text{Eq. 16}$$

where:

- ρ_{mix} is the density of the mixture, which is a weighted average of the densities of the individual phases,

- $\boldsymbol{u}_{mix}$ is the common velocity vector for the mixture,
- S_m represents the mass source term, accounting for phase changes or mass addition/removal due to reactions.

This equation ensures the conservation of mass in the system, considering the contributions from all phases as a single entity.

Momentum Conservation Equation:

The momentum conservation equation for the mixture is given by:

$$\frac{\partial(\rho_{mix}\boldsymbol{u_{mix}})}{\partial t} + \nabla \cdot (\rho_{mix}\boldsymbol{u}_{mix}\boldsymbol{u}_{mix}) = -\nabla p + \nabla \cdot (\mu_{mix}\nabla \boldsymbol{u}_{mix}) + \boldsymbol{S}_u \quad \text{Eq. 17}$$

where:

- μ_{mix} is the effective dynamic viscosity of the mixture,
- p is the pressure, assumed to be uniform across phases,
- $\boldsymbol{S}_u$ includes source terms related to momentum exchange between phases, drag forces, and other interfacial interactions.

In porous regions such as the GDL and CL, the momentum equation is often modified to include additional resistance terms, such as those described by the *Darcy–Forchheimer* law. These terms account for the flow resistance imposed by the porous structure, which is critical for accurately predicting pressure drops and flow distribution in the PEMFC.

Energy Conservation Equation

The energy conservation equation for the mixture is written as:

$$\frac{\partial((\rho C_p)_{mix}T)}{\partial t} + \nabla \cdot \left(\left(\rho C_p\right)_{mix}\boldsymbol{u}_{mix}T\right) = \nabla \cdot (k_{mix}\nabla T) + S_T \quad \text{Eq. 18}$$

where:

- $\left(\rho C_p\right)$ is the effective heat capacity of the mixture,
- T is the temperature,
- k_{mix} is the effective thermal conductivity of the mixture,

- S_T represents heat source terms, which can include contributions from chemical reactions, ohmic heating, and phase changes.

The energy equation ensures that the heat generated within the PEMFC is properly accounted for and that the temperature distribution across the cell is accurately predicted.

Species Conservation Equation

The species conservation equation for a species iii in the mixture is given by:

$$\frac{\partial(\rho_{mix}Y_i)}{\partial t} + \nabla \cdot (\rho_{mix}Y_i \boldsymbol{u}_{mix}) = \nabla \cdot \left(\rho_{mix}D_i^{eff}\nabla Y_i\right) + S_i \qquad \text{Eq. 19}$$

where:

- Y_i is the mass fraction of species iii in the mixture,
- D_i^{eff} is the effective diffusion coefficient for species iii in the mixture,
- S_i represents the source term for species iii, accounting for reactions and interfacial mass transfer.

This equation governs the transport of species within the mixture, ensuring that reactants are delivered to the reaction sites and products are removed efficiently. In the context of PEMFCs, this includes the transport of hydrogen, oxygen, and water vapor, as well as the production of liquid water.

3.1.2.2 Application of the Mixture Multiphase Model in PEMFCs

The Mixture Multiphase Model is particularly advantageous in the simulation of PEMFCs because it simplifies the complex interactions between phases while still capturing the essential physics of water management. Water management is a critical aspect of PEMFC operation, as it directly affects the performance and durability of the fuel cell [35]. The MMP model provides a framework for understanding how water is distributed and transported within the cell, from the anode to the cathode, and how it interacts with the reactant gases.

Water Transport and Distribution

The MMP model allows for the simulation of water transport as part of a mixed-phase continuum, where both liquid and vapor phases are present. The common velocity assumption simplifies the computational effort while still allowing for an accurate representation of water transport mechanisms such as capillary action and evaporation-condensation processes.

Porous Media and Capillary Effects

The GDL and CL in PEMFCs are porous materials that play a crucial role in water management. Models appropriate for these porous structures typically extend or modify the standard conservation equations, often incorporating Darcy's law (or Darcy–Brinkman/Darcy–Forchheimer extensions) for fluid flow in porous media. The MMP approach can integrate these formulations by adjusting the momentum and species conservation equations to account for flow resistance and phase interactions in the porous matrix.

Capillary effects, critical for determining the distribution of liquid water within the pores, are usually introduced through additional source terms in the momentum equation, reflecting capillary pressure gradients. Accurately modeling these phenomena is essential for predicting the onset of flooding and for designing GDLs with optimal water transport properties. By including dedicated porous media models, the numerical framework can more reliably capture the interplay of gas and liquid phases, ensuring more realistic simulation of PEMFC operation.

Species Transport

The transport of reactant gases (hydrogen and oxygen) and the removal of product water are central to the performance of a PEMFC. The MMP model allows for the coupled simulation of species transport and reaction dynamics within the cell [33]. By treating the phases as a mixture, the model can account for species-specific diffusion coefficients (e.g., separate diffusion coefficients for hydrogen and oxygen) in the governing equations, often based on Fick's law or experimentally derived relationships. These coefficients capture differences in molecular size and interactions between water vapor and reactant gases. The species conservation equations then ensure that the correct amount of each

reactant is delivered to the catalyst sites and that product water is removed efficiently, helping to prevent flooding or dehydration effects that can degrade performance.

Thermal Management

Heat generation and dissipation are critical aspects of PEMFC operation, as excessive temperatures can lead to membrane degradation and reduced efficiency [35]. The MMP model's energy conservation equation provides a means to simulate the thermal behavior of the cell, including the effects of phase change and the heat of vaporization of water. By accurately predicting the temperature distribution within the cell, the MMP model helps in optimizing thermal management strategies to maintain the PEMFC within its optimal operating temperature range.

3.1.2.3 Advantages and Challenges of the Mixture Multiphase Model

The Mixture Multiphase Model offers several advantages in the context of PEMFC simulation. Its primary strength lies in its ability to simplify the complex interactions between multiple fluid phases while still capturing the key physical phenomena that govern water management, species transport, and thermal behavior. By treating the phases as a mixture with a common velocity, the MMP model reduces the computational burden compared to more complex multiphase models, making it feasible to simulate large-scale systems or to conduct parametric studies [2].

However, the MMP model also has its limitations. The assumption of a common velocity field for all phases may not be accurate in situations where significant slip or relative motion between phases occurs. Additionally, the model's ability to capture sharp interfaces between phases is limited, which can be a drawback in scenarios where precise interface tracking is essential. Despite these limitations, the MMP model remains a valuable tool for the simulation of PEMFCs, particularly in applications where computational efficiency is a priority.

In summary, the Mixture Multiphase Model is a robust and efficient approach for simulating the multiphase flow dynamics within PEMFCs. It provides a good balance between computational simplicity and physical accuracy, making it an ideal choice for

understanding and optimizing the complex processes involved in water management, species transport, and thermal behavior in fuel cells. As PEMFC technology continues to evolve, the MMP model will likely play a crucial role in advancing our understanding and improving the performance of these systems [28][34].

3.1.3 Volume of Fluid (VOF) Method

The Volume of Fluid (VOF) approach is a numerical technique used for modelling immiscible multiphase flows where the interface between the phases is of primary interest [37]. Developed initially for capturing free surface flows, the VOF method has been widely adopted in various engineering applications, ranging from fluid dynamics problems involving large-scale interface tracking, such as wave motion, to microscale phenomena, such as droplet formation and coalescence. The method is particularly powerful in scenarios where the sharp delineation between phases, such as gas and liquid, needs to be accurately resolved.

In the context of Polymer Electrolyte Membrane Fuel Cells (PEMFCs), the VOF approach is employed to model the behavior of liquid water within the cell, especially in capturing the dynamics of water droplets in the gas flow channels and within the porous layers of the cell. Proper management of water is crucial in PEMFCs, as it affects the membrane's hydration and the cell's overall performance. The VOF method's ability to track and predict the movement and distribution of water within the cell's structure makes it a valuable tool for optimizing PEMFC designs to prevent flooding and ensure efficient operation [38].

3.1.3.1 Fundamental Concepts of the VOF Method

The VOF approach is based on the idea of using a volume fraction function to represent the presence of different phases within a computational cell [37]. The key concept is the introduction of a scalar function, α\alphaα, known as the volume fraction, which indicates the proportion of each phase within a given computational cell. For instance, in a two-phase system consisting of gas and liquid, the volume fraction α\alphaα of the liquid phase would be defined as:

$$\alpha_l \begin{cases} 1 & if\ the\ cell\ is\ completely\ filled\ with\ liquid \\ 0 & if\ the\ cell\ contains\ no\ liquid\ (i.e.,\ is\ filled\ with\ gas), \\ 0 < \alpha_l < 1 & if\ the\ cell\ contains\ an\ interface\ between\ gas\ and\ liquid \end{cases}$$

The sum of the volume fractions for all phases within a cell is unity, ensuring that each cell is fully occupied by the available phases.

$$\alpha_l + \alpha_g = 1 \qquad \text{Eq. 20}$$

This volume fraction is advected through the computational domain using a transport equation, which governs the evolution of the interface between the phases.

The VOF method thus requires solving this advection equation in conjunction with the Navier-Stokes equations to capture the fluid dynamics of the system [37]. The interface between the phases is reconstructed based on the volume fraction field, which is then used to compute surface tension forces, boundary conditions at the interface, and other relevant physical phenomena.

3.1.3.2 Governing Equations in the VOF Approach

The VOF method is embedded within the framework of the Navier-Stokes equations, which govern the fluid motion. The governing equations for a two-phase system using the VOF approach are the following.

Continuity Equation

The continuity equation for an incompressible fluid is given by:

$$\nabla \cdot \mathbf{u} = 0 \qquad \text{Eq. 21}$$

Where:

- $\mathbf{u}$ is the velocity vector

This equation ensures the conservation of mass within the fluid, maintaining a consistent volume throughout the simulation.

Momentum Conservation Equation:

The momentum equation, which accounts for the fluid's motion, is expressed as:

$$\frac{\partial(\rho \boldsymbol{u})}{\partial t} + \nabla \cdot (\rho \boldsymbol{u}\boldsymbol{u}) = -\nabla p + \nabla \cdot [\mu(\nabla u + (\nabla u)^T)] + \boldsymbol{F}_\sigma + \rho \boldsymbol{g} \quad \text{Eq. 22}$$

where:

- ρ is the fluid density, which is a function of the volume fraction α\alphaα,
- μ is the dynamic viscosity of the fluid, also dependent on α,
- $\boldsymbol{F}_\sigma$ represents the surface tension force acting at the interface between phases,
- **g** is the gravitational acceleration vector.

The surface tension force $\boldsymbol{F}_\sigma$ is particularly important in the VOF method, as it significantly influences the behavior of the interface, especially in small-scale flows such as droplet formation and breakup [39]. The computation of this force typically involves the curvature of the interface and the gradient of the volume fraction.

Volume Fraction Transport Equation

The volume fraction transport equation is central to the VOF method, as it determines the movement and shape of the interface between the phases:

$$\frac{\partial \alpha}{\partial t} + \nabla \cdot (\alpha \mathbf{u}) + \nabla \cdot (\alpha(1-\alpha)\boldsymbol{u}_r) = 0 \quad \text{Eq. 23}$$

Where:

- α is the volume fraction of the fluid phase (e.g., liquid phase)
- $\boldsymbol{u}$ is the common velocity field shared by all phases
- $\boldsymbol{u}_r$ is the relative velocity field used to sharpen the interface

This equation is solved simultaneously with the Navier-Stokes equations to track the interface's evolution over time.

Energy Equation

The energy conservation equation for incompressible, immiscible multiphase flows in the VOF method is given by:

$$\frac{\partial(\rho E)}{\partial t} + \nabla \cdot ((\rho E + p)\boldsymbol{u}) = -\nabla \cdot \boldsymbol{q} + S_E \quad \text{Eq.24}$$

Where:

- E is the total energy per unit mass
- $\boldsymbol{q}$ is the heat flux vector
- S_E represents energy source terms, such as those due to phase change or chemical reactions.

3.1.3.3 Reconstruction of the Interface

The reconstruction of the interface between different phases is a critical aspect of the Volume of Fluid (VOF) method. The accuracy with which the interface is reconstructed directly impacts the overall fidelity of the simulation, particularly in applications where the dynamics of the interface play a significant role, such as in droplet formation, coalescence, breakup, and interaction with solid boundaries [40]. The challenge in interface reconstruction lies in accurately capturing the sharp transition between phases while maintaining computational efficiency.

In the VOF method, the phase interface is represented implicitly by the volume fraction field α. The interface between the phases is not explicitly tracked but is inferred from the values of α within the computational cells. Cells where $0 < \alpha_l < 1$ indicate the presence of an interface. The primary goal of interface reconstruction is to accurately determine the position and shape of this interface within these mixed cells.

Accurate interface reconstruction is essential for several reasons:

- **Surface Tension Calculation**: The computation of surface tension forces, which are crucial in multiphase flows involving small-scale phenomena such as capillary action and droplet dynamics, depends on the accurate determination of the interface curvature [39]. Errors in interface reconstruction can lead to incorrect curvature estimates, resulting in inaccurate surface tension forces.

- **Mass Conservation**: Inaccurate interface reconstruction can lead to numerical diffusion, where the interface becomes smeared across several cells, causing a loss of sharpness and potentially leading to non-physical mass transfer between phases [40]. This can violate the conservation of mass and compromise the accuracy of the simulation.
- **Interaction with Boundaries**: The interaction between the fluid interface and solid boundaries, such as walls or obstacles, is critical in many applications [39]. Accurate reconstruction ensures that the contact angles and wetting behavior are correctly modeled, which is particularly important in simulating flows in porous media or near surfaces with specific wettability properties.

Interface Reconstruction Techniques

Several techniques have been developed to reconstruct the phase interface in the VOF method. The choice of technique depends on the desired accuracy, computational resources, and the specific characteristics of the flow being modeled. The most commonly used techniques include:

Simple Line Interface Calculation (SLIC)

The Simple Line Interface Calculation (SLIC) method is one of the earliest and simplest techniques for interface reconstruction [41]. In SLIC, the interface within each cell is assumed to be aligned with one of the coordinate axes, either as a horizontal or vertical line (in 2D) or a plane (in 3D). The position of the line or plane is determined based on the volume fraction values.

While SLIC is computationally efficient and easy to implement, it suffers from low accuracy in capturing complex or curved interfaces [42]. The method's assumption of axis-aligned interfaces can lead to a significant geometric error, particularly in cases where the actual interface is not aligned with the coordinate axes. As a result, SLIC is generally used in applications where computational speed is prioritized over accuracy.

Piecewise Linear Interface Calculation (PLIC)

The Piecewise Linear Interface Calculation (PLIC) method is a more advanced and accurate technique for interface reconstruction [43]. Unlike SLIC, PLIC does not assume that the interface is aligned with the coordinate axes. Instead, it approximates the interface as a straight line (in 2D) or a plane (in 3D) within each mixed cell. The orientation and position of this line or plane are determined by solving a geometric problem based on the volume fraction values and the gradients of the volume fraction field.

PLIC significantly improves the accuracy of interface reconstruction, particularly in capturing curved and complex interfaces. The method minimizes numerical diffusion and maintains a sharp interface between phases. PLIC is widely used in applications where the precise representation of the interface is crucial, such as in the simulation of capillary flows, droplet dynamics, and interfacial instabilities.

The process of determining the orientation and position of the interface in PLIC involves the following steps:

- **Calculate the Volume Fraction Gradient**: The gradient of the volume fraction field is computed to determine the direction in which the interface is likely oriented.
- **Determine the Interface Orientation**: Based on the gradient, the orientation of the interface is approximated as a linear segment or plane.
- **Position the Interface**: The position of the interface within the cell is adjusted to ensure that the correct volume fraction is maintained within the cell. This step involves solving a geometric problem to match the computed volume fraction.

The PLIC method, while more computationally intensive than SLIC, provides a much higher level of accuracy and is considered the standard approach for interface reconstruction in the VOF method.

Height Function Method:

The Height Function method is another technique used in the VOF method to improve the accuracy of curvature calculations, which are essential for accurately modelling

surface tension forces. In this method, the interface is reconstructed using height functions, which represent the height of the fluid column above a reference plane [44].

The Height Function method is particularly effective in scenarios where surface tension plays a dominant role, such as in microfluidics or in the simulation of small droplets. By accurately reconstructing the interface and calculating the curvature directly from the height functions, this method minimizes errors in surface tension force computation.

The primary challenge of the Height Function method is that it requires a well-defined interface and is sensitive to the resolution of the computational grid. Inadequate grid resolution can lead to inaccuracies in height function calculations, thereby affecting the overall accuracy of the simulation.

Level-Set and VOF Hybrid Methods:

To combine the strengths of the VOF method with other interface tracking methods, hybrid approaches such as the Level-Set/VOF method have been developed. In these hybrid methods, the VOF approach is used to track the volume fractions, while the Level-Set method is employed to provide a more accurate description of the interface geometry [45].

The Level-Set method represents the interface as the zero level set of a signed distance function, which allows for a smooth and continuous representation of the interface. By coupling the Level-Set method with VOF, hybrid methods can achieve better accuracy in interface reconstruction while maintaining the mass conservation properties of the VOF method.

These hybrid methods are particularly useful in simulations involving complex interface dynamics, such as those with significant topological changes (e.g., merging or breakup of interfaces).

3.1.3.4 Application of the VOF Method in PEMFCs

The VOF approach is particularly well-suited for modelling water behavior in PEMFCs, where the accurate tracking of liquid water distribution and movement is critical. Water management is a central challenge in PEMFC design and operation, as both excess and insufficient water can lead to performance degradation [46]. The VOF method's ability to

capture the dynamics of water droplets, film formation, and transport within the gas channels and porous layers makes it an essential tool in this context.

Droplet Formation and Removal in Gas Channels

In PEMFCs, water produced at the cathode accumulates as droplets in the gas flow channels. These droplets must be effectively removed to prevent flooding, which can block reactant gas flow and reduce cell efficiency [47]. The VOF method is highly effective in simulating the formation, growth, coalescence, and eventual removal of water droplets in the gas channels. By accurately modelling the surface tension forces and interface dynamics, the VOF approach can predict how droplets interact with the channel walls and how they are swept away by the gas flow.

Understanding these processes is crucial for designing gas channels with geometries and surface treatments that promote efficient water removal, thereby preventing flooding and maintaining high reactant gas transport rates.

Water Distribution in Porous Media

The GDL and CL in PEMFCs are porous structures where water can exist in both liquid and vapor phases. The VOF method can be employed to model the distribution of liquid water within these porous media, capturing the complex interactions between capillary forces, phase change, and external forces such as the gas flow.

The accurate tracking of the liquid-gas interface within the pores is essential for understanding how water moves through the GDL, how it interacts with the catalyst layer, and how it impacts the overall performance of the fuel cell. The VOF approach can simulate scenarios such as water breakthrough, where liquid water penetrates through the GDL into the gas channels, leading to potential flooding.

3.1.3.5 Advantages and Challenges of the VOF Method

The Volume of Fluid method offers several distinct advantages in the context of multiphase flow modelling, particularly for applications like PEMFCs where accurate interface tracking is crucial [37]. One of the primary strengths of the VOF approach is its

ability to capture sharp interfaces between immiscible phases, such as the gas-liquid interface in water droplets. This capability is particularly valuable in modelling scenarios where the interface dynamics play a critical role in the overall system behavior, such as in droplet formation, coalescence, and detachment in fuel cell gas channels.

Another significant advantage of the VOF method is its flexibility in handling complex geometries and boundary conditions. The method can be applied to irregularly shaped domains and can accommodate moving boundaries, making it suitable for a wide range of engineering applications beyond PEMFCs. Additionally, the VOF approach can be coupled with other physical models, such as those for heat transfer, phase change, and chemical reactions, providing a comprehensive framework for multiphase flow simulation.

However, the VOF method also presents several challenges. One of the primary difficulties lies in the accurate reconstruction of the interface, especially in three-dimensional simulations where the interface geometry can be highly complex [40]. The quality of the interface reconstruction directly affects the accuracy of the simulation, particularly in the calculation of surface tension forces and the prediction of capillary effects. Inaccuracies in interface tracking can lead to numerical diffusion, where the interface becomes smeared over several computational cells, reducing the precision of the model.

Another challenge is the computational cost associated with the VOF method. Although the method itself is relatively straightforward, the need to resolve the interface with high accuracy often requires fine mesh resolutions and small time steps. This can become especially cumbersome when the dimensions or location of the liquid phases are not known a priori, necessitating adaptive or refined meshing around the interface. Consequently, large-scale simulations or those coupling the VOF approach with other complex physical models can face significantly increased computational demands.

The VOF method is also sensitive to the choice of numerical schemes used for solving the transport equations. The advection scheme, in particular, must be carefully selected to minimize numerical diffusion and to ensure that the interface remains sharp and well-defined throughout the simulation. The balance between accuracy and computational efficiency is a key consideration in the application of the VOF method.

In conclusion, the Volume of Fluid method is a powerful tool for modelling multiphase flows, particularly in applications where accurate interface tracking is essential, such as in PEMFCs. While it presents certain challenges, particularly in terms of interface reconstruction and computational cost, its ability to capture the detailed dynamics of phase interfaces makes it invaluable in the design and optimization of systems where phase interactions are critical. As computational resources continue to improve and as new techniques for interface reconstruction and advection are developed, the VOF method is likely to become even more widely used in the simulation of complex multiphase systems.

3.1.4 Capillary Action and Phase Change

Capillary action, or capillarity, is a critical phenomenon in the transport of water within the porous layers of systems modeled using multiphase approaches such as the Mixture Multiphase Model (MMP), Eulerian Multiphase Model (EMP), and others. This action results from the balance between surface tension and the adhesive forces between the liquid phase (e.g., water) and the solid material of the porous medium [48]. In contexts like the Gas Diffusion Layer (GDL) and Catalyst Layer (CL) of PEMFCs or similar systems, capillary forces are essential for driving fluid from regions of high saturation to areas of lower saturation, ensuring a balanced distribution of liquids across the system [28].

Capillary pressure (P_c) governs this fluid movement and is influenced by several factors, including the pore size distribution of the medium, the wettability of surfaces (characterized by the contact angle θ_c), and the surface tension σ of the liquid. Smaller pores typically exert higher capillary pressures, which move fluids within the microstructure from saturated regions to drier ones [48]. The role of hydrophobic components (e.g., water-repellent treatments or coatings) also modifies this behavior by affecting the contact angle, thus impacting how easily water can wet or be repelled by the pore walls.

Because direct experimental determination of capillary pressure in complex porous structures is often challenging, many models use the Leverett function to estimate P_c from measurable properties like liquid saturation and porosity. One common form of the Leverett function is [49]:

$$J(S) = \frac{P_c\sqrt{k}}{\sigma\ cos(\theta_c)} \quad \text{Eq. 25}$$

Where:

- J(S), is an empirical relationship that connects capillary pressure P_c to the liquid saturation and the characteristics of the porous medium:

$$J(S) = \sqrt{\varepsilon}(1.417s - 2.120s^2 + 1.263s^3) \quad \text{Eq. 26}$$

- J(S) is a dimensionless function relating capillary pressure to liquid saturation s (the fraction of pore space occupied by the liquid) and the porous medium's properties.
- P_c is the capillary pressure.
- k is the absolute permeability (a measure of how easily fluids can flow through the porous material).
- σ is the surface tension of the liquid.
- θ_c is the contact angle, which indicates the wettability of the medium (hydrophobic or hydrophilic).
- ε is the porosity, defining the fraction of the total volume occupied by pores.

In multiphase modeling (e.g., MMP or EMP), incorporating the Leverett function allows the capillary pressure to dynamically adjust based on the local saturation at each point in the porous medium. This is particularly valuable for predicting water distribution under varying operating conditions and for preventing phenomena like flooding (excessive liquid saturation) or dehydration (insufficient liquid saturation). The capillary action thus works in tandem with phase change processes, like condensation and evaporation, which can alter local saturation levels, influencing capillary pressures and overall fluid transport.

By accounting for both capillarity and phase changes, multiphase models offer a holistic perspective on fluid behavior in complex systems. Engineers and researchers can then optimize the design of porous media (e.g., GDLs, CLs) to manage fluid distribution effectively, balancing the need for adequate hydration with the risk of performance degradation due to flooding or insufficient water content. The integration of empirical relationships like the Leverett function thus enhances the predictive capabilities of these models, guiding improved fluid management strategies across a wide range of applications [46].

3.1.5 Surface Tension and Wettability

The interaction between water droplets and the surfaces of the Gas Diffusion Layer (GDL), Catalyst Layer (CL), and gas channels in a Proton Exchange Membrane Fuel Cell (PEMFC) is critically influenced by the wettability characteristics of these materials. Wettability, quantified by the contact angle θ between a liquid droplet and a solid surface, plays a pivotal role in determining how water spreads or beads up on these surfaces [46]. This property is essential in controlling water management within the fuel cell, where both excessive water (leading to flooding) and insufficient water (leading to dehydration) can significantly impact performance.

Wettability is governed by the balance of intermolecular forces at the interface of the liquid, solid, and gas phases. The contact angle is determined by Young's equation [50]:

$$\cos\theta = \frac{\sigma_{SG}\sigma_{SL}}{\sigma_{LG}} \qquad \text{Eq. 27}$$

where:

- σ_{SG} is the solid-gas interfacial tension,
- σ_{SL} is the solid-liquid interfacial tension,
- σ_{LG} is the liquid-gas interfacial tension.

This equation illustrates how surface energies influence the contact angle and, consequently, the wettability of the surface. A low contact angle ($\theta < 90°$) indicates hydrophilic behavior, promoting wetting and spreading of water on the surface. Conversely, a high contact angle ($\theta > 90°$) signifies hydrophobic behavior, causing water to bead up and resist spreading [51].

3.1.5.1 Surface Tension and Capillary Effects in Porous Media

Surface tension (σ_{LG}) is a crucial factor in the stability and movement of fluid phases within the porous structures of the GDL and CL. The capillary pressure (P_c) governing the movement of water through these porous media is described by the Young-Laplace equation:

$$P_c = \frac{2\sigma_{LG}\cos\theta}{r} \quad \text{Eq. 28}$$

where:

- r is the effective pore radius.

This relationship indicates that smaller pore sizes and higher surface tensions increase capillary pressure, influencing water transport and retention within the fuel cell layers [28].

The materials used in the GDL and CL, typically carbon-based substrates, can be engineered to have specific wettability characteristics. Hydrophobic treatments, such as the application of polytetrafluoroethylene (PTFE), are often used to enhance water repellency in the GDL and MPL, facilitating the removal of excess water and preventing flooding. In contrast, the CL may require a balanced wettability to ensure efficient proton conduction while avoiding water accumulation that could block reactive sites.

Surface modifications at the micro and nanoscale, including coating, texturing, and chemical treatments, can tailor the wettability of these materials [52]. For example, incorporating hydrophilic additives or creating hierarchical structures can improve water management by promoting uniform water distribution and facilitating vapor diffusion.

Multiphase models provide a detailed framework for simulating the complex interactions between liquid water, gas phases, and the porous media within PEMFCs. These models

incorporate surface tension effects and contact angles to predict capillary-driven transport, phase change phenomena, and the distribution of water within the GDL, CL, and gas channels.

By solving the coupled mass, momentum, and energy conservation equations, along with appropriate constitutive relationships, multiphase models can predict the onset of flooding or dehydration under various operating conditions [52]. Parameters such as pore size distribution, permeability, and relative humidity are critical inputs that influence the accuracy of these simulations.

3.1.6 Hydrophobic and Hydrophilic Treatments, Contact Angles, and Multiphase Modelling

Effective water management is critical in the design and optimization of Polymer Electrolyte Membrane Fuel Cells (PEMFCs) to ensure high performance and longevity. Key to this is the control of water distribution within the cell's porous layers, such as the GDL and CL. The hydrophobicity or hydrophilicity of these materials, along with the contact angles of water droplets on their surfaces, play a significant role in determining how water is retained, transported, or removed from these layers. Different multiphase modelling approache, Mixture Multiphase Model (MMP), Eulerian Multiphase Model (EMP), and Volume of Fluid (VOF), handle these phenomena with varying degrees of detail and accuracy.

3.1.6.1 MMP (Mixture Multiphase Model)

- Hydrophobic and Hydrophilic Treatments: The MMP approach simplifies the modelling of multiphase flows by treating the different phases as a single continuum in equilibrium. While this model can approximate the effects of hydrophobic and hydrophilic treatments by adjusting the effective properties of the mixture, it does not explicitly simulate individual droplets or their interactions with surfaces. Therefore, MMP is better suited for generalized predictions of water retention or removal in treated GDLs or CLs, rather than capturing the specific dynamics of droplet formation and movement.

- Contact Angle and Surface Effects: Surface tension and contact angles in the MMP model are incorporated as averaged properties. However, this model does not resolve the intricate details of contact angle hysteresis or the dynamic behavior of droplets on surfaces. The difference between advancing and receding contact angles can significantly influence how water droplets initiate movement or remain pinned on a surface. This hysteresis arises due to factors such as surface roughness, chemical heterogeneities, and impurities. In the theoretical framework, one would account for hysteresis by using separate advancing and receding contact angles to describe the liquid–solid interaction more precisely. Because the MMP model does not fully resolve these intricate details, nor the dynamic behavior of droplets at the pore-scale, it is limited in simulating how water spreads or beads on hydrophobic or hydrophilic surfaces. Consequently, MMP is limited in simulating how water spreads or beads on hydrophobic or hydrophilic surfaces, particularly at the microstructural level.

3.1.6.2 EMP (Eulerian Multiphase Model)

- Hydrophobic and Hydrophilic Treatments: The EMP model treats each phase separately, allowing for a more detailed simulation of phase interactions compared to MMP. The effects of hydrophobic and hydrophilic treatments can be modeled with greater specificity, especially in terms of phase distribution within the GDL and CL. The EMP approach can simulate how surface treatments impact the overall distribution and movement of water in the cell, though it still abstracts some of the finer details at the droplet level.

- Contact Angle and Surface Effects: The EMP model incorporates surface tension and capillary effects with more granularity than MMP, enabling the simulation of some aspects of contact angles and their impact on water distribution. However, like MMP, EMP does not fully capture the dynamic behavior of contact angles or detailed surface interactions, making it less precise in predicting water behavior on surfaces with varying wettability.

3.1.6.3 VOF (Volume of Fluid)

- Hydrophobic and Hydrophilic Treatments: The VOF method excels at simulating the detailed behavior of multiphase flows, particularly when modelling surface interactions at the micro-scale. This method is ideal for capturing the effects of hydrophobic and hydrophilic treatments on droplet formation, detachment, and transport within the GDL and gas channels. VOF allows for precise modelling of how treated surfaces influence water dynamics, offering insights into optimizing surface properties for improved water management in PEMFCs.
- Contact Angle and Surface Effects: VOF is highly effective at explicitly modelling contact angles and their dynamic behavior, including contact angle hysteresis. This capability is crucial for understanding how water droplets spread or retract on treated surfaces, whether hydrophilic or hydrophobic. Additionally, VOF can simulate the effects of surface roughness on wettability, providing detailed insights into how microstructural features influence water retention and removal in PEMFCs. This level of detail makes VOF the preferred approach for designing and optimizing GDLs and CLs with tailored surface properties to enhance fuel cell performance.

Summary of Applications and Modelling Capabilities

- MMP: Best suited for broad, averaged predictions of water management strategies within PEMFCs. It can account for general effects of hydrophobic and hydrophilic treatments but lacks the detail to model specific droplet behavior and surface interactions.
- EMP: Offers a more detailed approach, with the ability to separately model phases and their interactions. It simulates water distribution more accurately than MMP but abstracts the finer details of surface interactions, making it less precise than VOF in applications like droplet dynamics and surface roughness effects.
- VOF: Provides the most detailed and accurate modelling of surface tension, contact angles, and their effects on water distribution in PEMFCs. It is particularly

well-suited for applications that require a precise understanding of how surface characteristics and droplet dynamics influence local wetting and water management, crucial for optimizing performance and preventing flooding at the micro-scale.

3.2 Conservation of Electric and Protonic Charge

In addition to the previously discussed governing equations, the conservation of electric and protonic charge is a critical principle in the modelling of electrochemical systems, such as Polymer Electrolyte Membrane Fuel Cells (PEMFCs). This principle ensures that the transport of electrons and protons within the system complies with the laws of charge conservation, maintaining equilibrium between charge sources and sinks across the various cell components. To accurately simulate the behavior of fuel cells, two additional governing equations are required, specifically addressing the conservation of electric and protonic charges. These equations are essential for capturing the complex interactions within the cell, enabling precise modelling of current flow and ion transport, which are pivotal for predicting overall cell performance and efficiency.

In PEMFCs, electric charge conservation is primarily governed by the continuity of the current in the solid conducting phases, such as the gas diffusion layer (GDL), catalyst layer (CL), and the bipolar plates (BP). The conservation of electric charge is mathematically expressed through the Ohm's law equation [2]:

$$\nabla(\sigma^{eff}\nabla\Phi_e) + S_{\Phi_e} = 0 \qquad \text{Eq. 29}$$

where σ^{eff} is the effective electrical conductivity of the solid phase, Φ_e is the electric potential, and S_{Φ_s} represents the source term associated with the generation or consumption of current, typically occurring at the reaction sites within the CL. This

equation ensures that the total current entering and leaving any given region is balanced, accounting for the current generated by the electrochemical reactions.

The effective isotropic conductivity σ^{eff} of bipolar plates is relatively straightforward to determine, but the same cannot be said for gas diffusion layers (GDL), which are porous media. Numerous correlations for the effective conductivity of carbon paper GDLs have been presented in the literature, derived from experimental data fitting and valuable for 3D-CFD models as a function of GDL porosity ε. However, many of these correlations do not differentiate between through-plane and in-plane electrical conductivity, resulting in inconsistencies that impede the development of physically accurate numerical models. Notable examples of such correlations include those proposed by Das et al. [53], Looyenga [54], and the widely adopted Bruggeman approximation [55]. A significant exception is the correlation developed by Zamel et al. [56], which is based on a 3D-reconstructed anisotropic porous material and provides separate coefficients for through-plane and in-plane conductivities. All of these correlations are summarized in *Table 1* and illustrated in *Figure 6*.

Table 1 - Correlations for GDL electrical conductivity σ^{eff} [S/m]

Ref.	Correlation	Notes
[53]	$\sigma^{eff} = \sigma_s \frac{2-2\varepsilon}{2+\varepsilon}$	Bulk conductivity: though-/in-plane directions not distinguished.
[54]	$\sigma^{eff} = \sigma_s(1-\varepsilon)^3$	Bulk conductivity: though-/in-plane directions not distinguished.
[55]	$\sigma^{eff} = \sigma_s(1-\varepsilon)^{1.5}$	Bulk conductivity: though-/in-plane directions not distinguished.
[56]	$\sigma^{eff} = \sigma_s\left\{1-\left(\frac{3\varepsilon}{2+\varepsilon}\right)Ae^{[B(1-\varepsilon)](1-\varepsilon)^C}\right\}$	Through-plane: A = 0.962 ± 0.01, B = 0.889 ± 0.015, C = -0.00715 ± 0.005 In-plane: A = 0.962 ± 0.004, B = 0.367 ± 0.005, C = -0.016 ± 0.002

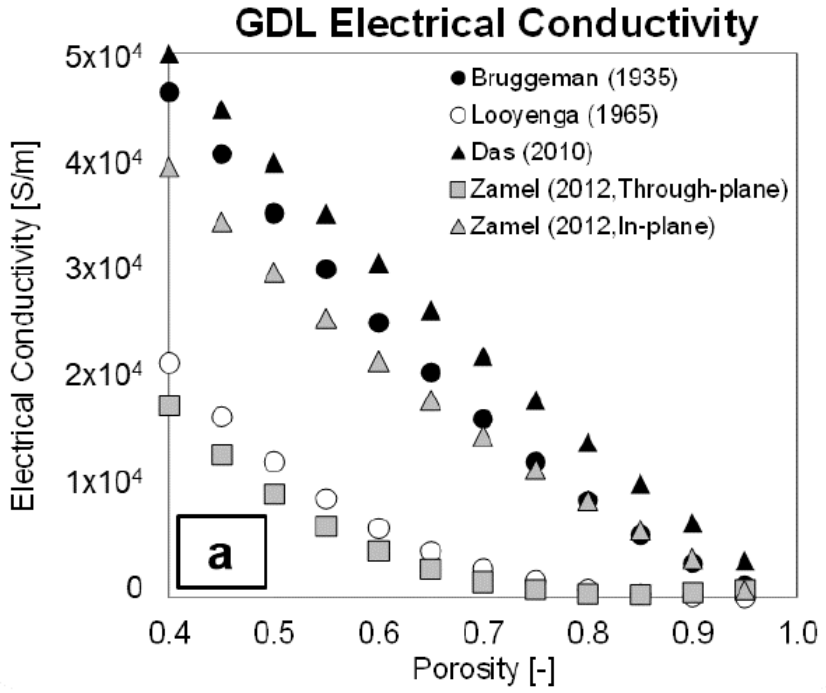

Figure 6 - Correlations for GDL electrical conductivity [2]

Similarly, protonic charge conservation is crucial in the electrolyte phase, where protons generated at the anode must be transported through the membrane to the cathode. The conservation of protonic charge in the electrolyte is described by:

$$\nabla(\kappa^{eff}\nabla\Phi_s) + S_{\Phi_s} = 0 \qquad \text{Eq. 30}$$

where κ^{eff} denotes the effective protonic conductivity of the membrane, Φ_s is the protonic potential, and S_{Φ_s} is the source term representing the proton generation and consumption rates at the electrode interfaces. This equation ensures that the movement of protons through the electrolyte is balanced with the generation and consumption processes at the electrodes, thereby maintaining charge neutrality.

The interplay between electric and protonic charge conservation is essential for the efficient operation of PEMFCs. Imbalances or disruptions in charge transport can lead to performance losses, such as increased overpotentials, reduced reaction rates, or localized degradation of cell components. Accurate modelling of charge conservation equations is

therefore critical for predicting the behavior of the fuel cell under various operating conditions and for optimizing its design and performance.

The electrolyte protonic conductivity κ^{eff} can be calculated using several correlations reported in *Table 2*.

Table 2 - Correlations for membrane protonic conductivity κ^{eff} [S/m]

Ref.	Correlation	Notes
[57]	$\kappa^{eff} = (0.5139\lambda - 0.326)e^{1268\left(\frac{1}{303}-\frac{1}{T}\right)}$	
[58]	$\kappa^{eff} = (1.72\lambda - 2.26)e^{2000\left(\frac{1}{303.15}-\frac{1}{T}\right)}$	
[59]	$\kappa^{eff} = 0.5738\lambda - 0.7192$	

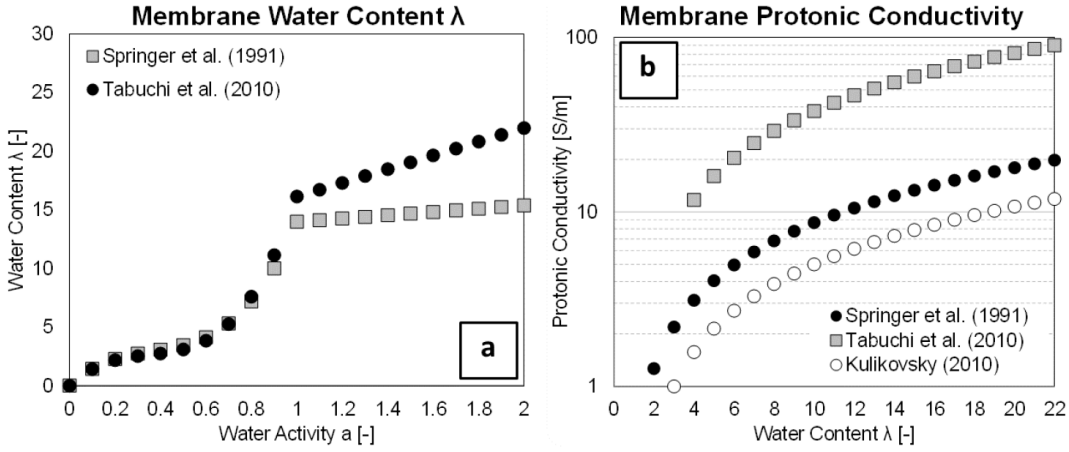

Figure 7 - Left: Correlations for the membrane water content λ as a function of the water activity. Right: Membrane protonic conductivity κ^{eff} as a function of water content

It is evident that the water content λ plays a crucial role in determining the effective protonic conductivity κ^{eff} of the electrolyte. The membrane's hydration state is defined

by the number of H_2O molecules per SO_3^- group, commonly referred to as the water content λ, which reaches approximately 20 for fully hydrated Nafion membranes. This parameter is closely linked to the water concentration in the membrane ionomer (c_{H2O} [kmol/m³]), the membrane's dry density ($\rho_{m,dry}$ [kg/m³]), and its equivalent weight (EW [kg/kmol]), as described in Eq 31. At equilibrium, the water content in the membrane is typically related to local water activity through an algebraic expression, with specific examples provided below in *Table 3* and depicted in *Figure 7*. These results demonstrate strong consistency in under-saturated conditions (a < 1), while deviations are observed in over-saturated conditions (a > 1).

$$\lambda = \frac{EW}{\rho_{m,dry}\, c_{H_2O}} \qquad \text{Eq. 31}$$

$$a = \frac{p_{H_2O}}{p_{sat,H_2O}} = \frac{x_{H_2O}\, p_{abs}}{p_{sat,H_2O}} \qquad \text{Eq. 32}$$

where p_{H_2O} represents the partial pressure of the water vapour.

Table 3 - Correlations for membrane equilibrium water content λ

Ref	Correlation	Notes
[57]	$\lambda = \begin{cases} 0.043 + 17.81a - 39.85a^2 + 36.0a^3 , & for\ 0 < a < 1 \\ 14 + 1.4(a-1) & for\ 1 \le a \le 3 \end{cases}$	
[26]	$\lambda = \begin{cases} 0.3 + 6a[1 - \tanh(a-0.5)] + 3.9\sqrt{a}\left[1 + tanh\left(\frac{a-0.89}{0.23}\right)\right] + s(\lambda_{s=1} - \lambda_{a=1}) & for\ s \le 0 \\ 16.8 + \lambda_{a=1}(1-s) & for\ s > 0 \end{cases}$	$\lambda_{s=1}$ = 16.8 is the water content at saturation and $\lambda_{a=1}$ is the value obtained when s = 1 and a = 1.
[58]	$\lambda = \begin{cases} 0.03 + 18.43a - 46.67a^2 + 44.36a^3 , & for\ 0 < a < 1 \\ 16.15 + 5.85(a-1) & for\ 1 \le a \le 3 \end{cases}$	

3.3 Introduction to Porous Media

Porous media are materials composed of a solid matrix interspersed with interconnected voids or pores. These pores allow the passage of fluids—liquids or gases—through the material, making the study of porous media essential in various fields such as petroleum engineering, groundwater hydrology, chemical engineering, environmental science, and biomedical engineering. Understanding and accurately modelling fluid flow, solute transport, and other processes in porous media are crucial for optimizing performance and addressing challenges in these areas [60].

Porous media modelling involves capturing the intricate interactions between the fluid phases and the solid matrix. These interactions are influenced by several key properties of the porous medium, including porosity, permeability, and tortuosity. This chapter provides a comprehensive overview of porous media modelling, focusing on the mathematical formulations and modelling approaches for permeability and tortuosity, two critical parameters that govern fluid flow and transport within these media.

3.3.1 Fundamental Concepts in Porous Media

Before delving into the mathematical models, it is essential to understand some fundamental concepts related to porous media:

1. **Porosity (ϕ)**: Porosity is the fraction of the total volume of a porous medium that is occupied by pores or voids. It is defined as:

$$\varepsilon = \frac{V_p}{V_t} \qquad \text{Eq. 33}$$

where V_p is the volume of the pores, and V_t is the total volume of the porous medium.

2. **Permeability (K)**: Permeability measures the ability of a porous medium to transmit fluids. It is influenced by the pore size, shape, connectivity, and the presence of multiple fluid phases. Permeability is typically expressed in units of square meters (m^2).

3. **Tortuosity (τ)**: Tortuosity is a dimensionless parameter that describes the complexity of the flow paths through the porous medium. It is defined as the ratio

of the actual path length that a fluid particle travels through the pores to the straight-line distance between the two points. Higher tortuosity indicates more convoluted pathways, which can impede fluid flow and affect transport properties such as permeability and diffusivity.

4. **Saturation (S)**: Saturation represents the fraction of the pore volume occupied by a particular fluid phase. In a two-phase system, the sum of the saturations of the wetting phase (S_w) and the non-wetting phase (S_{nw}) equals one:

$$S_{nw} + S_w = 1 \quad \text{Eq. 34}$$

5. **Capillary Pressure (P_c)**: Capillary pressure is the pressure difference between two immiscible fluid phases within the porous medium. It is influenced by the surface tension of the fluids, the contact angle, and the pore geometry.

6. **Darcy's Law**: Darcy's law is the fundamental equation that describes fluid flow through a porous medium. For a single-phase fluid, Darcy's law is expressed as:

$$\boldsymbol{u} = -\frac{k}{\mu}\nabla P \quad \text{Eq. 35}$$

where $\boldsymbol{u}$ is the Darcy velocity (volumetric flow rate per unit area), k is the permeability, μ is the dynamic viscosity of the fluid, and ∇P is the pressure gradient.

3.3.2 Permeability in Porous Media

Permeability is a key parameter in porous media modelling, as it quantifies the ease with which fluids can flow through the pore spaces. It is an intrinsic property of the medium, determined by the pore structure, including the size, shape, and connectivity of the pores. Understanding and accurately modelling permeability is crucial for predicting fluid flow in various applications [2].

Factors Affecting Permeability

Several factors influence the permeability of a porous medium:

- **Pore Size and Distribution**: Larger and more interconnected pores generally lead to higher permeability, as they provide less resistance to fluid flow.
- **Pore Shape and Geometry**: Irregular or elongated pores can reduce permeability by increasing the resistance to flow.
- **Porosity (ε)**: Higher porosity usually results in higher permeability, as more void space is available for fluid flow.
- **Tortuosity (τ)**: Higher tortuosity, which indicates more convoluted flow paths, generally reduces permeability.
- **Grain Size and Sorting**: Well-sorted materials with uniform grain sizes tend to have higher permeability compared to poorly sorted materials.
- **Compaction and Deformation**: Compaction can reduce pore space (porosity) and connectivity, leading to lower permeability, as can be seen in *Figure 8.*

Mathematical Models for Permeability

Several mathematical models have been developed to describe and predict permeability in porous media and are shown in *Table 4* and *Figure 8*.

Table 4 - Correlations for GDL permeability K [m^2].

Ref	Correlation	Notes
[61]	$K = e^{\left[\frac{-12.95+13.9\varepsilon}{1+1.57\varepsilon-2.22\varepsilon^2}\right]d^2}$	
[62]	$K = 0.012(1-\varphi)\left[\left(\frac{\pi}{4\varphi}\right)^2 - 2\frac{\pi}{4\varphi} + 1\right]\left[1 + 0.72\frac{\varphi}{(0.89-\varphi)^{0.54}}\right]$	
[63]	$K = \frac{\varepsilon}{8(ln\varepsilon)^2}\left[\frac{(\varepsilon-\epsilon_p)^{\alpha+2}}{(1-\varepsilon)^{\alpha}[(\alpha+1)\varepsilon-\epsilon_p]}\right]d^2$	$\epsilon_p = 0.11$ $\alpha = 0.521\ (2D\ parallel\ flow)$ $\alpha = 0.758\ (2D\ normal\ flow)$
[64]	$K = 0.0065\frac{\varepsilon^{3.6}}{67.2(1-\varepsilon)^2}d^2$	
[31]	$K = \frac{\varepsilon^3}{67.2(1-\varepsilon)^2}d^2$	

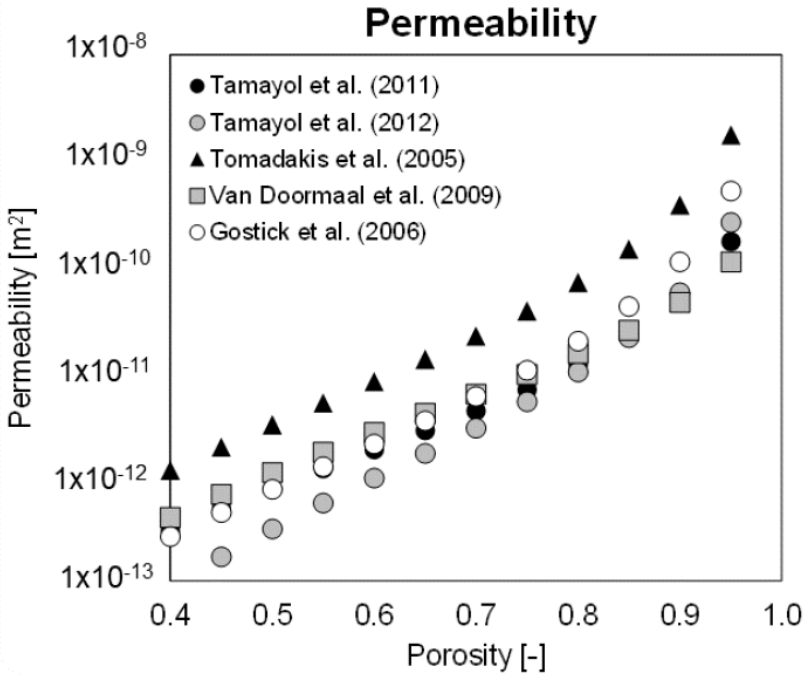

Figure 8 - Correlations for GDL permeability from Table 4 [2].

3.3.3 Tortuosity in Porous Media

Tortuosity is another critical parameter in porous media that describes the deviation of fluid flow paths from a straight line due to the complex pore structure. Tortuosity influences various transport properties, including permeability, diffusivity, and electrical conductivity.

Definition and Importance of Tortuosity

Tortuosity (τ) is defined as the ratio of the actual path length that a fluid particle or solute travels through the pores to the straight-line distance between the two points:

$$\tau = \frac{L_{actual}}{L_{straight}} \qquad \text{Eq. 36}$$

Higher tortuosity indicates more convoluted pathways, which can impede fluid flow and reduce transport efficiency. This property is used to scale the diffusivity coefficients of species in porous media to mimic the effect of the un-modelled solid phase occupation and structure, thus effectively reducing the diffusion transport rate.

Several correlations can be used to calculate the tortuosity, as shown in *Table 5* and *Figure 9*.

Table 5 - Correlations for porous medium tortuosity τ

Ref	Correlation	Notes
[55]	$\tau = \left(\frac{1}{\varepsilon}\right)^{0.5}$	
[66]	$\tau = 1 + 0.72\frac{1-\varepsilon}{(\varepsilon - 0.11)^{0.54}}$	
[63]	$\tau = \left(\frac{(1-0.11)}{(\varepsilon - 0.11)}\right)^{\alpha}$	$\alpha = 0.521\ (2D\ parallel\ flow)$ $\alpha = 0.758\ (2D\ normal\ flow)$

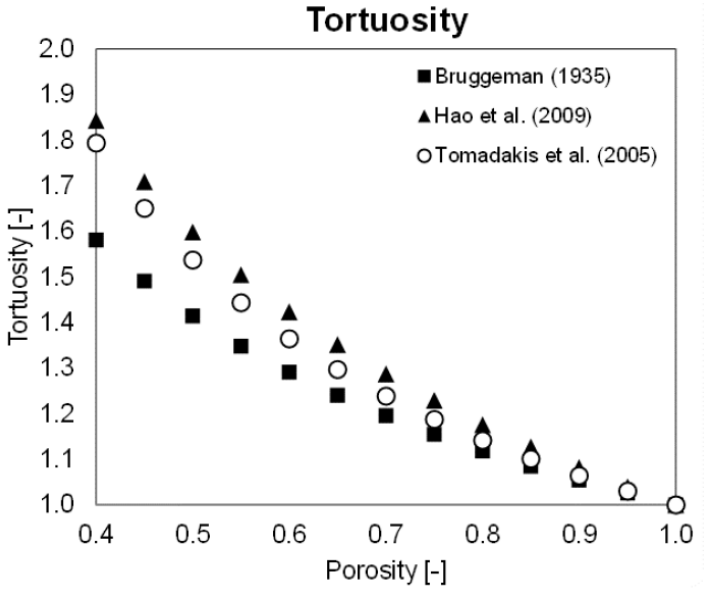

Figure 9 - Correlations for porous medium tortuosity τ from Tabel 5

Impact of Tortuosity on Transport Properties

Tortuosity affects several key transport properties:

- **Permeability**: Higher tortuosity increases the resistance to fluid flow, thereby reducing permeability. This relationship is captured in modified forms of the Carman-Kozeny equation.
- **Diffusivity**: Tortuosity reduces the effective diffusivity (D_{eff}) of solutes in the porous medium, as longer and more complex paths slow down diffusion:

$$D_{eff} = \frac{D}{\tau^2} \quad \text{Eq. 37}$$

3.4 Modelling Approaches for Catalyst Layers (CL)

Understanding and accurately modelling the catalyst layers (CL) in proton exchange membrane fuel cells (PEMFCs) and electrolyzers (PEMECs) is essential for optimizing their performance and efficiency. The CL is a critical component where electrochemical reactions occur, and its complex structure presents significant challenges for modelling. Over the years, researchers have developed several approaches to represent the CL, each varying in complexity and computational demands. These methods offer different levels of insight into the electrochemical and transport processes within the CL, and selecting the appropriate model depends on the specific objectives of the study.

3.4.1 Ultra-Thin Layer Model

One of the simplest approaches is the Ultra-Thin Layer Model. This model assumes that the catalyst layer has negligible thickness, effectively treating it as an infinitely thin interface where electrochemical reactions take place at the contact between the membrane and the gas diffusion layer (GDL). This simplification significantly reduces computational effort, making it attractive for simulations of entire fuel cells or stacks, especially when computational resources are limited. For example, Berning and Djilali

[29] utilized this model to analyze the effects of parameters such as GDL porosity and thickness on cell performance. However, the ultra-thin layer model has notable limitations. By neglecting the finite thickness and microstructural complexities of the CL, it cannot capture detailed phenomena such as reactant diffusion, ionic conduction, and water management within the layer. This oversimplification may lead to an overestimation of current density due to the assumption of idealized reaction conditions. Therefore, while the ultra-thin layer model is computationally efficient, it may not provide accurate predictions in cases where the properties and behavior of the CL significantly influence performance [2].

3.4.2 Macro-Homogeneous Model

To address some of these limitations, the Macro-Homogeneous Model, also known as the pseudo-homogeneous model, offers a more detailed representation of the CL by considering its finite thickness. This model treats the catalyst layer as a continuous medium with averaged properties, accounting for the presence of multiple components such as platinum catalysts, carbon support, solid GDL matrix, and ionomer electrolyte. By incorporating the finite thickness, the macro-homogeneous model allows for the analysis of gradients in concentration, potential, and temperature across the CL. It uses effective transport coefficients to represent the influence of the microstructure on mass and charge transport. This makes it suitable for studying the impact of material properties and operating conditions on fuel cell performance. However, the macro-homogeneous model assumes a uniform distribution of materials, which means it neglects the discrete nature of the microstructure. It cannot resolve detailed interactions at the nanoscale between catalyst particles, ionomer, and pores. Despite this, the macro-homogeneous model strikes a balance between computational efficiency and model fidelity, and it has been widely used in PEMFC simulations [2] [65].

3.4.3 Agglomerate Model

For a more comprehensive and physically representative approach, the Agglomerate Model considers the complex composition and structural distribution of materials within the CL by modelling it as a collection of agglomerates [67] [68] [69] [70]. Each agglomerate consists of catalyst particles—platinum supported on carbon—and is

surrounded or infiltrated by the ionomer [68] [70]. This model captures microstructural details that are critical for understanding the CL's behavior. Within the agglomerates, there are primary pores, which are internal pores that may be filled with ionomer or liquid water. These pores significantly affect the diffusion of reactants to the active sites. Between the agglomerates are the secondary pores, which facilitate the transport of gases and liquid water. The filling of these pores influences mass transport and water management within the CL [71].

The agglomerate model considers transport phenomena in detail. Reactant diffusion occurs through multiple pathways, including ionomer-filled regions, liquid water, and void spaces. Additionally, the model addresses liquid water dynamics by examining the generation and movement of liquid water within the CL, which can impact performance and durability. Variations of the agglomerate model provide different perspectives on these processes. For instance, the model proposed by Nam and Kaviany [72] assumes that primary pores are filled with ionomer, and reactant diffusion occurs in the dissolved phase. In this model, secondary pores may be partially or fully filled with liquid water, affecting the overall transport properties. Alternatively, the model by Xing [68] [70] suggests that liquid water generation begins in the primary pores, filling them before it occupies the secondary pores as a thin film around agglomerates. This sequential filling process impacts the effective diffusivity and the availability of reactants, thereby influencing the cell's performance.

The agglomerate model offers significant advantages by providing detailed insights into the interplay between microstructure and performance. It can predict the effects of various material properties, such as ionomer content, agglomerate size, and porosity, on electrochemical reactions and transport processes. However, this model is computationally intensive due to its complexity. It also requires detailed knowledge of the CL microstructure, which may necessitate advanced characterization techniques that are not always readily available [68] [70].

Selecting the appropriate modelling approach requires an understanding of the strengths and limitations of each method in relation to the study's objectives. The Ultra-Thin Layer Model is best suited for system-level simulations where computational speed is critical,

and detailed CL phenomena have a minimal impact on the overall performance. It allows researchers to explore general trends and perform quick analyses but may not be suitable for in-depth studies of the CL itself.

The Macro-Homogeneous Model offers a good compromise between detail and computational demand. It is appropriate for studies focusing on the effects of CL thickness, material properties, and operating conditions on fuel cell performance. This model allows for the investigation of gradients within the CL and can capture the influence of changes in material composition and structure to a certain extent.

The Agglomerate Model is ideal for in-depth analysis of the CL microstructure and its impact on performance. It is particularly useful for optimizing CL design, selecting appropriate materials, and understanding degradation mechanisms. By considering the detailed microstructural features and transport processes, the agglomerate model can provide valuable insights that inform the development of more efficient and durable fuel cells [68] [69] [70] .

3.4.4 Catalyst Layer Modelling in PEMFCs and PEMECs

In the CL, species creation and destruction are governed by the species transport equation, which incorporates a source term S_i to account for the consumption and production of chemical species. For a hydrogen/air PEMFC following electrochemical reactions:
$H_2 \rightarrow 2H^+ + 2e^-$ (Anode)

$2H^+ + 2e^- + \frac{1}{2}O_2 \rightarrow H_2O$ (Cathode)

The source terms for hydrogen, oxygen, and water vapor are expressed as [2]:

$$S_{H_2,a} = -\left(\frac{M_{H_2}}{2F}\right) j_a; \quad S_{H_2O,a} = -M_{H_2O}\left(\frac{n_d j_a}{F}\right) \qquad \text{Eq. 38}$$

$$S_{O_2,c} = -\left(\frac{M_{O_2}}{4F}\right) j_c; \quad S_{H_2O,c} = M_{H_2O}\left(\frac{n_d j_c}{F}\right) + \left(\frac{M_{H_2}}{2F}\right) j_a \qquad \text{Eq. 3}$$

Here:

- M_{H_2} and M_{O_2} are the molar masses of hydrogen and oxygen.
- F is Faraday's constant.
- j_a and j_c are the anodic and cathodic current densities.
- n_d is the electro-osmotic drag coefficient, representing the number of water molecules dragged per proton conducted.

The source term S_{H_2O} includes the water flux due to electro-osmotic drag from anode to cathode, which is a significant factor affecting membrane hydration and overall cell performance.

3.4.4.1 Liquid Water Effect

In modelling the CL, it is essential to account for the presence of liquid water, which can block pores and impede gas transport. The effective diffusion coefficient D_i^{eff} for species i is adjusted using the Bruggeman correlation, modified to include the liquid water volume fraction s:

$$D_i^{eff} = D_{i,0}\varepsilon^{1.5}(1-s)^{1.5} \quad \text{Eq. 40}$$

- $D_{i,0}$ is the diffusion coefficient in the bulk gas phase.
- ε is the porosity of the CL.
- s represents the saturation level of liquid water within the pores.

This modification acknowledges that liquid water reduces the effective porosity available for gas diffusion, thereby affecting reactant transport to the active sites.

3.4.4.2 Charge Conservation and Potential Distribution

The charge conservation equations for the electronic (solid) and ionic (electrolyte) phases are given by:

$$\nabla \cdot (\sigma^{eff}\nabla\Phi_s) - S_{\Phi_s} = 0 \quad \text{Eq. 41}$$

$$\nabla \cdot (\kappa^{eff} \nabla \Phi_e) + S_{\Phi_e} = 0 \quad \text{Eq. 42}$$

- σ^{eff} and κ^{eff} are the effective conductivities of the electronic and ionic phases, respectively.
- Φ_s and Φ_e are the potentials of the solid and electrolyte phases.
- S_{Φ_s} and S_e are source terms representing the transfer of charge due to electrochemical reactions.
-

3.4.4.3 Electrochemical Kinetics: Butler–Volmer Equations

The kinetics of the anodic and cathodic reactions are described by the Butler–Volmer equations:

Anode Reaction (Hydrogen Oxidation Reaction, HOR):

$$H_2 \rightarrow 2H^+ + 2e^-$$

$$j_a = \zeta_a j_{0,a}^{ref} \left(\frac{c_{H_2}}{c_{H_2}^{ref}} \right)^{\gamma_a} \left[e^{\left(\frac{\alpha_a F \eta_a}{RT} \right)} - e^{\left(\frac{\alpha_c F \eta_a}{RT} \right)} \right] \quad \text{Eq. 43}$$

Cathode Reaction (Oxygen Reduction Reaction, ORR):

$$^1/_2\, O_2 + 2H^+ + 2e^- \rightarrow H_2O$$

$$j_c = \zeta_c j_{0,c}^{ref} \left(\frac{c_{O_2}}{c_{O_2}^{ref}} \right)^{\gamma_a} \left[-e^{\left(\frac{\alpha_a F \eta_c}{RT} \right)} + e^{\left(\frac{\alpha_c F \eta_c}{RT} \right)} \right] \quad \text{Eq. 44}$$

- $j_{0,a}^{ref}$ and $j_{0,c}^{ref}$ are the reference exchange current densities at the anode and cathode.
- ζ_a and ζ_c are the specific active surface areas.
- η_a and η_c are the overpotentials at the anode and cathode, defined as $\eta = \Phi_s - \Phi_e - E^{eq}$, where E^{eq} is the equilibrium potential.
- α_a and α_c are the anodic and cathodic charge transfer coefficients.

- γ_a and γ_c are reaction order coefficients, representing the dependence on reactant concentration.

The specific active surface area ζ is critical as it directly affects the reaction rates. It is determined by:

$$\zeta = \frac{A_s m_{pt}}{\delta_{CL}} \quad \text{Eq. 45}$$

- A_s is the catalyst surface area per unit mass, which depends on the platinum particle size and dispersion.
- m_{pt} is the platinum loading.
- δ_{CL} is the thickness of the catalyst layer.

The catalyst-specific surface area A_s strongly depends on different types of supported catalysts and platinum black. Nevertheless, it may be approximated in terms of the platinum mass fraction f (in this case A_s $[\frac{m^2}{g_{Pt}}]$) [2] as in Eq. 46

$$A_s = (227.79f^3 - 158.57f^2 - 201.53f + 159.5) \cdot 10^3 \quad \text{Eq. 46}$$

Advancements in catalyst technology, such as the use of nano-sized platinum particles and alternative catalyst supports, can significantly increase A_s , enhancing fuel cell performance.

3.4.4.4 Exchange Current Density and Temperature Dependence

The exchange current density j_0 is a fundamental parameter reflecting the intrinsic activity of the electrode reaction. For the cathode, an empirical correlation with temperature T is given by:

$$log_{10}\left(j_{0,c}^{ref}\right) = 3.507 - \frac{4001}{T} \quad \text{Eq. 47}$$

This relationship highlights the exponential increase in $j_{0,c}^{ref}$ with temperature, emphasizing the importance of thermal management in PEMFCs [73].

3.4.4.5 Charge Transfer Coefficients and Tafel Slopes

In fuel cells, activation polarization often governs overall performance, and a key way to describe it is via the Tafel equation. This equation applies at sufficiently large overpotentials, where one exponential term in the Butler–Volmer equation dominates. In such cases, the *activation overpotential*, ΔV_{act}, relates linearly to the logarithm of the current density, i:

$$\Delta V_{act} = a + b\ log(i) \qquad \text{Eq. 48}$$

where a depends on the exchange current density i_0 and b is the Tafel slope. The Tafel slope quantifies how many millivolts of additional overpotential are needed for each tenfold increase in current, and can be expressed as [1]:

$$b = \frac{2.3RT}{\alpha F} \qquad \text{Eq. 49}$$

where R is the gas constant, T is the absolute temperature, F is the Faraday constant, and α is the charge-transfer coefficient.

A critical aspect of this approximation is that it holds best at *larger* overpotentials—once the overpotential rises above tens of millivolts, one exponential term in the Butler–Volmer equation becomes dominant. At lower overpotentials, near equilibrium, both exponentials can matter, and the simpler Tafel form no longer accurately describes the behavior. Nevertheless, once the Tafel regime is reached, plotting ΔV_{act} vs. log(i) yields a straight line whose slope (b) can be used to infer fundamental kinetic parameters, including the exchange current density and the charge-transfer coefficient.

In practice, **charge-transfer coefficients** α_a and α_c at the anode and cathode determine how sensitively the reaction rate responds to changes in overpotential. For example, the hydrogen oxidation reaction (HOR) at the anode often has $\alpha_a \approx 0.5$, indicating a relatively symmetric energy barrier. Meanwhile, the oxygen reduction reaction (ORR) at the

cathode is more sensitive to temperature and potential, causing α_c (and hence the Tafel slope) to vary. At low overpotentials (i.e., high cell voltages), the Tafel slope is typically around 60 mV dec^{-1}, corresponding to $\alpha_c \approx 1$. As the overpotential increases (cell voltage drops), the Tafel slope can rise to about 120 mV dec^{-1}, indicating a decrease in α_c.

The temperature dependence of α_c in these higher-slope regimes has been quantified empirically. For instance, [74] proposes:

$$\alpha_c = 0.495 + 2.3 \cdot 10^3 \cdot (T - 300) \quad \text{Eq. 50}$$

or alternatively [75],

$$\alpha_c = 0.001678\, T \quad \text{Eq. 51}$$

These expressions indicate that α_c increases with temperature, leading to a lower Tafel slope and enhanced reaction rates at elevated temperatures.

4 Single-Channel PEM Fuel Cell

PEM fuel cells have a simple structure, devoid of moving mechanical components, which makes them suitable for discretisation using structured calculation grids. However, this simplicity is countered by the intricate nature of the physical and electrochemical processes that require modelling. In order to mathematically represent a PEM fuel cell accurately, several aspects must be taken into account, including multiphase flows involving multiple gas species, the kinetics of multiphase electrochemical reactions, electric and ionic charge transport, and energy transfer.

This chapter presents the mathematical model used in this thesis research, which incorporates simplified phase interactions and electrochemical reaction kinetics. Initially, the assumptions necessary for the simplification of the model are provided, followed by the derivation of the conservation equations governing the different transport processes and the models used for the different phenomena.

In this work, a macro-homogeneous modelling approach is adopted to simulate the catalyst layer (CL) of the fuel cell. This approach effectively homogenizes the intricate microstructure of the catalyst layer into a continuum, where averaged transport properties and reaction kinetics are used to represent the overall behaviour of the porous medium. In the commercial CFD software STAR-CCM+, while robust capabilities exist for modelling porous media and fluid flow, there is no built-in functionality to directly implement surface reactions within a porous matrix.

To overcome this limitation, user-defined field functions were developed and integrated into the simulation. These functions are used to incorporate the source and sink terms associated with the electrochemical reactions, specifically, the hydrogen oxidation reaction (HOR) at the anode, the oxygen reduction reaction (ORR) at the cathode (see Eqs. 64 - 66), as well as the sorption/desorption processes of water vapor and liquid water. The user-defined functions allow us to model the production and consumption of species within the catalyst layer by defining localized reaction rates as additional source terms in the species conservation equations.

Furthermore, the active catalytic surface area, critical for accurately capturing the reaction kinetics, is parameterized as a function of the platinum loading. This is achieved by expressing the specific active surface (ζ) in terms of the platinum loading (m_{pt}), the electrochemical active surface area A_s and the catalyst layer thickness (δ_{CL}) as shown in Eq. 73. By linking ζ directly to m_{pt}, the model can be easily adjusts the effective reaction surface area to reflect changes in the catalyst composition, thereby enhancing the fidelity of the simulation in representing the electrochemical performance of the fuel cell.

The mathematical formulation implemented in the commercial code is detailed in the following paragraphs.

4.1 Assumptions

In order to mathematically describe the physical and electrochemical phenomena in a PEM fuel cell (PEMFC), certain assumptions have been made to facilitate numerical simulations without compromising the general characteristics of the cell:

- The gases are considered ideal.
- Due to the low velocities, the flow is assumed to be laminar.
- The membrane is a solid component that is impermeable to the passage of gaseous species; therefore, crossover is neglected.
- The porous media (GDL and CL) are assumed to be isotropic and homogeneous.
- The effect of gravity is ignored.

4.2 Governing Equations

For multiphase flow modelling, the Mixture Multi-Phase (MMP) model approach is used, which assumes the presence of several miscible and equilibrium phases and that their motion can be simulated as that of a single continuum. In particular, a continuity, momentum, and energy equation are solved for the Eulerian mixture (e.g., the mixture density ρ_m or the mixture velocity vector $\boldsymbol{u_m}$ are considered), and the phases subdivision is handled by a dedicated transport equation for the volume fraction. The phase relative

velocity is calculated by the model and it is used to numerically investigate multiphase processes in PEMFC. The governing equations for the MMP model (Eqs. 52-57) are synthesised in *Table 6*, together with the region-dedicated source term specification.

Table 6 – Governing Equations Mixture Multiphase Model

Continuity equation:		$\nabla(\rho_m \boldsymbol{u_m}) = S_m$		Eq. 52
CH	GDL	CL	MEM	BP
$S_m = 0$	$S_m = 0$	$S_m = \sum_k S_k$	$\boldsymbol{u_m} = \boldsymbol{0}$ $S_m = 0$	$\boldsymbol{u_m} = \boldsymbol{0}$ $S_m = 0$
Momentum equation:		$\frac{1}{\varepsilon^2}\nabla(\rho_m \boldsymbol{u_m}\,\boldsymbol{u_m}) = -\nabla p + \nabla\left(\frac{\mu}{\varepsilon}\nabla \boldsymbol{u_m}\right) + \boldsymbol{S_u}$		Eq. 53
CH	**GDL**	**CL**	**MEM**	**BP**
$\boldsymbol{S_u} = \boldsymbol{0}$	$\boldsymbol{S_u} = -\frac{\mu}{K_{GDL}}\boldsymbol{u_m} + \boldsymbol{f_p} + \boldsymbol{f_u}$	$\boldsymbol{S_u} = -\frac{\mu}{K_{GDL}}\boldsymbol{u_m} + \boldsymbol{f_p} + \boldsymbol{f_u}$	$\boldsymbol{u_m} = \boldsymbol{0}$ $\boldsymbol{S_u} = \boldsymbol{0}$	$\boldsymbol{u_m} = \boldsymbol{0}$ $\boldsymbol{S_u} = \boldsymbol{0}$
Species transport:		$(\rho_m Y_i \boldsymbol{u_m}) = \nabla\left(D_i^{eff}\nabla Y_i\right) + S_i$		Eq. 54
CH	**GDL**	**CL**	**MEM**	**BP**
$S_i = 0$	$S_i = 0$	$S_{H_2} = -\frac{M_{H_2}}{2F} j_a$ (an) $S_{H_2O} = -S_d$ (an) $S_{O_2} = -\frac{M_{O_2}}{4F} j_c$ (cat) $S_{H_2O} = \frac{M_{H_2O}}{2F} j_c + S_d$ (cat)	$S_i = 0$	$S_i = 0$ $Y_i = 0$
Energy transport:		$\nabla\left(\left(\rho_m c_p\right)^{eff} T \boldsymbol{u_m}\right) = \nabla(k^{eff}\nabla T) + S_T$		Eq. 55
CH	**GDL**	**CL**	**MEM**	**BP**
$S_k = 0$	$S_k = 0$	$S_T = \frac{i_s^2}{\sigma^{eff}} + \frac{i_e^2}{\kappa^{eff}} + j_a\eta_{act} + j_a\frac{T\Delta S}{2F}$ (an) $S_T = \frac{i_s^2}{\sigma^{eff}} + \frac{i_e^2}{\kappa^{eff}} + j_c\eta_{act} + j_c\frac{T\Delta S}{2F}$ (cat)	$S_T = \frac{i_e^2}{\sigma^{eff}}$	$S_T = \frac{i_s^2}{k^{eff}}$
Charge transport :		$\nabla(\sigma^{eff}\nabla\Phi_s) + S_{\Phi_s} = 0$ $\nabla(\kappa^{eff}\nabla\Phi_e) + S_{\Phi_e} = 0$		Eq. 56 Eq. 57
CH	**GDL**	**CL**	**MEM**	**BP**
$\Phi_s = 0$; $\Phi_e = 0$	$S_{\Phi_s} = 0$; $S_{\Phi_e} = 0$	$S_{\Phi_s} = -j_a$; $S_{\Phi_e} = j_a$ (an) $S_{\Phi_s} = j_c$; $S_{\Phi_e} = -j_c$ (cat)	$S_{\Phi_s} = 0$; $S_{\Phi_e} = 0$	$S_{\Phi_s} = 0$; $S_{\Phi_e} = 0$

4.3 Porous Media

A macro-homogeneous approach is employed to model porous media, where the intricate and detailed fibrous structure of the material is disregarded. Instead, corrective terms are utilized to simulate the overall impact of the solid phase on a larger scale. Specifically, the porosity (ε), which represents the statistical ratio of pores to the total volume, and the tortuosity (τ), which represents the statistical ratio of the convoluted path to the straight-line distance (as calculated in Eq. 58 and Eq. 59 [66]), are utilized to modify (decrease) the local diffusivity of species when they are transported in the GDL and CL. This modification replicates the more challenging delivery of reactants (or removal of products) at the CL.

$$\varepsilon = \frac{V_f}{V_f + V_s} = \frac{V_f}{V_t} \quad \text{Eq. 58}$$

$$\tau = 1 + 0.72\frac{1-\varepsilon}{(\varepsilon-0.11)^{0.54}} \quad \text{Eq. 59}$$

Where V_f represents the volume occupied by the fluid and V_s the volume occupied by the solid.

The resistance imposed by the porous medium on the fluid is characterized by two components: viscous and inertial, which are combined in Equation 60. The non-linear inertial term is disregarded due to the low velocities involved, while the viscous term is computed for the n-th phase by considering its viscosity ($\mu_{(n)}$), the material permeability (K), and the relative permeability (K_{rl}), as shown in Equation 61. The relative permeability signifies the extent to which the presence of other phases in the pore space obstructs a particular phase, and it is formulated according to Eq. 62, with a value of k = 4, as indicated in references [58][76].

$$\boldsymbol{f_p} = -(\boldsymbol{P_{vis}} + \boldsymbol{P_{in}} \cdot |\boldsymbol{u_m}|) \cdot \boldsymbol{u_m} \quad \text{Eq. 60}$$

$$\boldsymbol{P_{vis}} = \frac{\mu_{(n)}}{K K_{rl}} \boldsymbol{I} \quad \text{Eq. 61}$$

$$K_{rl,n} = \alpha_{(n)}{}^{k} \quad \text{Eq. 62}$$

Another source term is added to the momentum equation to account for the capillary force in the porous media, represented as a vector source ($\boldsymbol{f_u}$) for each n-th phase in the presence of the other m-th phase (in this case gas and liquid). Since there is limited experimental data available, the capillary pressure is estimated using Leverett's function (Eq. 63), which takes into account the gas-liquid surface tension (s) and assumes a contact angle (θ_c) of 110° [58]. It's worth noting that Leverett's function was originally derived for different types of porous media, such as homogeneous solids and sandy beds. For more detailed information on this topic, Wu et al. [77] provide relevant insights. It should be mentioned that previous studies have explored several formulations of capillary pressure [78][79], considering the contact angle. In this case, the formulation is suitable for contact angles (θ_c) greater than 90°.

$$\boldsymbol{f_{u\,(n)}} = \alpha_{(n)}\alpha_{(m)} s\, cos\left(\frac{\theta_c\, \pi}{180}\right) \cdot \sqrt{\frac{\varepsilon}{\tau}} \nabla \left[1.417\left(1-\alpha_{(n)}\right) - 2.120\left(1-\alpha_{(n)}\right)^2 + 1.263\left(1-\alpha_{(n)}\right)^3\right]$$
Eq. 63

4.4 Catalyst Layer Modelling

As stated, a macro-homogeneous model is implemented via user coding within a multi-dimensional CFD code to simulate the catalyst layer. This approach retains the finite thickness of the CL while employing average transport coefficients to account for spatial variations in compositional parameters. Unlike GDL modelling, which typically considers a single solid phase for electron transport, CL modelling must account for two distinct solid phases: the conductive carbon phase for electronic transport and the ionomer phase (analogous to the membrane material) for ionic transport. By adopting the macro-homogeneous approach, the model simulates electrochemical reactions on an effective internal surface of the solid-fluid interface that is statistically determined rather than assuming a planar reaction area.

The hydrogen oxidation reaction (HOR) at anode and the oxygen reduction reaction (ORR) at cathode are implemented as in Eqs. 64, 65 and 66, where the indices represent the gas (g), liquid (l), Pt/C (s) and ionomer (i). It is worth noting that cathode half-reaction is distinguished between the water formation in the liquid/vapour phases, based on the local pressure level.

$$H_{2(g)} \leftrightarrow 2H^{+}_{(i)} + 2e^{-}_{(s)} \quad \text{Eq. 64}$$

$$\frac{1}{2}O_{2(g)} + 2H^{+}_{(i)} + 2e^{-}_{(s)} \leftrightarrow H_2O_{(g)} \quad \text{if } p < p_{sat} \quad \text{Eq. 65}$$

$$\frac{1}{2}O_{2(g)} + 2H^{+}_{(i)} + 2e^{-}_{(s)} \leftrightarrow H_2O_{(l)} \quad \text{if } p > p_{sat} \quad \text{Eq. 66}$$

Where the pressure saturation is calculated as in Eq. 67 [49]:

$$p^{sat} = 101325 \cdot 10^{\left[-2.1794+0.02953(T-273)-9.1837\cdot10^{-5}\cdot(T-273)^2+1.445\cdot10^{-7}(T-273)^3\right]} \quad \text{Eq. 67}$$

In relation to the species conservation equation, the source terms for water production is represented by the term S_d. This term considers the sorption/desorption process of dissolved water from the ionomer phase to either the liquid or gas phase, as in the Eqs. 68, 69 and 70.

$$S_d = S_{ld} + S_{vd} \quad \text{Eq. 68}$$

$$S_{ld} = \gamma_l \frac{\rho_m}{EW}\left(\lambda_{eq} - \lambda\right) \quad \text{Eq. 69}$$

$$S_{gd} = \gamma_g \frac{\rho_m}{EW}\left(\lambda_{eq} - \lambda\right) \quad \text{Eq. 70}$$

Where ρ_m is the density of the ionomer phase $[\frac{kg}{m^3}]$ and EW the equivalent weight.

Whereas, for the production of water and the consumption of oxygen and hydrogen due to the development of electrochemical reactions, volumetric transfer currents j_c and j_c are used, calculated by the Butler-Volmer Equation for anode and cathode as in Eq. 71 and 72.

$$j_c = (1-s)\,\zeta \cdot i_{0,c}^{ref} \cdot \left(\frac{c_{O_2}}{c_{O_2}^{ref}}\right)^{\gamma_c} \cdot \left[-e^{\left(\frac{\alpha_a F \eta_c}{RT}\right)} + e^{\left(-\frac{\alpha_c F \eta_c}{RT}\right)}\right] \quad \text{Eq. 71}$$

$$j_a = (1-s)\,\zeta \cdot i_{0,a}^{ref} \cdot \left(\frac{c_{H_2}}{c_{H_2}^{ref}}\right)^{\gamma_a} \cdot \left[e^{\left(\frac{\alpha_a F \eta_a}{RT}\right)} - e^{\left(-\frac{\alpha_c F \eta_a}{RT}\right)}\right] \quad \text{Eq. 72}$$

Where i_0^{ref} is the exchange current density $[\frac{A}{m^2}]$.

A user-defined functions has been implemented to dynamically calculate the hydrogen and oxygen concentration in the catalyst layer, used for the modelling of Eq. 71 and Eq. 72.

The term $\zeta\ [m^{-1}]$ represents the specific active surface of the catalyst, which is modelled as in Eq. 73:

$$\zeta = \frac{A_s m_{pt}}{\delta_{CL}} \qquad \text{Eq. 73}$$

Where A_s is the electrochemical active surface area $[\frac{m^2}{g_{pt}}]$ calculated with Eq. 46, m_{pt} the platinum loading $[\frac{g_{pt}}{m^2}]$ and δ_{CL} the thickness [m] of the CL.

4.5 Membrane

As stated in the assumptions, the membrane is treated as a solid component that does not allow the passage of gaseous species, effectively excluding the crossover phenomenon. However, it allows the movement of ions and dissolved water through the absorbed phase via the electro-osmotic effect. The ionic conductivity is determined using the correlation proposed by Springer et al. [46] (Eq. 74), which takes into account the membrane's water content (λ_{eq}) and temperature. The equilibrium water content of the membrane is expressed as shown in Eq. 75, where the water activity in the layer adjacent to the membrane (a) is calculated based on the water concentration (c_w) (through the Eq. 76).

$$\sigma^{eff} = (0.5139\lambda - 0.326) \cdot \exp\left[1268\left(\frac{1}{303} - \frac{1}{\mathrm{T}}\right)\right] \qquad \text{Eq. 74}$$

$$\lambda_{eq} = \begin{cases} 0.043 + 17.81a - 39.85a^2 + 36.0a^3 for\ 0 < a < 1 \\ 14 + 1.4(a-1) \quad for\ 1 \leq a \leq 3 \end{cases} \qquad \text{Eq. 75}$$

$$a = \frac{c_w RT}{p^{sat}} \qquad \text{Eq. 76}$$

Once water is absorbed in the ionomer phase, its transport follows a diffusion-type model using an experimentally derived [80] water diffusivity correlation for the dissolved phase (D_w) as in Eq. 77.

$$D_w = 4.1 \cdot 10^{-10} \left(\frac{\lambda}{25}\right)^{0.15} \left[1 + tanh\left(\frac{\lambda - 2.5}{1.4}\right)\right] \quad \text{Eq. 77}$$

The next chapter presents the 3D model and explains how the mathematical model can be applied to three-dimensional geometry. The chapter illustrates the following:

- Introduction of the geometries, calculation grids and operational parameters used in the simulations.
- Description of the initial and boundary conditions of each domain.
- Modified geometry and parameters for the case of compressed porous media.
- Validation of the model and analysis of the results obtained.

4.6 Computational Model

The simulations were carried out using the commercial software STAR-CCM+ v2020.1 by SIEMENS SISW [47]. To validate the model, numerical results were compared against experimental data from Tabuchi et al. [58], focusing on two specific geometries: one with a channel-to-rib spacing of 1 mm/1 mm and the other with 0.4 mm/0.4 mm, referred to as Case 1 and Case 2, respectively. The layout of these geometries and their key dimensions are illustrated in *Figure 10*.

The computational mesh consisted of approximately 4.3 million hexahedral cells for Case 1 and 1.9 million cells for Case 2, with 128,000 and 55,000 cells allocated to each CL, respectively. These mesh configurations were determined through mesh independence tests to ensure that the solutions were unaffected by further mesh refinement. Future studies will explore coarser grids, particularly along the axial direction, following the recommendations provided in [81]. *Table 7* details the main cell dimensions, which align

with those documented in [58]. Inlet and outlet regions were extended by 5 mm on each side to allow fully developed flow conditions within the primary domain. Conformal interfaces were established at all contact points between components.

The boundary conditions applied include symmetry planes at the lateral boundaries of the electrodes and membrane, and a volumetric flow rate of 2 L/min with 90% relative humidity for both anode and cathode inlets, consistent with the conditions reported in [58]. The outer surfaces of the bipolar plates were maintained at a fixed temperature of 353 K to simulate the liquid cooling effects described in the reference study [58]. The outlet pressure was set at 250 kPa. Detailed material properties and electrochemical parameters are provided in *Tables 8 and 9*. The external surfaces of the bipolar plates were treated as equipotential surfaces, with potential values set to Φ_S=0 for the anode and cathode, respectively, and the voltage difference (ΔV) was varied between 0.3 V and 0.9 V in 0.1 V increments. For models incorporating the effects of porous media compression, modifications were made both at the geometric level (simulating compression in land areas) and by adjusting the local material properties accordingly.

4.6.1 Model Input Parameters

The mathematical model is constrained by various parameters. The input parameters of the current model can be roughly grouped into three kinds: the structural parameters (*Table 7*), the electrochemical kinetic parameters (*Table 8*), the physical and thermal parameters (*Table 9*).

Table 7 - Geometrical dimensions from [58].

Component dimensions	**Value**
Channel length	10 mm
Channel height	0.5 mm
Channel width	1 mm/0.4mm (Case 1/2)
BPP width	2 mm/0.8mm (Case 1/2)
BP height	1 mm
GDL thickness	200 μm

CL thickness	10 μm
Membrane thickness	30 μm

Table 8 - Electrochemical properties from [58].

	Anode	**Cathode**
Electrochemical Reactions	$H_{2(g)} \leftrightarrow 2H^{+}_{(m)} + 2e^{-}_{(s)}$	$\frac{1}{2}O_{2(g)} + 2H^{+}_{(i)} + 2e^{-}_{(s)} \leftrightarrow H_2O_{(l)}$ $\frac{1}{2}O_{2(g)} + 2H^{+}_{(i)} + 2e^{-}_{(s)} \leftrightarrow H_2O_{(g)}$
Pt Loading m_{Pt}	0.4 mg_{Pt}/cm^2	0.4 mg_{Pt}/cm^2
Electrochemical active surface A_s	58000 m^2/kg_{Pt}	58000 m^2/kg_{Pt}
Charge transfer coefficients	α_a=1 α_c=1	α_a=1 α_c=1

Table 9 - Physical and transport properties from [58]

Physical properties of FC main components		**Value**
GDL	Density (solid phase)	2250 kg/m^3
	Electrical Conductivity	500 S/m
	Thermal Conductivity	10 W/m/K
	Permeability	$4 \cdot 10^{-12}$ m^2
	Contact angle θ_c	110°
	Porosity ε_{GDL}	0.7
CL	Porosity ε_{CL}	0.5
	Permeability	$4 \cdot 10^{-13}$ m^2
	Contact angle θ_c	110°
Ionomer	Density	2000 kg/m^3
	Ionic Conductivity	Eq. 12
	Specific Heat	903.0 J/kg/K
	Thermal Conductivity	0.445 W/m/K
	Volume Fraction	0.2
Pt/C	Density	2250.0 kg/m^3
	Electrical Conductivity	500.0 S/m
	Specific Heat	707.68 J/kg/K

	Th. Conductivity	10 W/m/K
	m_{Pt}	0.004 kg/m^2
	Active Surface	58000 m^2/kg
BPP	Density	2250 kg/m^3
	Electrical Conductivity	20000 S/m
	Specific Heat	707.68 J/kg/K
	Thermal Conductivity	20 W/m/K
Membrane	Density	2000 kg/m^3
	Ionic Conductivity	Eq. 7
	Specific Heat	903 J/kg/K
	Thermal Conductivity	0.445 W/m/K

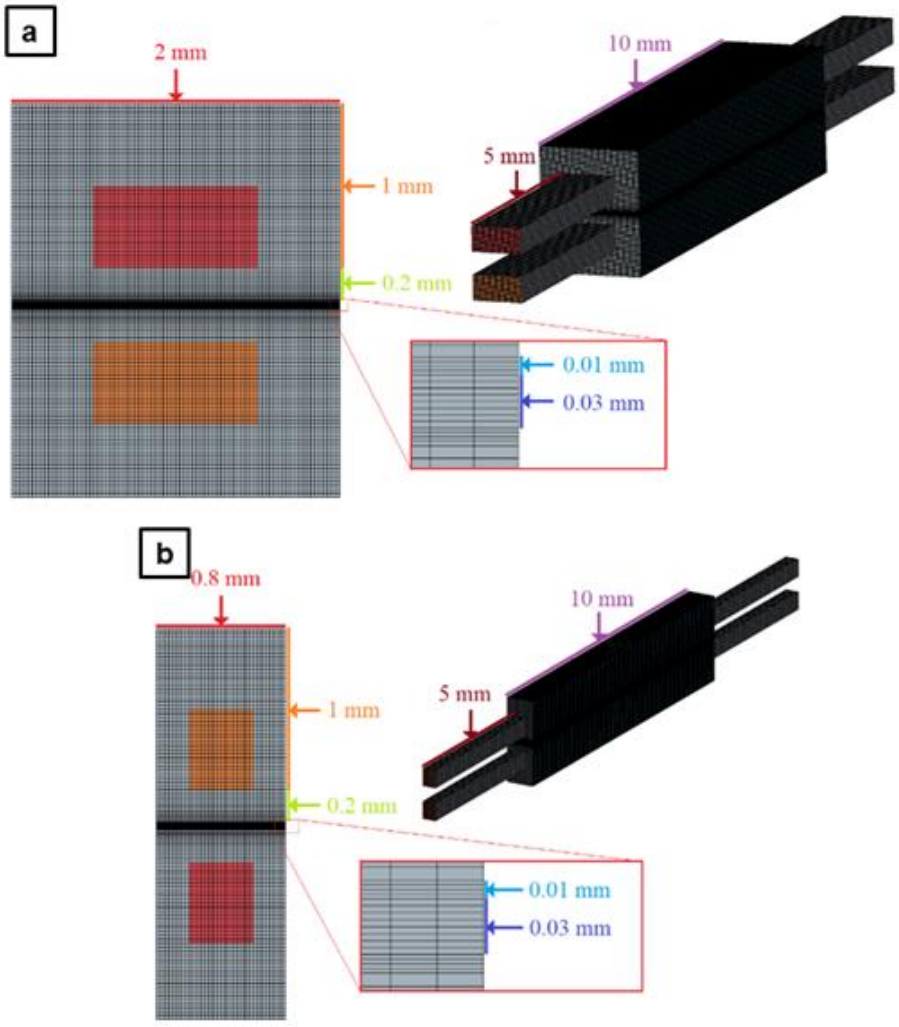

Figure 10 - Computational domain with main dimensions and finite volume mesh: a) Case 1 (1mm/1 mm), b) Case 2 (0.4mm/0.4 mm).

4.6.2 Modified geometry - Inhomogeneous compression

One of the effects neglected by most multi-dimensional PEMFC models is the influence of the porous media deformation, caused by the compressive force of the BPPs. The externally applied clamping pressure causes an alteration of GDL/CL porosity, with local effects on all the transport processes. However, to some extent this is mandatory to prevent gas leakage, hence it cannot be excluded. From a local perspective, the compression of the porous medium in the land zone causes a local reduction of the porosity and an increase in anisotropy, while its value remains almost unchanged in the subchannel zone. This phenomenon can be easily understood by observing *Figure 11*. Nitta et al. [82] experimentally investigated the inhomogeneous compression of the GDL under the BPP compression, measuring the alteration of several properties and deriving formulations for the variation in permeability, contact resistance, electrical and thermal conductivity. As no experimental data are available concerning the inhomogeneous compression of the diffusive layers of the analysed cell, the correlations proposed in [82] and used in [83] for a specific GDL (380 μm thick GDL) are here normalized to be applied to a 200 μm thick GDL and extended to a 10 μm thick CL. This allows a numerical analysis of the effect that the deformation of the porous layers has on the performance of the cell. As stated, the logarithmic trend proposed in [83] was inherited in this study to derive the GDL/CL thickness in the deformed state as in Eq. 78, where h_{compr} represents the GDL thickness in the land zone and $h(x) = h_0 = 200\ \mu m$ in the axial channel region. The study is carried out on two different compression ratios, expressed as $CR = \frac{h_{compr}}{h_0}$, namely CR=0.66 and CR=0.5. This means that the thickness in the compressed zone is 66% and 50% of the nominal *ex-situ* value.

$$h(x) = \begin{cases} h_{compr} \\ 19.30314\, ln[(x - 0.0005) \cdot 10^6 + 1] \cdot 10^{-6} + h_{compr} \end{cases} \quad \text{Eq. 78}$$

As already specified, the deformation locally modifies the porosity of the medium, which is calculated employing Eq. 79 [83], with h_{min} (Eq. 80) determined by the solid fibres' occupation $(1-\varepsilon_0)$, which is supposed to remain unchanged under compression.

It is worth mentioning that the pores will undergo strong deformation upon compression, the pores (initially spherical in shape) become ellipsoid. The properties of the GDL may undergo further changes as a result of this phenomenon.

$$\varepsilon(x) = \varepsilon_0 \frac{h(x)-h_{min}}{h_0-h_{min}} \qquad \text{Eq. 79}$$

$$h_{min} = (1-\varepsilon_0)h_0 \qquad \text{Eq. 80}$$

The variation of transport properties is applied also to the CL region, with the permeability of CL reduced by an order of magnitude to maintain the initial conditions. Permeability, electrical and thermal conductivity are differentiated into three zones based to reproduce the deformed/undeformed zone, as listed in *Table 8* and represented in *Figure 11* for the two analyzed CR:

Table 8 - Equations of permeability K(x) (top row), electrical conductivity k(x) (middle row), thermal conductivity k(x) (bottom row) for both cases analyzed CR 0.66 (left column) and CR 0.5 (right column).

CR=0.66	**CR=0.5**
$K(x) = \begin{cases} 3.04 \cdot 10^{-12}\ m^2 \quad if \quad 0 \le x \le 0.5mm \\ -1.700 \cdot 10^{-11} + 2.760 \cdot 10^{-7} h(x) - 1.484 \cdot 10^{-3} h(x)^2 + \\ 2.754 \cdot h(x)^3 + 3.128 \cdot 10^{-12} \\ if\ 0.5mm < x \le 0.53mm \\ 4 \cdot 10^{-12}\ m^2 \quad if \quad 0.53mm < x \le 1mm \end{cases}$ Eq. 81	$K(x) = \begin{cases} 1.64 \cdot 10^{-12}\ m^2 \quad if \quad 0 \le x \le 0.5mm \\ -1.700 \cdot 10^{-11} + 2.760 \cdot 10^{-7} h(x) - 1.484 \cdot 10^{-3} h(x)^2 + \\ 2.754 \cdot h(x)^3 + 3.128 \cdot 10^{-12} \\ if\ 0.5mm < x \le 0.675mm \\ 4 \cdot 10^{-12}\ m^2 \quad if \quad 0.675mm < x \le 1mm \end{cases}$ Eq. 84

$$\kappa(x) = \begin{cases} 636\ S/m & if\ 0 \le x \le 0.5mm \\ -6.140900 \cdot 10^{24}x^5 + 1.587296 \cdot 10^{22}x^4 \\ -1.641198 \cdot 10^{19}x^3 \\ +8.485023 \cdot 10^{15}x^2 - 2.193494 \cdot 10^{12}x + \\ 2.268323 \cdot 10^{8}\ S/m \\ if\ 0.5mm < x \le 0.53mm \\ 500\ S/m & if\ 0.53mm < x \le 1mm \end{cases} \quad \text{Eq. 82}$$

$$\kappa(x) = \begin{cases} 657\ S/m & if\ 0 \le x \le 0.5mm \\ -1.525283 \cdot 10^{22}x^5 + 4.596524 \cdot 10^{19}x^4 \\ -5.530371 \cdot 10^{16}x^3 \\ +3.320855 \cdot 10^{13}x^2 - 9.952847 \cdot 10^{9}x + \\ 1.191714 \cdot 10^{6}\ S/m \\ if\ 0.5mm < x \le 0.675mm \\ 500\ S/m & if\ 0.675mm < x \le 1mm \end{cases} \quad \text{Eq. 85}$$

$$k(x) = \begin{cases} 12.7\ W/(mK) & if\ 0 \le x \le 0.5mm \\ -1.228431 \cdot 10^{23}x^5 + 3.205952 \cdot 10^{20}x^4 \\ -3.346878 \cdot 10^{17} \\ x^3 + 1.747075 \cdot 10^{14}x^2 - 4.560098 \cdot 10^{10}x \\ +4.761253 \cdot 10^{6} \\ if\ 0.5mm < x \le 0.53mm \\ 10\ W/(mK) & if\ 0.53mm < x \le 1mm \end{cases} \quad \text{Eq. 83}$$

$$k(x) = \begin{cases} 13.14\ W/(mK) & if\ 0 \le x \le 0.5mm \\ -3.050567 \cdot 10^{20}x^5 + 9.193048 \cdot 10^{17}x^4 \\ -1.106074 \cdot 10^{15}x^3 \\ +6.641711 \cdot 10^{11}x^2 - 1.990569 \cdot 10^{8}x \\ +2.383429 \cdot 10^{4} \\ if\ 0.5mm < x \le 0.675mm \\ 10\ W/(mK) & if\ 0.675mm < x \le 1mm \end{cases} \quad \text{Eq. 86}$$

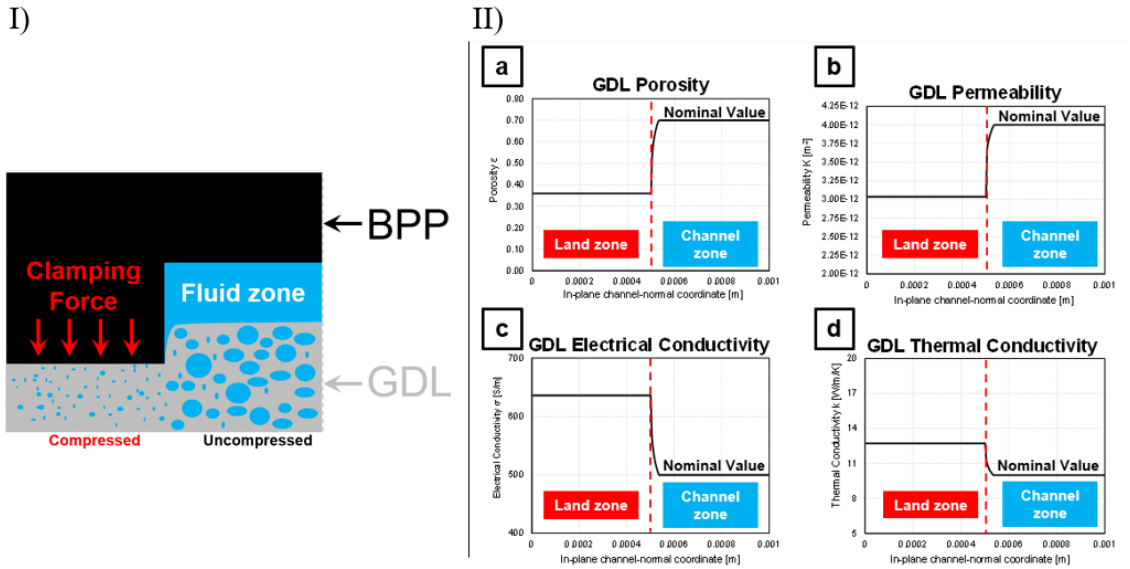

Figure 11 - I) Scheme of GDL compression by BPP under the assembly clamping force. II) Alteration of GDL porosity (a), permeability (b), electrical (c) and thermal conductivity (d) as a consequence of BPP compression.

4.7 Results

Figure 12 a) presents a comparison between the experimental polarization curves reported in the reference study [58] and the results from the current numerical simulations. The reference data were used as a baseline for the nominal (uncompressed) conditions, since the original numerical study did not take into account deformations in the presence of compressive forces and there are no data to assume the compressive effect. The 3D-CFD model accurately replicates the voltage-current behavior observed in both investigated cases.

For Case 1, the model effectively captures the pronounced impact of mass transport overpotentials, which lead to a sharp voltage drop at higher current densities. This effect is considerably less pronounced in Case 2, as observed in both experimental data and simulations. This trend is further supported by the overpotential analysis shown in *Figure 12(b)* at 2.5 $\frac{A}{cm^2}$, indicating a reduction in mass transfer overpotential for Case 2 (0.09 V) compared to Case 1 (0.13 V). The higher rib-to-channel ratio in Case 1 contributes to this disparity by hindering oxygen diffusion to the active sites beneath the land area, resulting in a longer diffusion path and reduced oxygen supply rates to the catalyst layer (CLc). This restriction creates a more pronounced oxygen-limited performance in Case 1 compared to the more closely spaced Case 2.

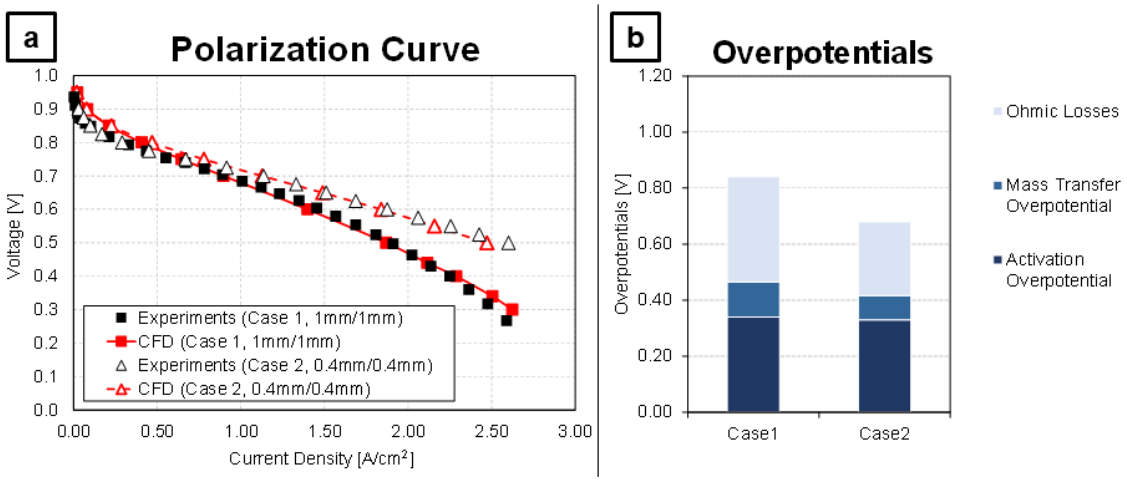

Figure 12 - Numerical and experimental polarization curves (a) and overpotential analysis (b) for Case 1 and 2.

Focusing on this oxygen transport limitation, *Figure 13 (a-b)* illustrates the spatial distribution of oxygen concentration at approximately 2.5 $\frac{A}{cm^2}$, corresponding to ΔV = 0.3V for Case 1 and ΔV= 0.5 V for Case 2. For Case 1, there is a significantly reduced oxygen concentration beneath the land zone, highlighting a reactant-limited scenario that is not evident in Case 2. At lower current densities, this limitation becomes less severe, as depicted in *Figure 13 (c-d)* at 2.0 $\frac{A}{cm^2}$ (ΔV=0.5 V for Case 1 and ΔV=0.6 V for Case 2) and *Figure 13 (e-f)* at 1.0 $\frac{A}{cm^2}$ (ΔV=0.7 V for both cases), where the reaction rate is comparatively lower.

Finally, the extent of oxygen supply limitation in Case 1 is further quantified in *Figure 14*, which shows the oxygen molar concentration at the GDLc/CLc interface along a mid-channel section for three different voltages. This comparison underscores the critical impact of geometric configuration on reactant availability and cell performance, particularly under high-demand conditions.

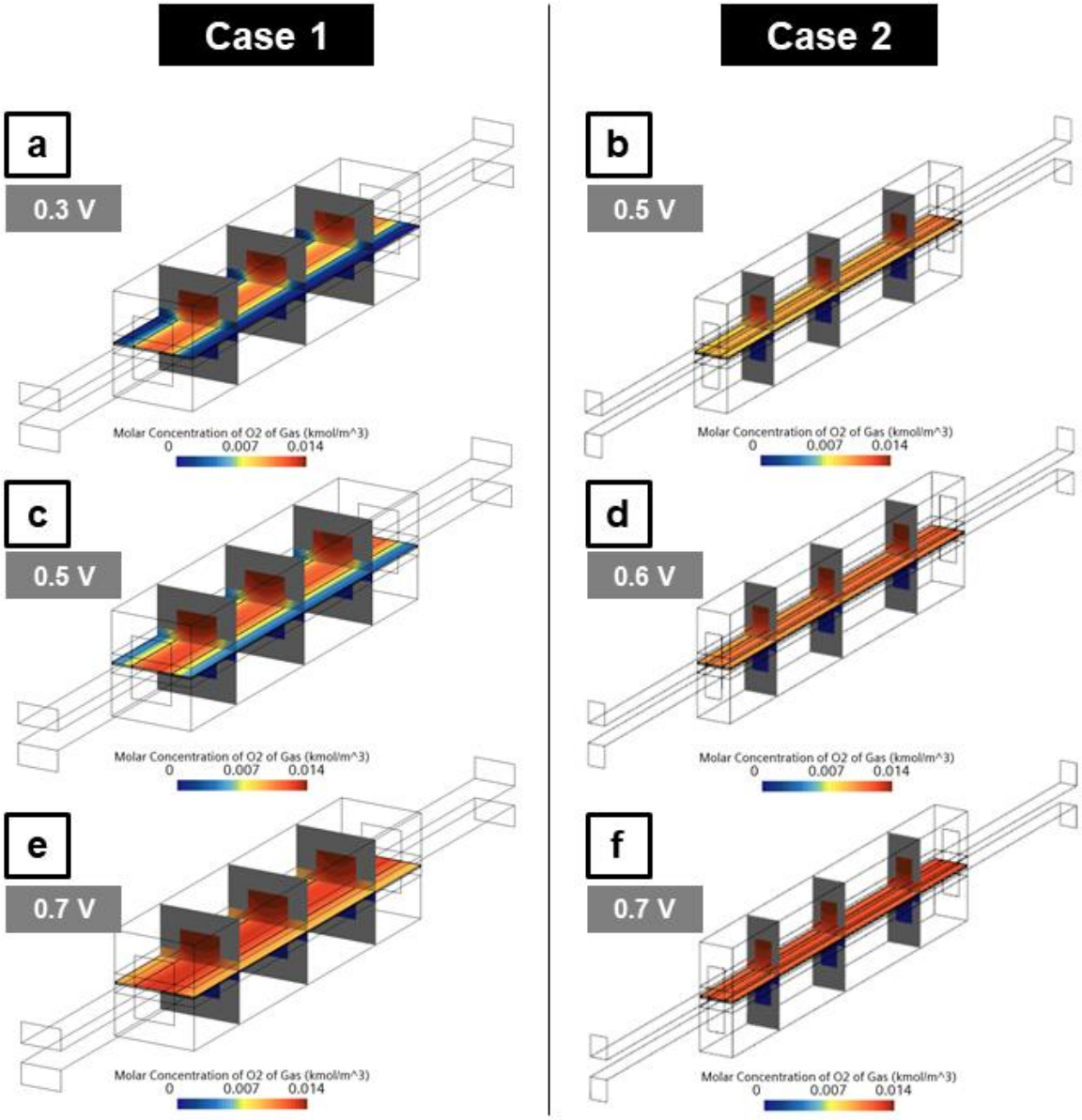

Figure 13 - Scalar field of molar concentration of O2 [kmol/m3] at 2.5 A/cm2 for Case 1/2 (a/b), at 2.0 A/cm2 for Case 1/2 (c/d) and at 1.0 A/cm2 for Case 1/2 (e/f).

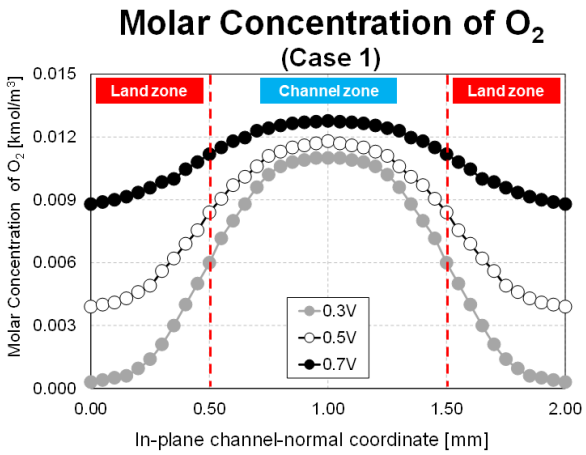

Figure 14 - Molar concentration of O2 [kmol/m3] at the GDLc/

Another important difference between the two cases can be seen in *Figure 12 (b)*, which shows that Case 2 exhibits reduced ohmic losses compared to Case 1. This reduction is not directly linked to the differences in reactant delivery discussed earlier. This observation was initially noted in the reference study [58] and is further explored here by examining the membrane water content (λ) and the effective ionic conductivity (σ^{eff}).

Specifically, the average membrane water content values for Cases 1 and 2 are λ=9.03 and λ=9.31, respectively, corresponding to ionic conductivities of $\sigma^{eff} = 8.02\ S/m$ and $\sigma^{eff} = 8.18\ S/m$ under the operating condition of 2.5 $\frac{A}{cm^2}$. Given that these models do not account for contact resistances, the ionic resistance of the membrane plays a dominant role in determining the overall cell resistance. This explains why Case 1 experiences higher ohmic losses.

Figure 15 illustrates the spatial distribution of membrane water content and ionic conductivity. For Case 1, there is a noticeable region of dehydration and reduced conductivity centered around the channel, which is absent in Case 2. This localized dehydration under the channel zone contributes significantly to the observed increase in ohmic losses for Case 1, highlighting the impact of channel and rib design on the membrane's hydration state and overall cell performance.

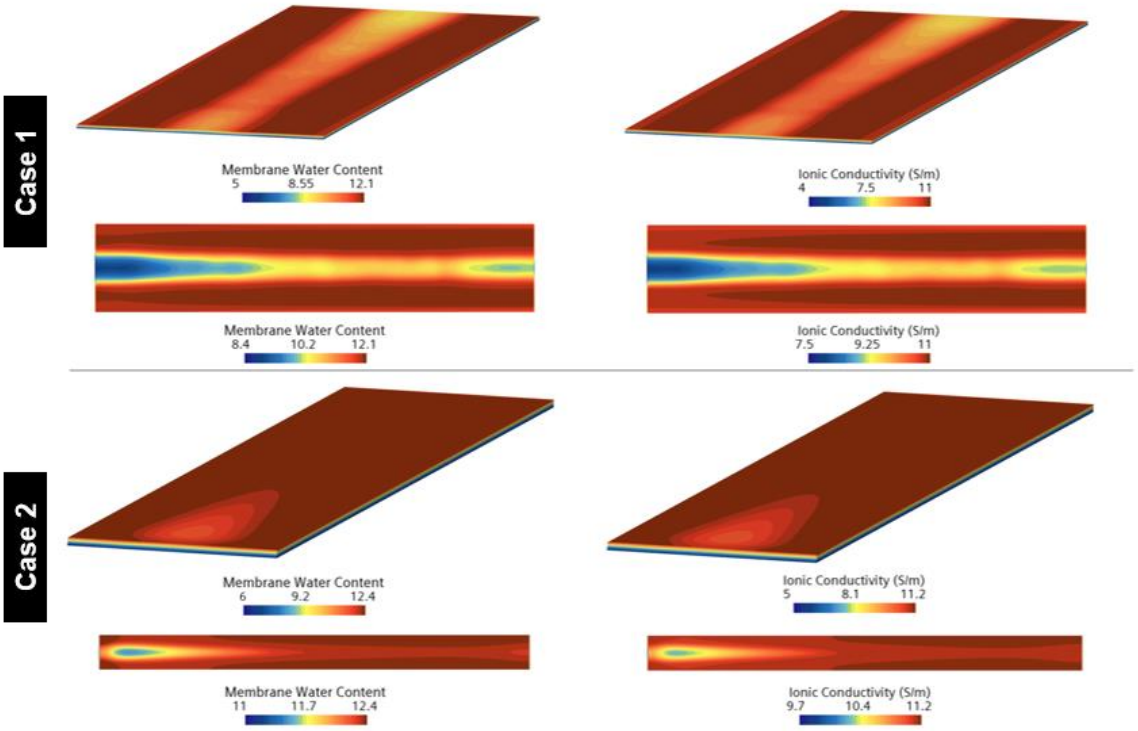

Figure 15 - Scalar fields of membrane water content and ionic conductivity [S/m] for Case 1 (top) and Case 2 (bottom) at 2.5 A/cm2. Isometric view and Top view of the membrane with higher minimum plot to better appreciate its distribution.

The enhanced membrane hydration observed in Case 2 can be attributed to a more uniform distribution of the liquid phase within the diffusive layers adjacent to the membrane, as depicted in *Figure 16.* This figure shows the distribution of the liquid volume fraction across three sections and at the CLc/MEM interface, illustrating how effective species transport to the CLc directly impacts ohmic losses.

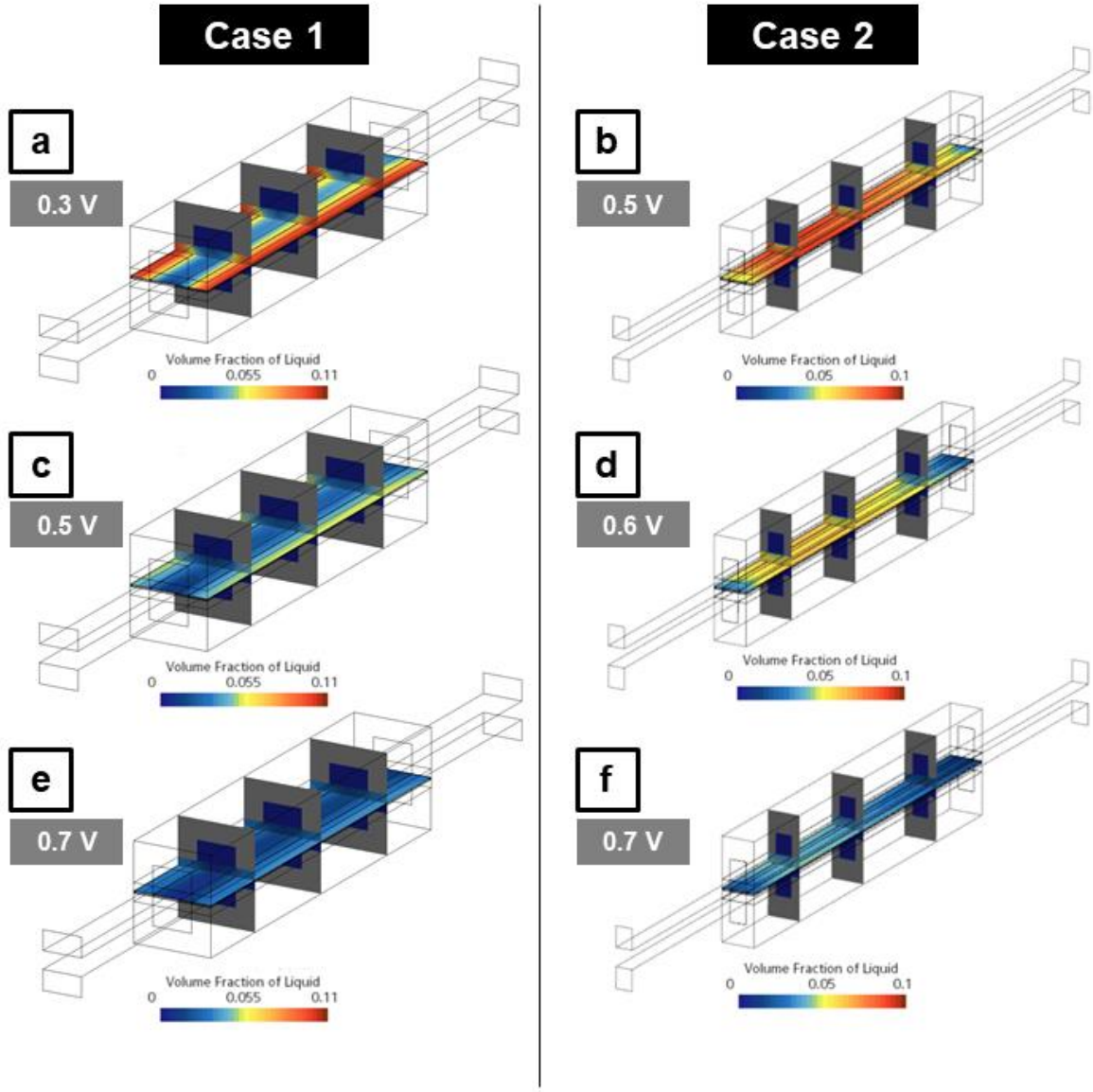

Figure 16 - Volume fraction of liquid water at 2.5 A/cm2 for Case 1/2 (a/b), at 2.0 A/cm2 for Case 1/2 (c/d) and at 1.0 A/cm2 for Case 1/2 (e/f).

However, it is important to note that polarization curves alone do not suffice for the complete validation of multidimensional PEMFC models. Identical overall cell outputs can be obtained even when individual sub-models are incorrectly parameterized, as highlighted in [84]. Consequently, a combination of global and local validation techniques is essential for high-fidelity CFD models, with particular emphasis on integrating comparisons with neutron radiography (NRG) visualizations, as demonstrated in previous studies [84].

Figure 17 compares the simulated distribution of liquid water in the GDLc/CLc and at the CLc/MEM interface with experimental NRG measurements from Ref. [58]. The strong quantitative agreement validates the macro-homogeneous modelling approach used for the porous components (GDL and CL). This level of accuracy was not achieved in earlier simulations using a thin-layer approach by other authors [86], underscoring the importance of comprehensive electrical and physical validation in the development of accurate PEMFC models.

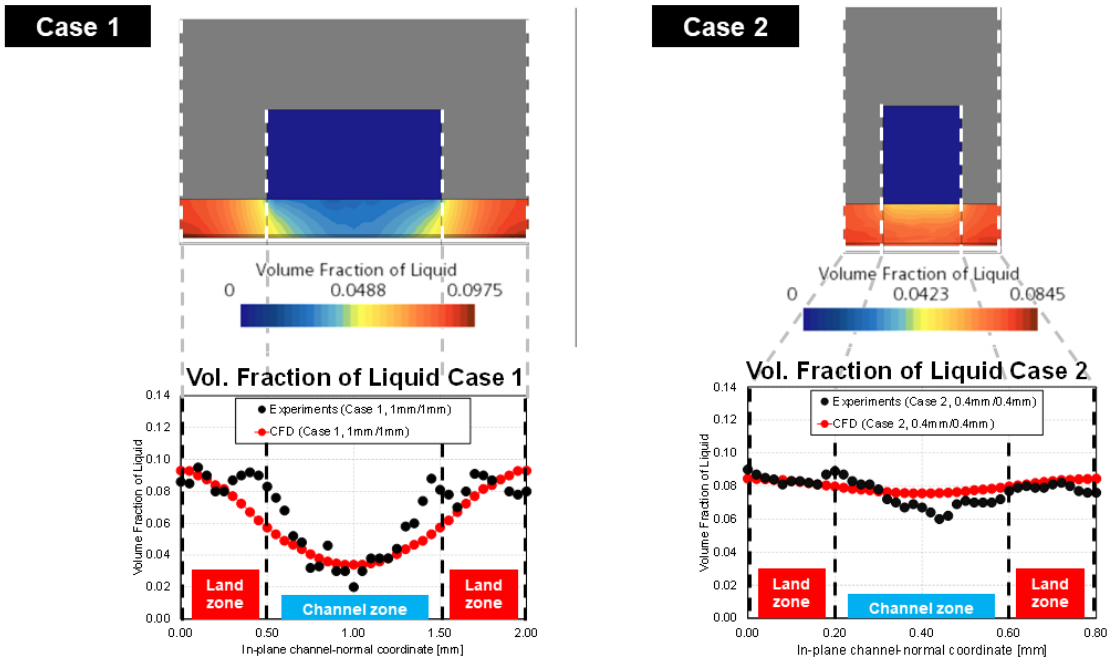

Figure 17 - Scalar field of the liquid volume fraction on a half-channel section and comparison of numerical and experimental results of the liquid volume fraction at the CLc/MEM interface on a half-channel section at 2.5 A/cm2.

4.7.1 Effect of Porous Parts Compression

The polarization curves under various compression conditions were analyzed exclusively for Case 1, as this configuration with a wider channel-to-rib spacing was selected to emphasize the potential differences resulting from modified material properties. *Figure 18* presents the polarization curves for the nominal case (CR = 1) and the compressed scenarios (CR = 0.66 and CR = 0.5, corresponding to thickness reductions in the compressed zone to 66% and 50% of the nominal ex-situ value, respectively). The results

reveal that increased compression of the deformable layers leads to a noticeable reduction in current density, particularly at higher current densities (above 1 $\frac{A}{cm^2}$).

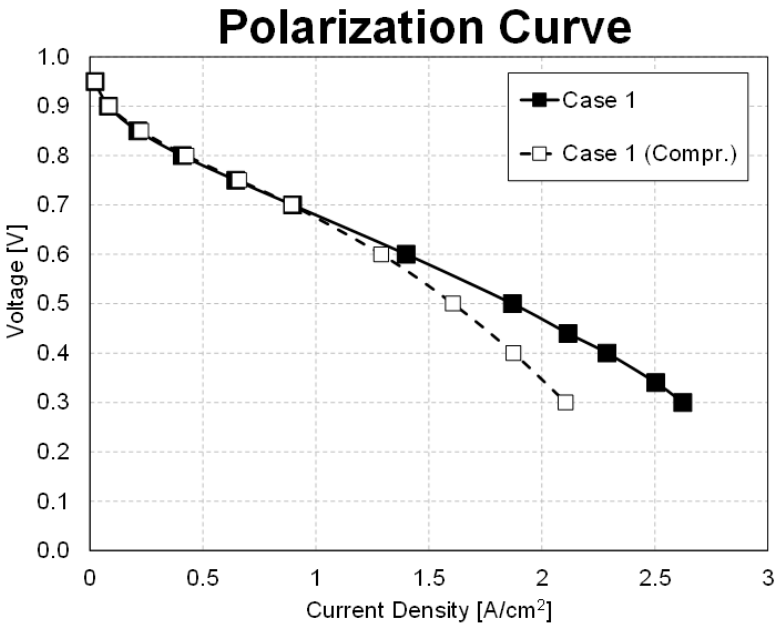

Figure 18 - Numerical polarization curves of Case 1 with CR 1 (underformed), CR 0.66 and CR 0.5.

The curves show that the compressed designs exhibit concentration-limited behavior significantly earlier than the undeformed case.

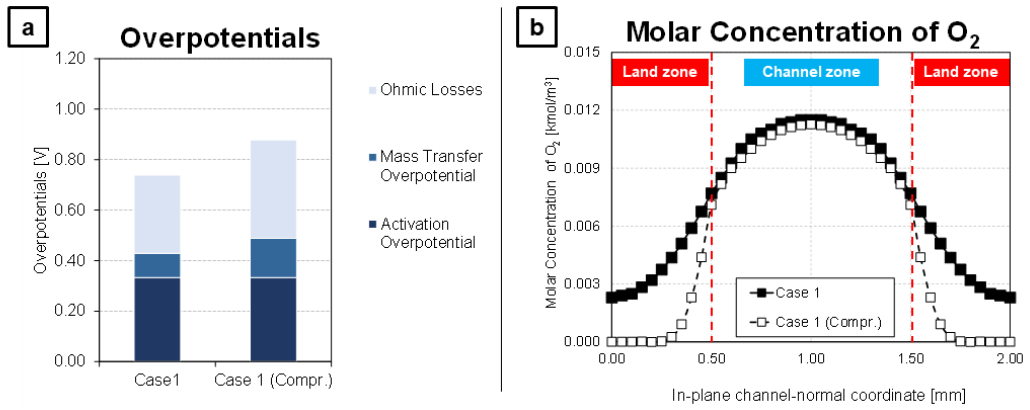

Figure 19 - a) Overpotential analysis and b) O2 molar concentration [kmol/m3] at CLc/MEM interface of Case 1 with CR 1, CR 0.66 and CR 0.5.

This behavior can be explained through an analysis of the overpotentials at a fixed current density of 1.85 $\frac{A}{cm^2}$, shown in *Figure 19 (a).* The results confirm that mass transfer overpotentials rise with increased GDL/CL compression, recorded at 0.087 V, 0.174 V, and 0.187 V for CR values of 1, 0.66, and 0.5, respectively. This increase is primarily attributed to the reduced porosity and increased tortuosity in the land zones, which leads to a localized decrease in permeability. Consequently, the resistance to reactant transport becomes a more critical and rate-limiting factor compared to the reference (uncompressed) model, which explains the premature drop in current density at the same voltage levels.

Figure 19 (b) further supports this conclusion by showing the oxygen molar concentration across an axial-orthogonal section. The figures clearly depict the oxygen deficiency in the land zones for both compressed cases, which is caused by restricted transport through the compressed, lower-permeability porous medium.

These factors significantly hinder the removal of liquid water generated in the CLc, as shown in *Figure 20 (right)* for the case with CR = 0.66. This increased water retention leads to greater occlusion of the pores within the CLc, further constraining mass transport and reducing the volume available for gaseous reactants. As a result, the oxygen concentration within the compressed zones drops to near zero, indicating the onset of mass transport limitations at the active sites. *Figure 20 (left)* illustrates the scalar field of oxygen molar concentration for Case 1 with CR = 0.66 across three different voltages, which can be directly compared to *Figure 13*. This visual comparison clearly confirms the lower oxygen concentration levels observed for CR = 0.66.

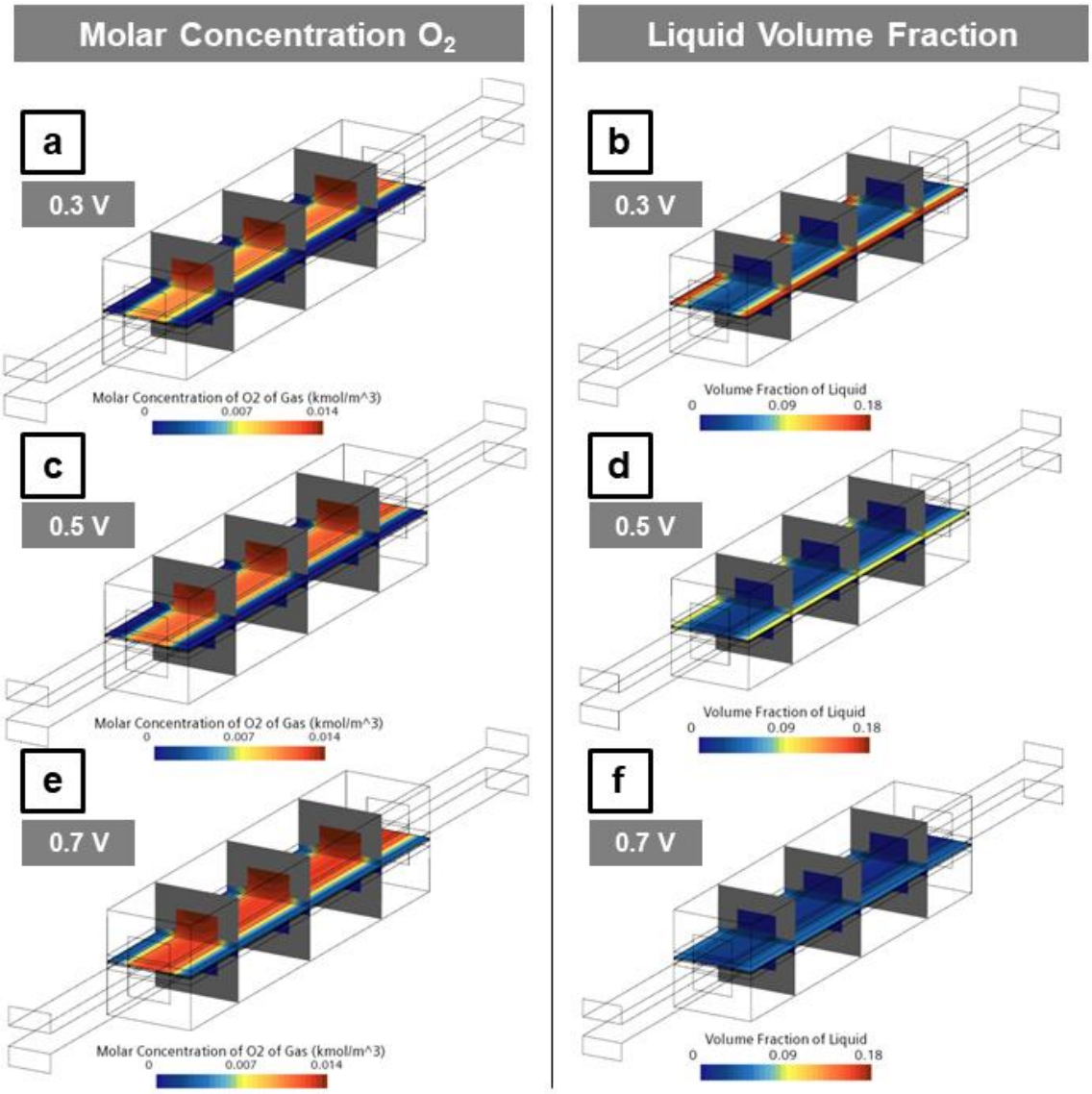

Figure 20 - Scalar fields for Case 1 with CR 0.66 for the molar concentration of O2 [kmol/m3] (left) and of volume fraction of liquid (right) at 0.3 V (a-b), at 0.5 V (c-d) and at 0.7 V (e-f).

In terms of ohmic losses, the compressed cases display higher values, which is initially counterintuitive given the enhanced electrical conductivity of the diffusive layers under the land zone. To further investigate this phenomenon, two novel indices were introduced: the Index of Uniform Membrane Water Content (IUλ), which quantifies the uniformity of the water content distribution, and a non-dimensional Membrane Performance Coefficient (C_m), which evaluates the combined effect of hydrated regions and ionic current (i_e). This coefficient is scaled by the limiting current density (i) and a maximum

water [1] content (λ*=22). These indices are computed using Equations (87) and (88), respectively.

The limiting current density is estimated using the correlation provided in (Equation (89)), where n represents the number of electrons, D is the diffusion coefficient of the reactant species (oxygen in this case), δ is the diffusion distance, and C_B is the bulk concentration of oxygen.

$$IU\lambda = \frac{\int_v |\lambda - \lambda_{avg}| dV}{\int_v dV} \quad \text{Eq. 87}$$

$$C_m = \frac{1}{i_L \lambda^*} \frac{\int_v i_e \lambda dV}{\int_v dV} \quad \text{Eq. 88}$$

$$i_L = \frac{nFDC_B}{\delta} \quad \text{Eq. 89}$$

An analysis of the average membrane water content λ_{avg} and average ionic conductivity (σ_{avg}^{eff}) for all cases in Table 6 reveals a non-monotonic trend when transitioning from CR = 1 to CR = 0.66 and CR = 0.5. This contrasts with the continuous increase in ohmic overpotential, primarily attributed to the membrane's resistance to ionic transport. However, examining the Index of Uniform Membrane Water Content (IUλ) shows a monotonic increase as the compression ratio decreases, indicating reduced uniformity of membrane hydration in more compressed states. This is further evidenced by the diverging maximum and minimum λ values, as illustrated in Figure 21.

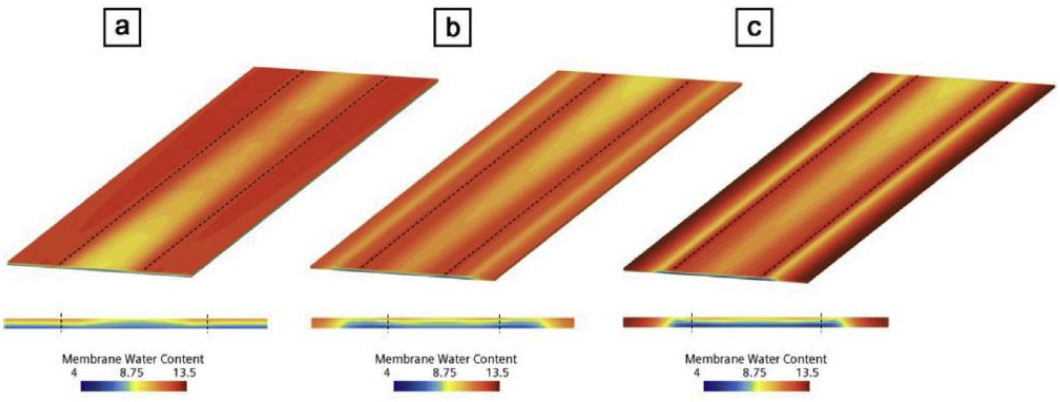

Figure 21 - Scalar fields of water content in membrane for Case 1 CR 1 (a), CR 0.66 (b) and CR 0.5 (c).

The decreased uniformity can be observed by comparing the liquid volume fraction fields for Case 1 at CR = 1 (*Figure 16, left*) and CR = 0.66 (*Figure 20, right*), where a clear reduction in uniformity is seen, caused by less efficient mass transport. To further understand the rise in ohmic overpotential, the Membrane Performance Coefficient (C_m) is examined. The values in *Table 9* confirm a monotonic decline in C_m with increasing compression, directly linking this reduction to the observed increase in ohmic overpotential.

Table 9 - Values of λ_{avg} (first row) ,σ_{avg}^{eff} (second row), λ_{max} (third row), σ_{max}^{eff} (fourth row), λ_{min} (fifth row), σ_{min}^{eff} (sixth row), $IU\lambda$ (seventh row) and C_m (eight row) for Case 1 with CR 1(left column), CR 0.66 (middle column) and CR 0.5 (right column).

Variable	**CR=1**	**CR=0.66**	**CR=0.5**
λ_{avg}	8.97	8.57	9.01
σ_{avg}^{eff}	7.89 $[S/m]$	7.49 $[S/m]$	7.91 $[S/m]$
λ_{max}	18.2	21.2	23.6
σ_{max}^{eff}	16.55 $[S/m]$	19.31 $[S/m]$	21.65 $[S/m]$
λ_{min}	5.90	4.55	4.00
σ_{min}^{eff}	4.95 $[S/m]$	3.67 $[S/m]$	3.16 $[S/m]$
$IU\lambda$	1.00	1.26	1.65
C_m	0.045	0.042	0.040

These findings underscore that analyzing membrane water content alone does not fully account for the variations in ohmic overpotential, as regions of high hydration can result from poor water removal, effectively creating conditions similar to flooding. Only by incorporating the local ionic current into the analysis using the C_m index can we differentiate beneficial hydration (current-conductive regions) from detrimental hydration (water-occluded or flooded areas). This combined approach provides new insights into distinguishing effective from ineffective membrane hydration.

4.8 Conclusions

In this chapter, we developed and validated a three-dimensional computational fluid dynamics (CFD) model of a proton exchange membrane fuel cell (PEMFC) operating with hydrogen and air. The model was validated against experimental data from two straight-channel configurations reported in [58], which were specifically chosen to emphasize the effects of varying channel-to-rib width ratios. By incorporating a computationally efficient macro-homogeneous approach for the volumetric catalyst layer (CL), the model demonstrated both accuracy and computational efficiency, highlighting its suitability for industrial-scale PEMFC simulations.

Key Findings

The first part of the study focused on validating the model's predictive capabilities. The simulated polarization curves and the accumulation of the liquid phase in the porous media, both in terms of average values and spatial distribution, showed good agreement with experimental measurements. This validation confirmed that the model reliably captures the key physical phenomena occurring within the cell.

We observed that increasing the channel-to-rib width ratio leads to higher concentration and ohmic overpotentials. Specifically:

- **Concentration Overpotential**: Larger rib areas resulted in more extensive oxygen-deficient regions under the land zones, impeding oxygen transport to the reaction sites.
- **Ohmic Overpotential**: A non-uniform membrane hydration state developed, leading to increased cell resistance.

Both factors contributed to a reduction in overall cell performance.

In the second part of the study, we incorporated the deformation of the porous materials—the gas diffusion layer (GDL) and the catalyst layer (CL)—caused by mechanical compression from the bipolar plates (BPP). This was achieved by extending the model

proposed in [82], resulting in modifications to porosity, tortuosity, permeability, and both electrical and thermal conductivities of the porous media.

The results indicated a significant reduction in cell performance, especially at high current densities. The compression of the porous media led to:

- **Increased Mass Transport Resistance**: Compression hindered the efficient delivery of reactants and removal of products within the porous media.
- **Impeded Liquid Water Removal**: Reduced porosity under the land zones made it more difficult to remove liquid water, increasing concentration overpotentials.
- **Non-uniform Membrane Hydration**: Inhomogeneous compression led to decreased ionic conductivity and increased ohmic overpotentials.

Implications for Fuel Cell Design

From these findings, several important conclusions can be drawn:

1. **Channel-to-Rib Width Ratio**: Optimizing this ratio is a critical design parameter for enhancing PEMFC performance. A reduced ratio improves reactant transport to active sites beneath the land zones and promotes more uniform membrane hydration, thereby lowering cell electrical resistance.
2. **Porous Media Deformation**: Accounting for the inhomogeneous compression of the diffusive layers is essential for accurate modelling under practical operating conditions. The deformation significantly impacts cell performance at high current densities by altering local material properties and increasing both ohmic and concentration overpotentials.

5 PEM Fuel Cell

In this chapter, the results of the numerical simulation for the entire PEM fuel cell are presented. The modelling approach employed here closely parallels that of the single-channel study discussed in the previous chapter; therefore, the detailed methodology will not be reiterated. However, unlike the first study, the deformation of the porous media is ignored. The focus shifts to examining the effect of thermal management on fuel cell performance by analysing four different cooling circuits in order to investigate the importance of optimal thermal management which plays a critical role in the operation and performance of Polymer Electrolyte Membrane Fuel Cells (PEMFCs), significantly more so than in internal combustion engines (ICEs). This difference arises primarily from the distinct operating temperature ranges and thermal sensitivities of these two technologies.

In ICEs, the operating temperature range is relatively wide, due to the combustion process. These systems inherently tolerate significant thermal fluctuations without drastic impacts on performance. Cooling systems in ICEs primarily aim to prevent overheating of the engine components rather than to maintain a narrowly defined optimal temperature range. Consequently, thermal management in ICEs, while necessary, is less critical for fine-tuning performance.

In contrast, PEMFCs operate at much lower temperatures, typically below 100 °C, making them highly sensitive to thermal variations. Precise control of the operating temperature is essential for several reasons:

1. **Membrane Hydration**: The polymer electrolyte membrane's conductivity relies heavily on adequate hydration, which is directly influenced by the cell temperature. Excessive heat can lead to membrane dehydration, reducing proton conductivity and overall cell efficiency. Conversely, inadequate heat dissipation may result in excessive water condensation, hindering gas transport and reactant distribution.

2. **Reaction Kinetics**: The rate of the electrochemical reactions occurring at the electrodes depends on temperature. While higher temperatures generally enhance

reaction kinetics, the upper limit is constrained by the material properties of the membrane and other components.

3. **Durability**: Thermal stress and gradients within the fuel cell can lead to mechanical degradation of the membrane and other components over time. Effective thermal management minimizes these stresses, prolonging the device's operational lifespan.

4. **System Efficiency**: Precise thermal regulation ensures that the energy produced by the fuel cell is not wasted in managing extreme temperature conditions. This contributes to improved overall efficiency, especially in systems designed for continuous operation.

In light of these factors, thermal management in PEMFCs is not merely a support function but a core component of their design and operation. Achieving optimal thermal conditions within a narrow temperature range directly impacts the performance, efficiency, and longevity of the fuel cell. This makes thermal management a cornerstone of research and development efforts aimed at improving PEMFC systems for real-world applications.

5.1 Computational Model

Four full-cell 3D models were developed using SIMCENTER STAR-CCM+ 2021.2, licensed by SIEMENS DISW. Each model consists of 2,240,200 finite volume cells and incorporates the polymeric membrane, two catalyst layers, two gas diffusion layers, two reactant channel systems, and two bipolar plates. Additionally, it includes two cooling channel systems embedded within the bipolar plates on both the anode and cathode sides.

The four models differ in the configurations used for the cooling system, typically analyzed in literature [87] [88] and illustrated in Figure 22, which also depicts the computational domain of the cell. The dimensions of each component are provided in *Table 10*. Three different coolant mass flow inlet values are tested for each cooling circuit: $\dot{m}_{cool}$ = 1E-4 kg/s, $\dot{m}_{cool}$ = 3E-4 kg/s and $\dot{m}_{cool}$ = 6E-4 kg/s. It is important to note that

these mass flow rates are maintained constant across all simulated voltages, and the external surfaces of the computational domain are assumed to be adiabatic. Pure water is employed as the coolant in the analysis.

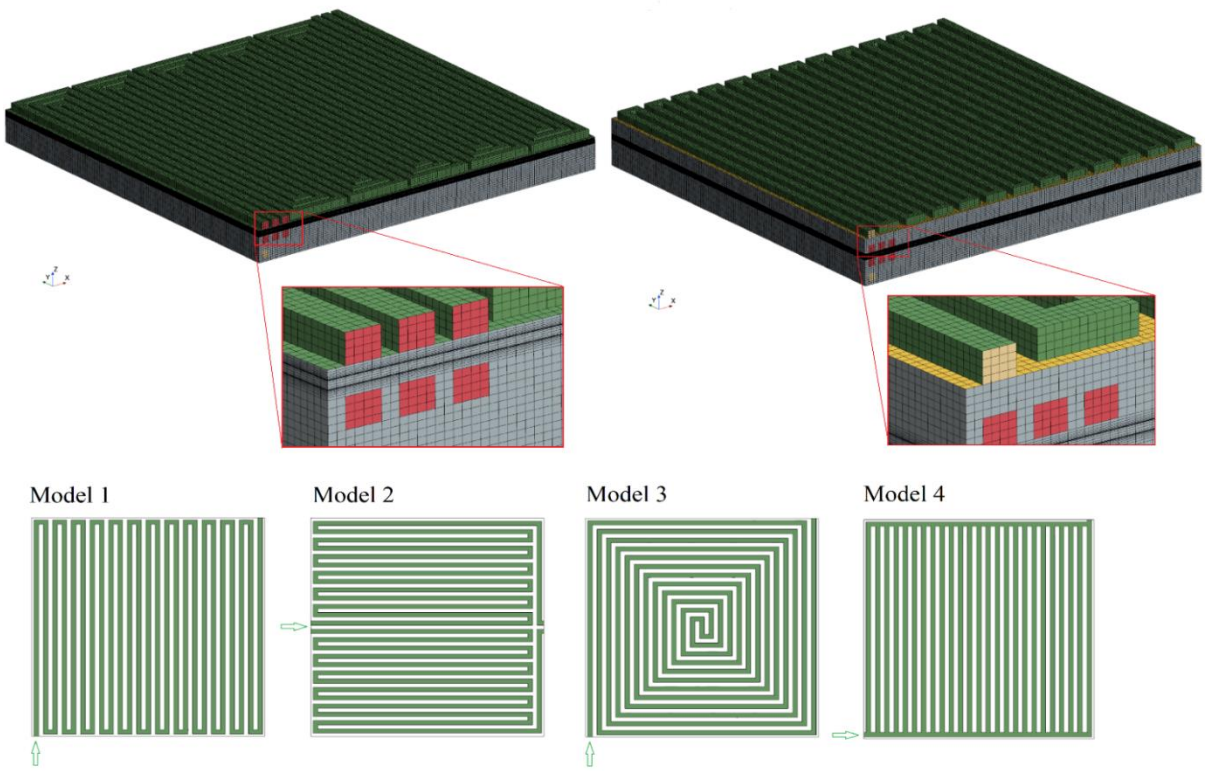

Figure 22 - Computation domain and mesh. Cooling circuit configurations Model 1), Model 2), Model 3) and Model 4).

Table 10 - Geometrical dimensions

Property	**Value**
Channel height	1 mm
Channel width	1 mm
BP width between channels	0.5 mm
BP height	1.5 mm
GDL thickness	300 µm
CL thickness	12 µm
Membrane thickness	30 µm

Table 11 - Physical properties of Fuel Cell's main components.

Property	Value
GDL	
El. Conductivity	5000 S/m
Th. Conductivity	24 W/m/K
Porosity ε_{GDL}	0.7
CL	
Ionomer Vol. F	0.2
Pt/C Vol. F	0.8
Porosity ε_{CL}	0.5
$j_{0,c}^{ref}$	0.043 A/m^2
$j_{0,a}^{ref}$	5200 A/m^2
γ_c	0.5
γ_a	1
(Ionomer phase of CL)	
Density	2000 kg/m^3
Ion. Conductivity	Eq.
Spec. Heat	903 J/kgK
Th. Conductivity	0.445 W/mK
(Pt/C phase of CL)	
Density	2000 kg/m^3
El. Conductivity	5000 S/m
Spec. Heat	708 J/kgK
Th. Conductivity	24 W/mK
Bipolar Plate	
Density	2250 kg/m^3
El. Conductivity	125000 S/m
Spec. Heat	708 J/kgK
Th. Conductivity	24 W/mK
Membrane	
Density	2000 kg/m^3
Ion. Conductivity	Eq. 72
Spec. Heat	903 J/kgK
Th. Conductivity	0.445 W/mK

Table 12- Boundary conditions.

Property	**Value**
Anode Channel H_2 H_2O	
Relative Humidity	100%
Temperature	353K (80 °C)
Absolute Pressure	250 kPa
Cathode Channel O_2 N_2 H_2O	
Relative Humidity	100%
Temperature	353 K (80 °C)
Absolute Pressure	250 kPa
Gas Diffusion Layer & Catalyst Layer	
Temperature	353K (80 °C)
Absolute Pressure	250 kPa
Cooling Channel H_2O Liquid	
Temperature	353K (80 °C)
Absolute Pressure	200 kPa

5.2 Results

Figure 23 and Figure 24 display the polarization curves and power outputs for all models analyzed at various coolant mass flow rates. It becomes immediately apparent that an increase in coolant flow rate results in higher current densities across all configurations. To facilitate a clearer comparison, the lower part of the figure illustrates the curves of the different models for all inlet coolant flow rates.

The results show that Model 1 consistently achieves the highest current density values in every case, while Model 3 records the lowest values at the two lowest flow rates. Models 2 and 4 exhibit opposite trends as the coolant flow rate increases. Specifically, Model 2 enhances its performance, reaching current density values similar to those of Model 1 at the highest flow rate. In contrast, Model 4 shows only a slight improvement and registers the lowest current density at the highest flow rate.

These findings can be explained by examining the membrane temperature values presented in Figure 25. Model 1 maintains the lowest average temperature, which leads to the highest water content in the membrane (Figure 26) and consequently results in

maximum ionic conductivity (Figure 27). Observing Models 2 and 4, we notice that Model 2 experiences a significant and rapid temperature reduction as the coolant flow rate increases, while Model 4 shows a modest decrease. These variations in membrane temperature impact the membrane's water content and ionic conductivity, corroborating the trends observed in the polarization curves.

Figure 28 illustrates the thermal power density absorbed by the cooling circuits on both the anode and cathode sides across all simulated voltages and coolant flow rates. The trends align with the previously discussed membrane temperature variations among the different models. Additionally, an increase in heat flux is observed as the voltage decreases, corresponding to a rise in the thermal power generated by the cell.

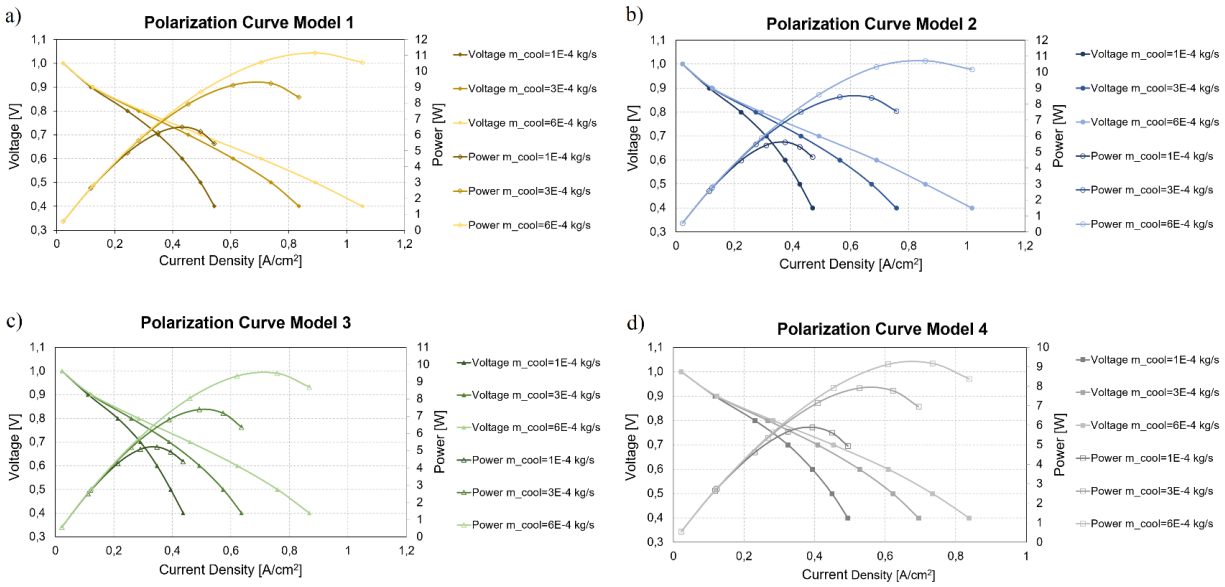

Figure 23 - Comparison of polarization curves and power for $\dot{m}_{cool} = 1E-4\ kg/s$, $\dot{m}_{cool} = 3E-4\ kg/s$ and $\dot{m}_{cool} = 6E-4\ kg/s$ in: a) Model 1, b) Model 2, c) Model 3, d) Model 4

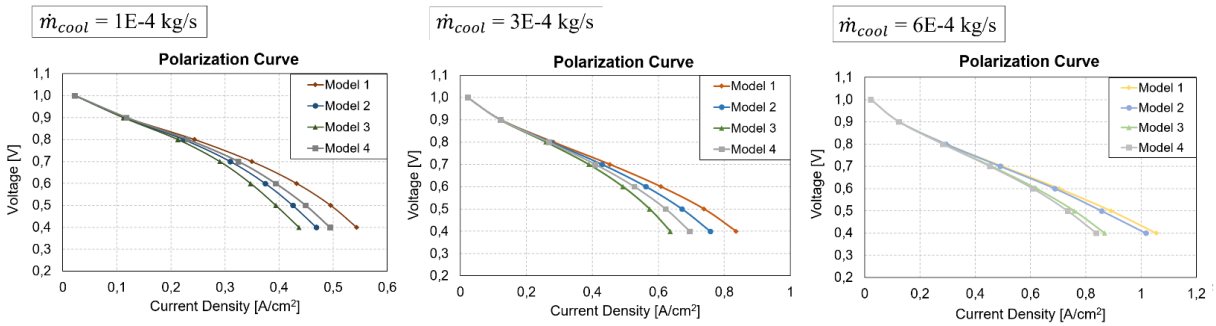

Figure 24 - Comparison of polarization curves for all models at the same coolant mass flow rates.

Although the cell performance results are significant, it is necessary to consider additional criteria for selecting the optimal cooling circuit. One such criterion is the Uniform Index of Temperature (IUT), defined as:

$$IUT = \frac{\int_v |T - T_{avg}|\, dV}{\int_v dV} \qquad \text{Eq. 90}$$

A lower IUT value indicates a more uniform temperature distribution within the cell. However, this parameter alone is insufficient for a comprehensive evaluation of the cooling circuit. Therefore, we also consider the temperature difference $\Delta T = T_{max} - T_{min}$ within the region of interest and the pressure drop ΔP across the cooling circuit, which determines the energy required to pump the coolant through the cell.

The IUT calculated for the membrane is presented in Figure 30 for all voltages and coolant flow rates analyzed. The temperature difference ΔT and the pressure drop ΔP are shown in Figure 29 and Figure 31, respectively.

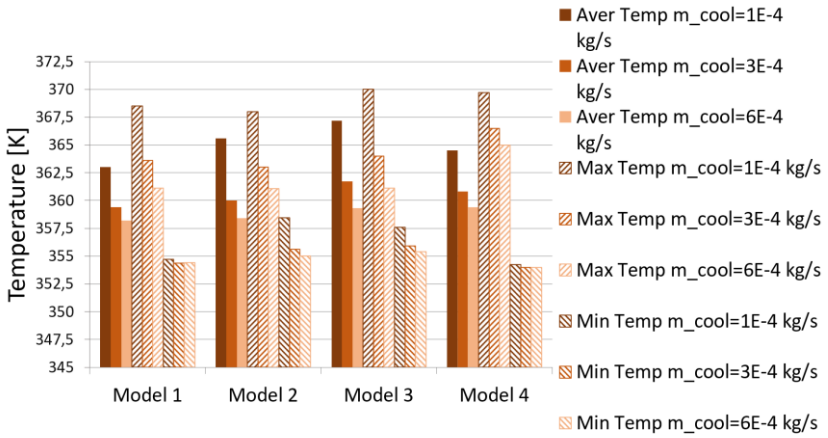

Figure 25 - Average, maximum and minimum membrane temperature at 0.4V for all coolant mass flow rates.

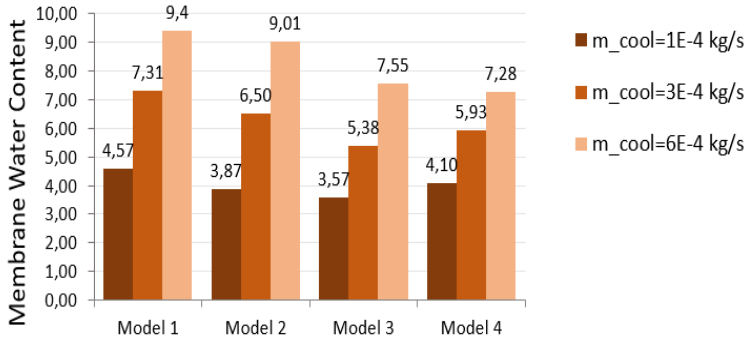

Figure 26 - Membrane water content at 0.4V for each model and coolant mass flow rates.

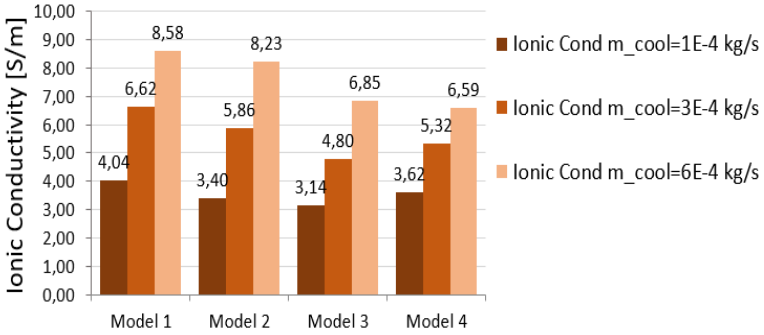

Figure 27 - Membrane ionic conductivity at 0.4V for each model and coolant mass flow rates.

Examining Figure 29 and Figure 30 for the case at 0.4 V, it is observed that Model 3 exhibits the lowest values of the Uniform Index of Temperature (IUT) and the temperature difference ΔT at the two highest coolant mass flow rates, as shown below.

Model 3			
$\dot{m}_{cool}$ [kg/s]	$1E-4$	$3E-4$	$6E-4$
$\dot{V}_{cool}$ [l/min]	0.006	0.018	0.036
IUT	1.5	1.22	0.76
ΔT [K]	12.4	8.1	5.7

Conversely, Model 4 displays the highest IUT and ΔT values at the two highest flow rates, with a slightly decreasing trend as the flow rate increases.

Model 4			
$\dot{m}_{cool}$ [kg/s]	$1E-4$	$3E-4$	$6E-4$
$\dot{V}_{cool}$ [l/min]	0.006	0.018	0.036
IUT	2.83	2.5	2.15
ΔT [K]	15.5	12.5	11

Model 1, despite demonstrating the best performance in terms of current density, shows relatively high IUT and ΔT values. However, there is a significant decreasing trend in these values as the coolant flow rate increases.

Model 1			
$\dot{m}_{cool}$ [kg/s]	$1E-4$	$3E-4$	$6E-4$
$\dot{V}_{cool}$ [l/min]	0.006	0.018	0.036
IUT	3.57	2.02	1.3
ΔT [K]	13.8	9.2	6.7

Lastly, Model 2 presents favorable values with a mildly decreasing trend.

Model 2			
$\dot{m}_{cool}$ [kg/s]	$1E-4$	$3E-4$	$6E-4$

$\dot{V}_{cool}$ [l/min]	0.006	0.018	0.036
IUT	1.44	1.38	1.07
ΔT [K]	9.6	7.4	6.1

Referring to Figure 31, it becomes evident that Model 3 has the highest pressure drop across the cooling circuit, whereas Model 4 exhibits the lowest pressure drop due to the lower fluid velocities within the cooling channels, as shown in Figure 32, compared to the other models. Model 1 shows a relatively high pressure drop, which is well compensated by the increased power output from the cell. Finally, Model 2 offers a good compromise between pressure drop and power output.

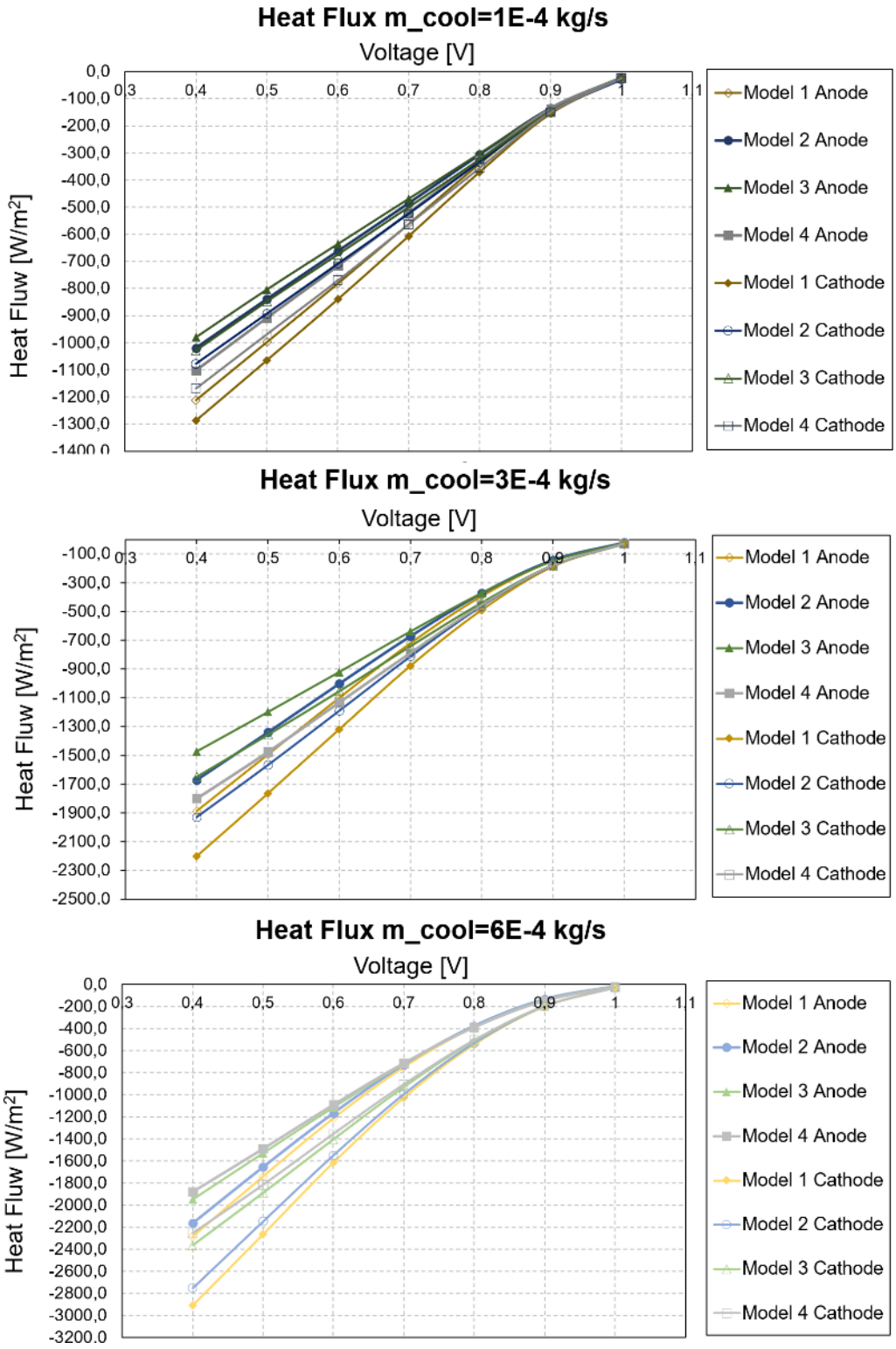

Figure 28 - Heat flux [W/m2] for all models and voltages with $\dot{m}_{cool} = 1E-4\ kg/s$, $\dot{m}_{cool} = 3E-4\ kg/s$ and $\dot{m}_{cool} = 6E-4\ kg/s$

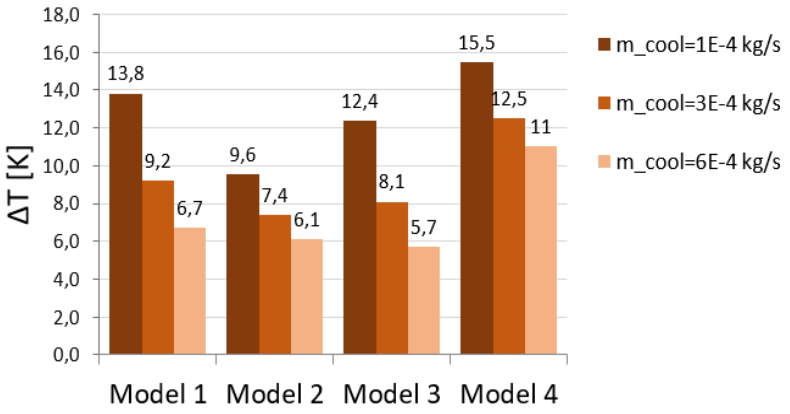

Figure 29 - ΔT [K] at 0.4V for each model and coolant mass flow rates.

Figure 33, Figure 34 and Figure 35 depict the temperature distribution on the MEM/CLc interface at 0.4 V for all the analyzed coolant flow rates, enabling visualization of the previously discussed IUT parameter and ΔT. In Model 1, a significant temperature non-uniformity is evident at $\dot{m}_{cool} = 1E-4\ kg/s$, a phenomenon that rapidly diminishes as the coolant flow rate increases. This configuration results in a unidirectional temperature gradient from the sidewall near the inlet to the outlet.

Model 4 exhibits pronounced temperature unevenness and asymmetry in the temperature field even at higher flow rates, where other configurations tend to achieve a more uniform distribution. The maximum temperature is located laterally toward the outlet section.

Model 3 provides the most homogeneous temperature distribution at coolant flow rates of $\dot{m}_{cool} = 3E-4\ kg/s$ and $\dot{m}_{cool} = 6E-4\ kg/s$, thus ensuring favorable operating conditions for the membrane. This advantage comes at the expense of a high pressure drop across the cooling circuit and higher average operating temperatures compared to other configurations. The maximum temperature in this model is situated at the center of the cell.

Finally, analyzing Model 2 reveals excellent temperature uniformity and reduced ΔT at $\dot{m}_{cool} = 1E-4\ kg/s$, but with diminishing improvements as the coolant flow rate increases. It is noteworthy that this configuration ensures good power output and low pressure drops.

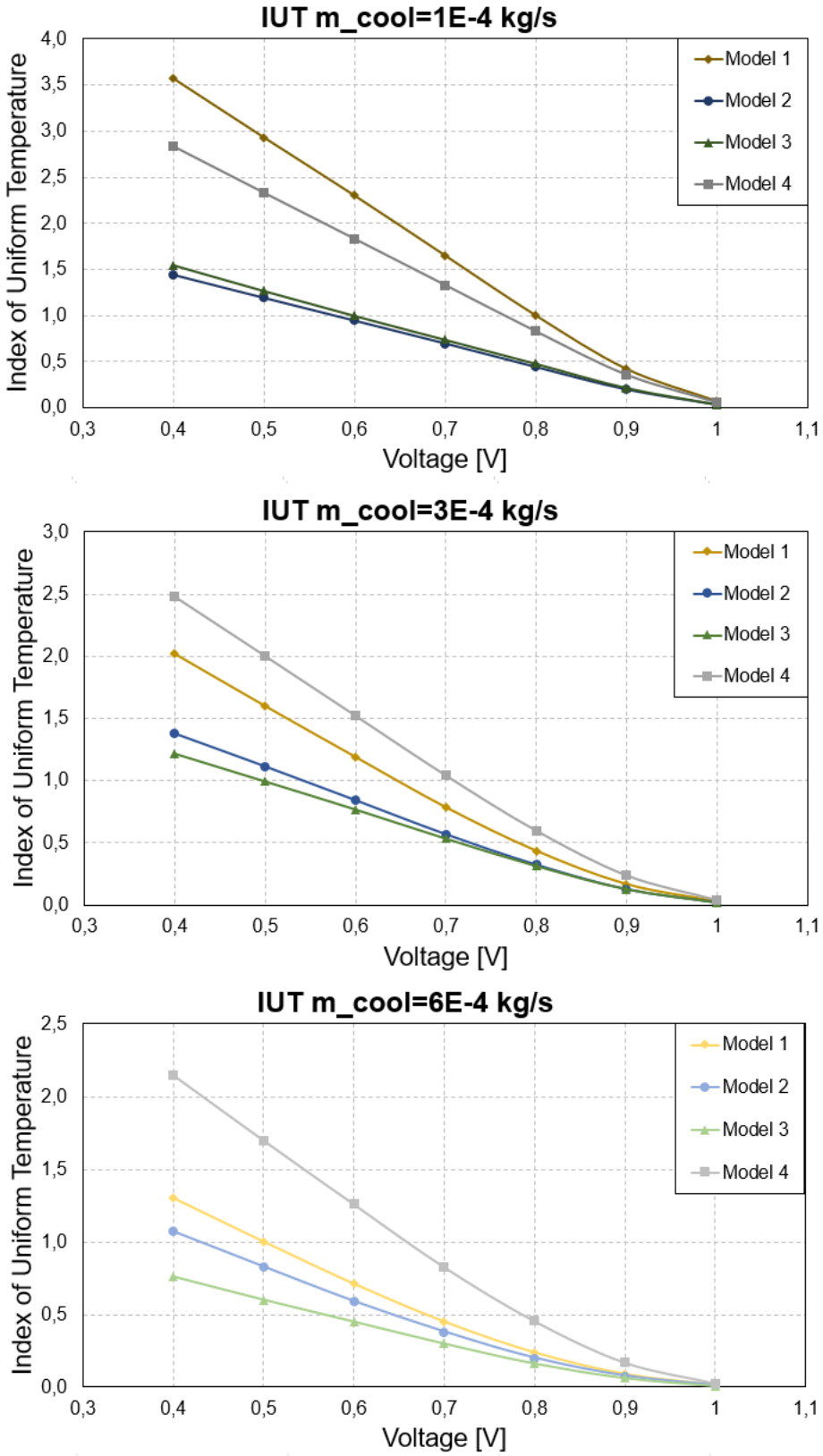

Figure 30 - Index of Uniform Temperature (IUT) in Membrane for all models and coolant mass flow rates.

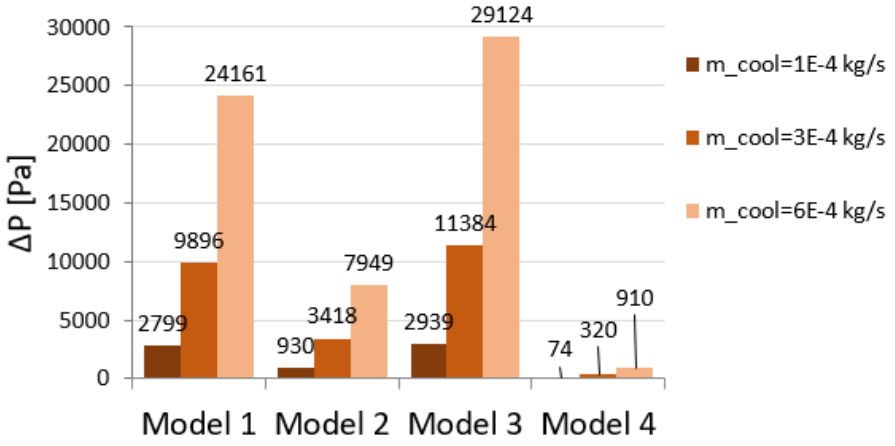

Figure 31 - ΔP[Pa] for each model and coolant mass flow rates

.

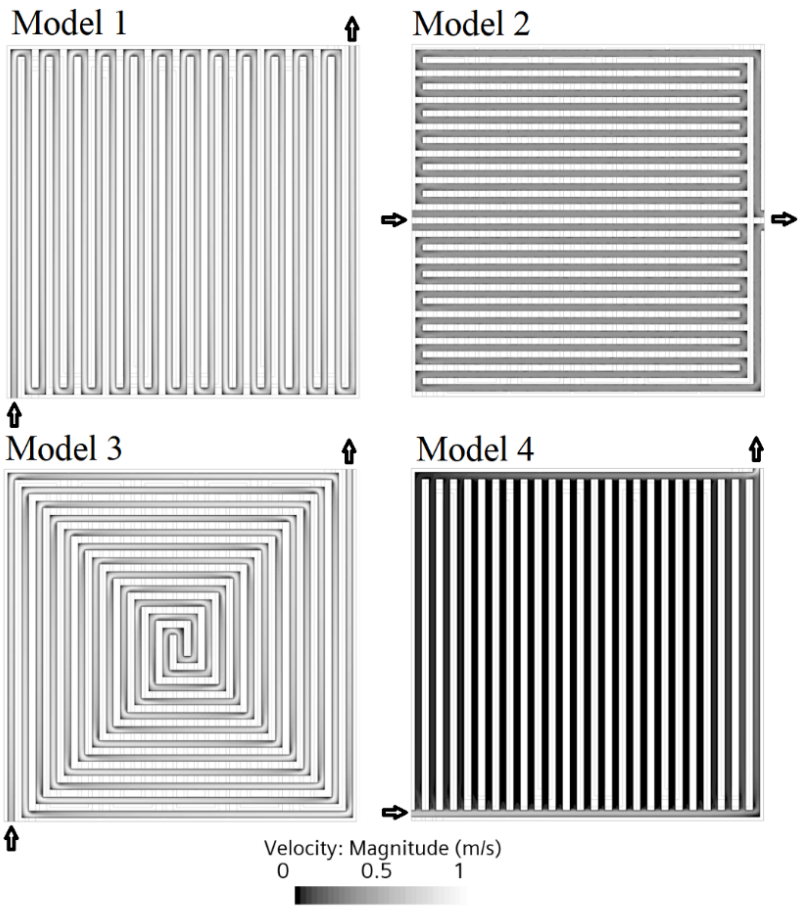

Figure 32 - Velocity magnitude in middle of cooling channel for $\dot{m}_{cool} = 6E-4\ kg/s$ (0.036 l/min).

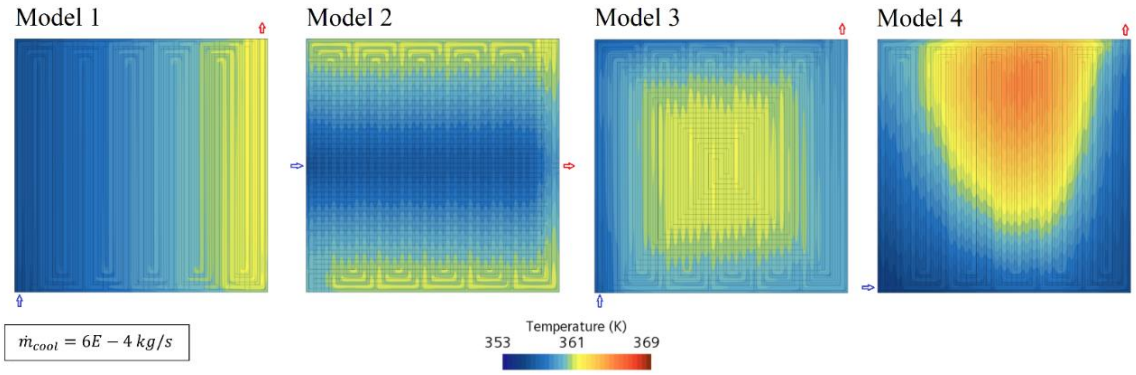

Figure 33 - Temperature distribution in MEM/CLc at 0.4V for all model at $\dot{m}_{cool} = 6E-4\ kg/s$ *(0.036 l/min).*

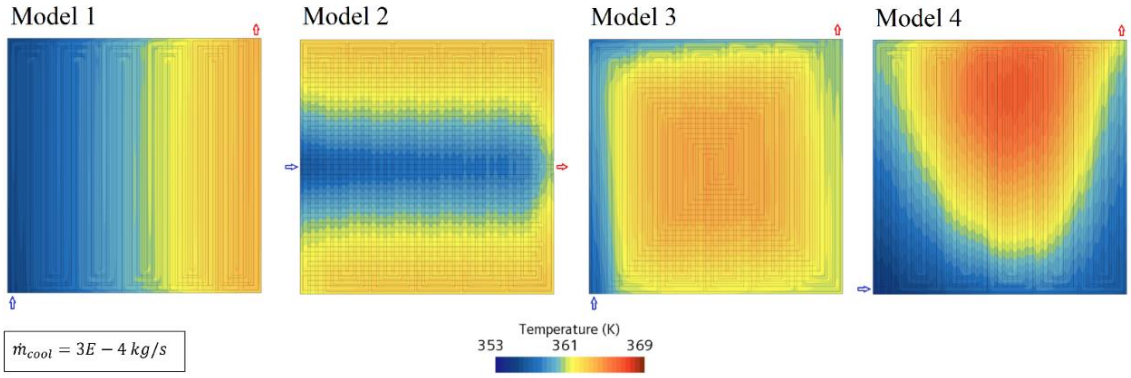

Figure 34 - Temperature distribution in MEM/CLc at 0.4V for all model at $\dot{m}_{cool} = 3E-4\ kg/s$ *(0.018 l/min).*

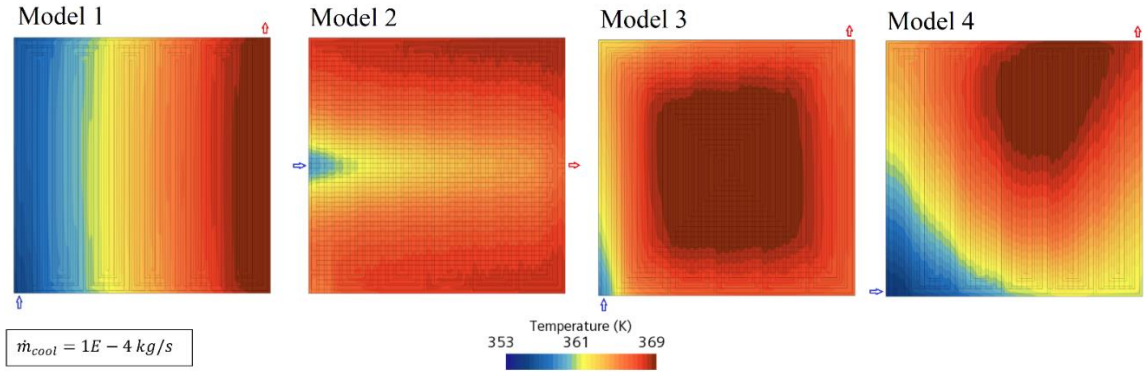

Figure 35 - Temperature distribution in MEM/CLc at 0.4V for all model at $\dot{m}_{cool} = 1E-4\ kg/s$ *(0.006 l/min).*

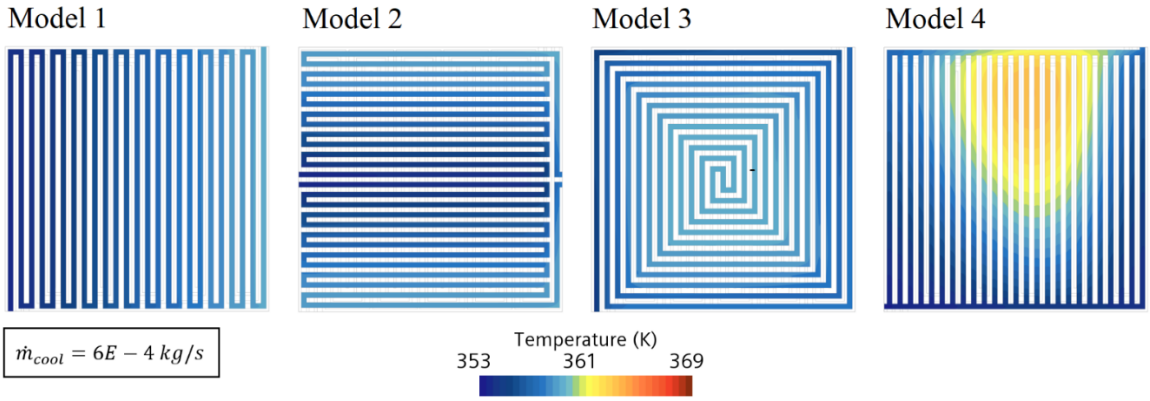

Figure 36 - Temperature distribution in middle of cathode-side cooling channels for all models at 0.4V at $\dot{m}_{cool} = 6E-4\ kg/s$ (0.036 l/min)

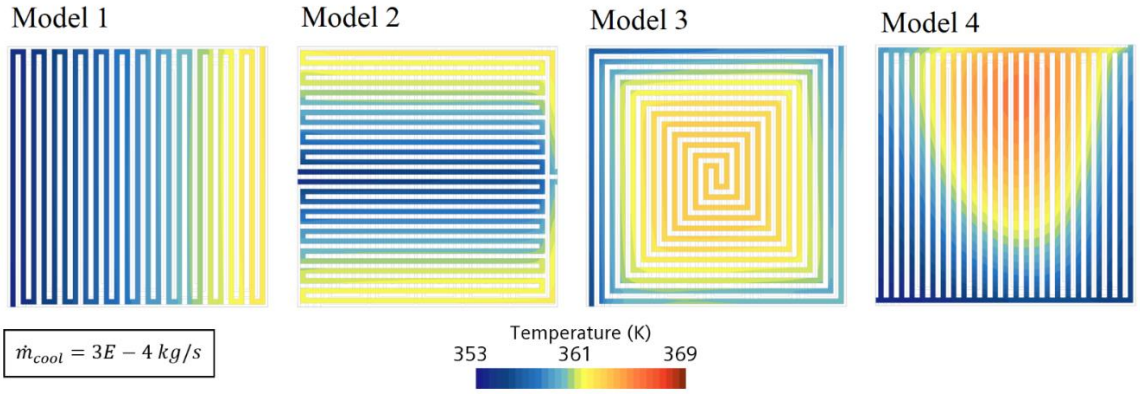

Figure 37 - Temperature distribution in middle of cathode-side cooling channels for all models at 0.4V at $\dot{m}_{cool} = 3E-4\ kg/s$ (0.018 l/min)

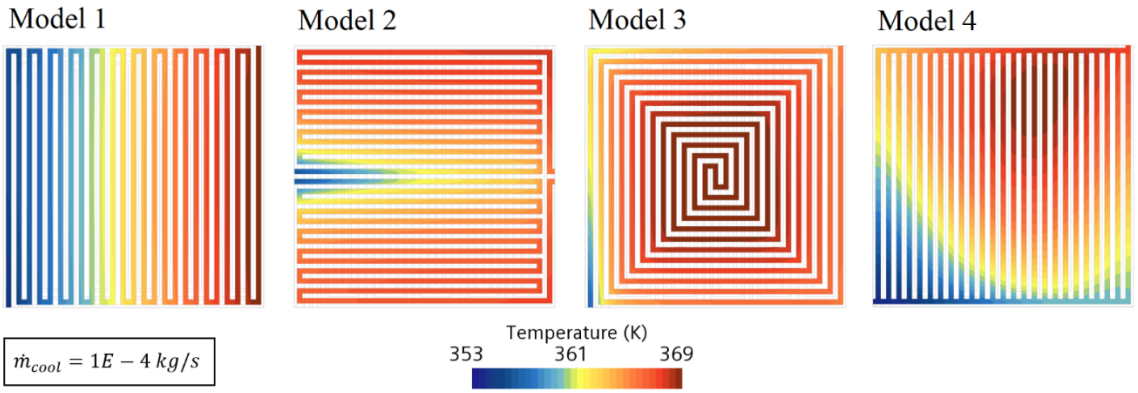

Figure 38 - Temperature distribution in middle of cathode-side cooling channels for all models at 0.4V at $\dot{m}_{cool} = 1E-4\ kg/s$ (0.006 l/min)

Figure 36, Figure 37 and Figure 38 illustrate the temperature distribution at the midpoint of the cathode-side cooling channels. In Figure 39, the maximum temperature values are observed for Model 1, aligning with the heat flow data presented. This configuration enables the maximum heat removal from the cell, whereas Model 4 allows for the minimum.

Ohmic Overpotential

Ohmic losses, resulting from resistance to the flow of ions in the electrolyte and electrons through electrically conductive components, are described by Ohm's Law:

$$DV_{ohm} = i\,R_i \qquad \text{Eq. 91}$$

where R_i [Ω·cm²] is the total internal resistance of the cell—comprising ionic, electrical, and contact resistances — and i is the current density [A/cm²]. Figure 41 presents the analysis of ohmic losses alongside the current density for each case studied. In this investigation, electrical contact resistances between components were neglected; therefore, the ohmic voltage drops are attributed solely to the electrical and ionic resistances.

A decreasing trend in ohmic overpotential is observed across all models as the coolant flow rate increases. This phenomenon is due to improved thermal management of the membrane, which enhances hydration and reduces ionic resistance. Model 1 exhibits the lowest ohmic losses because of its highest heat absorption capacity. For completeness, Figure 40 displays the total internal resistance of the cell, which in this context is predominantly determined by the ionic resistance of the membrane. Again, a decreasing trend is evident across all cases, with Model 1 showing the lowest resistance values.

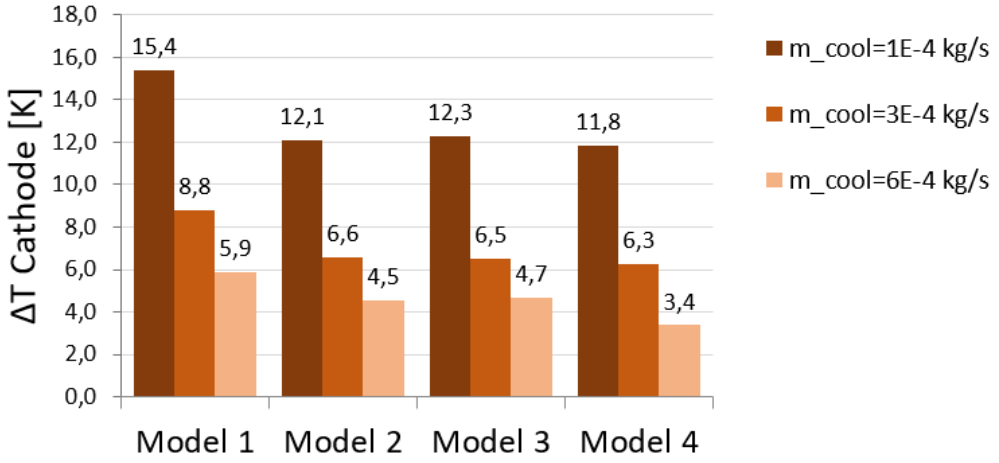

Figure 39 - ΔT [K] between outlet and inlet of the cooling circuit on the cathode side at 0.4V for all coolant mass flow rates.

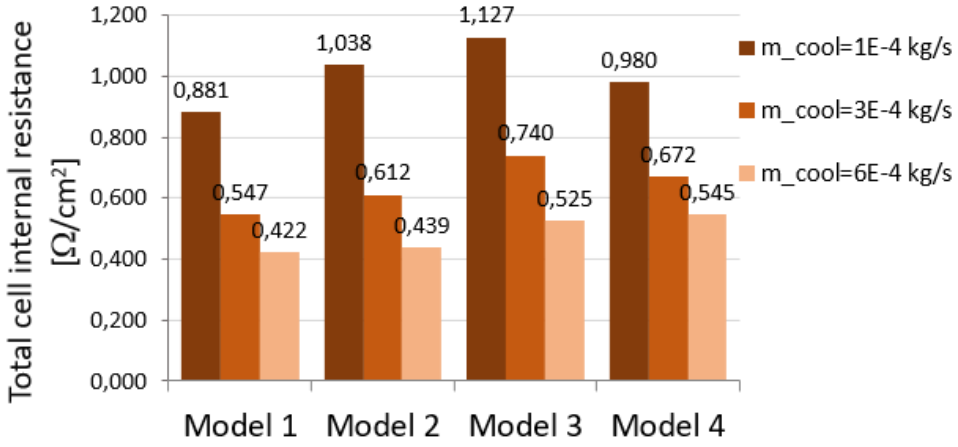

Figure 40 - Total cell internal resistance [Ω/cm2] at 0.4V for all coolant mass flow rates.

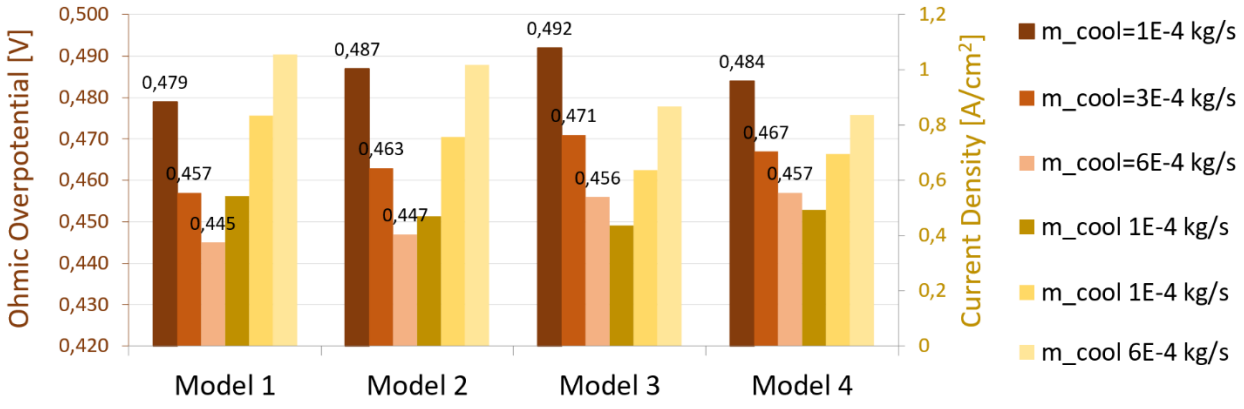

Figure 41 - Ohmic overpotential [V] (brown) and Current density [A/cm2] (black) at 0.4V for each model and coolant mass flow rates.

5.3 Conclusions

In this work, a numerical comparison was performed among four different cooling circuit configurations for PEM fuel cells, varying the coolant mass flow rate to analyze their behavior under different operating conditions. The key findings are summarized below:

1. Model 1:
    - Electrical Performance: Achieved the highest current density and power output across all coolant flow rates and voltages analyzed.
    - Thermal Flux: The superior performance is attributed to the high thermal flux of this configuration, which maintains low operating temperatures in the membrane and enhances ionic conductivity.
    - Temperature Distribution: Showed a rapid improvement in temperature uniformity as the coolant flow rate increased, with the maximum temperature located near the outlet wall.
    - Ohmic Losses: Reported the lowest ohmic overpotential and total internal resistance, aligning with its high current density values.
    - Pressure Drop: Experienced a relatively high pressure drop across the cooling circuit, which is offset by the increased power output.

2. Model 2:
    - Balanced Performance: Offered a good compromise between thermal management and electrical performance.
    - Temperature Distribution: Demonstrated a favorable temperature profile with the maximum temperature near the side surfaces, facilitating easier heat removal if additional cooling methods are implemented.

- Ohmic Losses: Showed good values of ohmic overpotential and internal resistance, making it a promising candidate for practical applications.
- Pressure Drop: Had low pressure drops, contributing to overall operational efficiency.

3. Model 3:
   - Thermal Management: Exhibited the best thermal uniformity, with the lowest Uniform Index of Temperature (IUT = 0.76) and temperature difference (ΔT = 5.7 K) at a coolant mass flow rate of $\dot{m}_{cool} = 6E-4\ kg/s$.
   - Electrical Performance: Despite excellent thermal management, it showed lower current densities and higher pressure drops across the cooling circuit.
   - Temperature Distribution: The maximum temperature was located at the center of the cell, complicating heat dissipation through external surfaces.
4. Model 4:
   - Poor Performance: Displayed the worst temperature distribution and overall performance among the configurations studied.
   - Temperature Uniformity: Showed significant temperature unevenness even at higher coolant flow rates, with the maximum temperature located toward the outlet section.

This study underscores the importance of considering multiple performance criteria — including current density, thermal management, ohmic losses, and pressure drops — when selecting the optimal cooling circuit configuration for PEM fuel cells.

6 PEM Electrolysis Cell

The modeling approach described in the previous chapter, particularly the Mixture Multiphase Model combined with a macro-homogeneous treatment of the catalyst layer, can be effectively extended to the analysis of PEM electrolyzers. Despite the distinct operational modes of fuel cells and electrolyzers, both systems share analogous physical phenomena. In PEM electrolyzers, water is decomposed into hydrogen and oxygen gases, giving rise to multiphase flow dynamics comparable to those observed in fuel cells, where gaseous reactants are consumed. Furthermore, both devices involve similar thermal and electrical conduction processes due to their electrochemical reactions and share common structural components such as the membrane electrode assembly (MEA) and bipolar plates (BPs).

By adapting the catalyst layer modeling approach—specifically, modifying the definitions and kinetics of the electrochemical reactions—the same framework can be utilized to simulate the complex interplay of mass transport, heat transfer, and reaction kinetics in PEM electrolyzers.

6.1 Computational Model

The 3D model of a PEM Electrolysis Cell (PEMEC) featuring a three-channel serpentine design, as proposed by Ma et al. in [89], has been reproduced using SIMCENTER STAR-CCM+ v2022.2 (SIEMENS DISW). The geometry and dimensions of the model are depicted in Figure 42 and detailed in *Table 13*. The finite volume mesh is composed of approximately 1.35 million hexahedral cells, with 120,000 cells allocated to each catalyst layer (CL). Material properties and boundary conditions are outlined in *Tables 14 and 15*, respectively. The outer walls of the bipolar plates are treated as equipotential surfaces, with the cathode and anode potential values set to $\varphi_s = 0 / \Delta V$, respectively. The applied voltage, ΔV, varies within the range of 1.4 to 2.0 V, with a step increment of 0.1 V, and a refined increment of 0.05 V for low-voltage operation. The temperature of the outer bipolar plate walls is set to match the water inlet temperature (i.e., 333 K and 353 K for the two tested cases), under the assumption of an ideal cooling system. This assumption

stems from the fact that perfect thermal management in the upper and lower cells is considered in the stack assembly.

Table 13 - Geometrical dimensions, reproduced from [89].

Component dimensions	**Value**
Channel height	1 mm
Channel width	1 mm
BP width between channels	0.5 mm
BP height	1.5 mm
GDL thickness	300 μm
CL thickness	12 μm
Membrane thickness	30 μm

Table 14 - Physical and transport properties, reproduced from [89]

Property	**Value**
GDL	
Density (solid phase)	2250 kg/m^3
Electrical Conductivity	500 S/m
Thermal Conductivity	24 W/m/K
Permeability	4×10^{-12} m^2
Contact angle θ_c	110°
Porosity ε_{GDL}	0.7
CL	
Porosity ε_{CL}	0.4
Permeability	4×10^{-13} m^2
Contact angle θ_c	110°
Specific active area ζ	$110'000\ 1/m$
Ionomer Density	2000 kg/m^3
Ion. Conductivity	Eq. 12
Spec. Heat	903.0 J/kg/K
Th. Conductivity	0.445 W/m/K
Volume Fraction	0.4
Pt/C Density	2250.0 kg/m^3
El. Conductivity	500.0 S/m
Spec. Heat	707.68 J/kg/K
Th. Conductivity	10 W/m/K
Volume Fraction	0.6
BP	
Density	2250 kg/m^3
El. Conductivity	20000 S/m

Spec. Heat	707.68 J/kg/K
Th. Conductivity	20 W/m/K
Membrane	
Density	2000 kg/m^3
Ion. Conductivity	Eq. 12
Spec. Heat	903 J/kg/K
Th. Conductivity	0.445 W/m/K

Table 15 - Boundary conditions, reproduced from [89].

Boundary Conditions		**Value**
Cathode Channel		
	Inlet	
	Water flowrate	5 ml/min (hydration)
	Temperature	353 K / 333 K
	Volume fraction of water	1
	Outlet	
	Pressure	101325 Pa
Anode Channel		
	Inlet	
	Water flowrate	50 ml/min
	Temperature	353 K / 333 K
	Volume fraction of water	1
	Outlet	
	Pressure	101325 Pa
Cathode BP		
	Top	
	Electric Potential	0 V
	Temperature	353 K / 333 K (Fixed by the cooling system)
	Bottom	
	Electric Potential	From 1.4V to 2.0V
	Temperature	353 K / 333 K (Fixed by the cooling system)

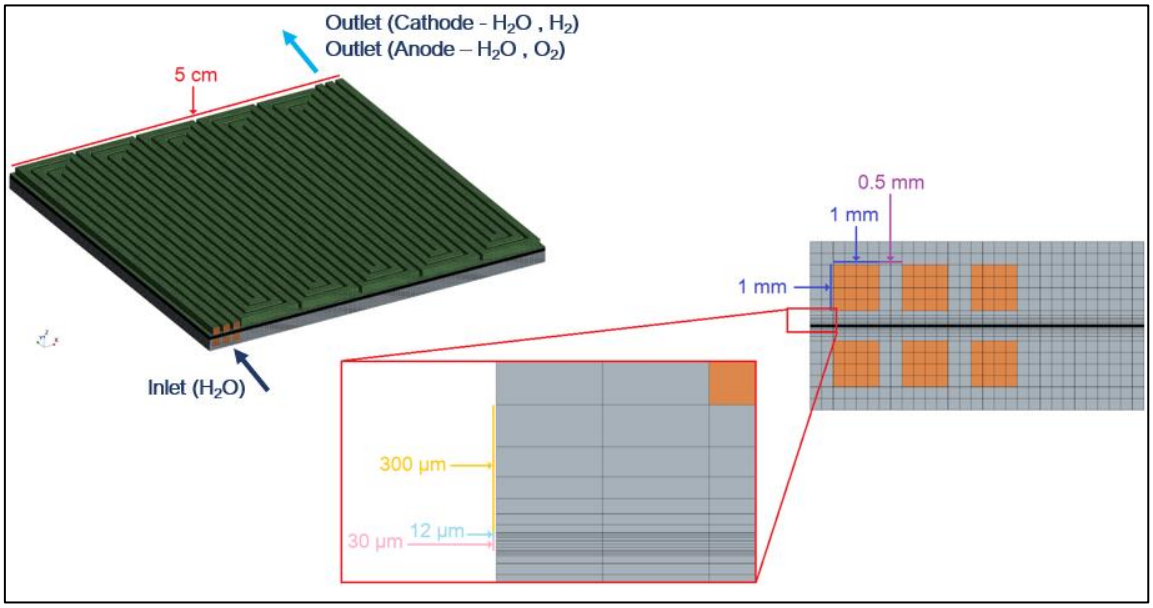

Figure 42 - Computational domain with main dimensions and finite volume mesh.

6.2 Results

The numerical model was validated by comparing the simulated polarization curves with the experimental data reported in [89] at two temperature levels. As illustrated in Figure 43, the simulation results closely match the experimental data, demonstrating good agreement in current-voltage characteristics for both operating temperatures. The simulations accurately replicate the experimentally observed voltage reduction with increasing temperature, indicating that the model effectively captures the physics-based contributions of overpotentials.

To gain deeper insight into the cell's performance, individual overpotential analyses were conducted for each applied voltage, as shown in Figure 44. The anodic activation overpotential emerged as the largest contributor, primarily due to the low exchange current density at the anode. Conversely, the concentration overpotential is minimal—negligible below 1.6 V and only becoming significant around 2.0 V. This behavior is attributed to the gradual accumulation of gaseous oxygen in the anodic catalyst layer (CL), which impedes reactant transport because of its high specific volume and the obstructive nature of the porous CL and gas diffusion layers (GDLs).

Figure 45 displays the gas volume fraction at the interface between the GDL and the anode-side channels. The presence of horizontal bands with reduced gas volume fraction near the serpentine bends is due to liquid water infiltrating the GDL. This infiltration displaces the gas, ejecting it into adjacent channels where higher gas volume fractions are observed. This phenomenon is driven by the pressure gradient between adjacent channel pairs, causing the liquid to bypass the channel path through the GDL— a process further detailed in Figure 50 *c) and d)*.

Figure 46 illustrates the distribution of gas volume fraction within sections of the GDL, highlighting areas of gas accumulation and liquid bypass flow. The x-direction component of the mixture velocity is presented in Figure 47 , where negative values confirm the bypass flow through the GDL beneath the bipolar plate in specific regions. This effect diminishes as the gas progresses along the channel due to a decreasing pressure gradient between adjacent channels, as depicted in Figure 50 *c) and d)*.

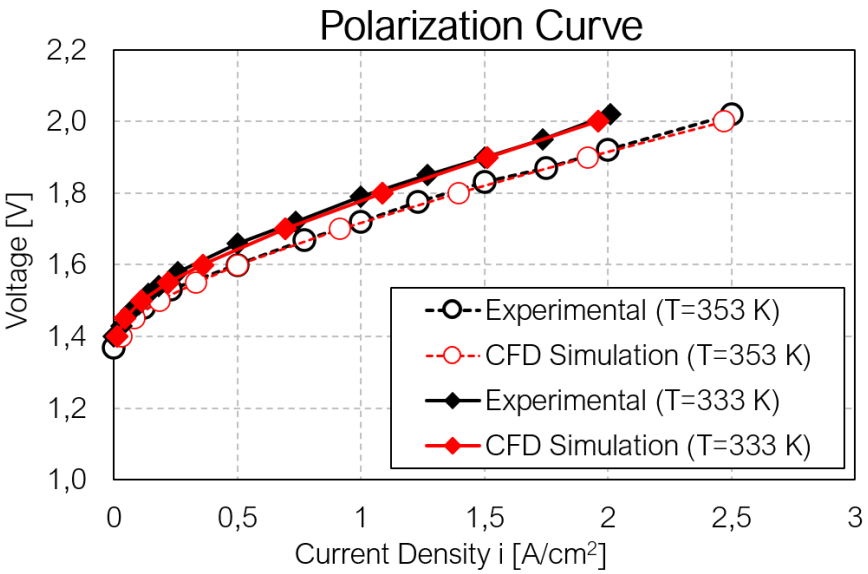

Figure 43 - Polarization curves for 333 K and 353 K operation.

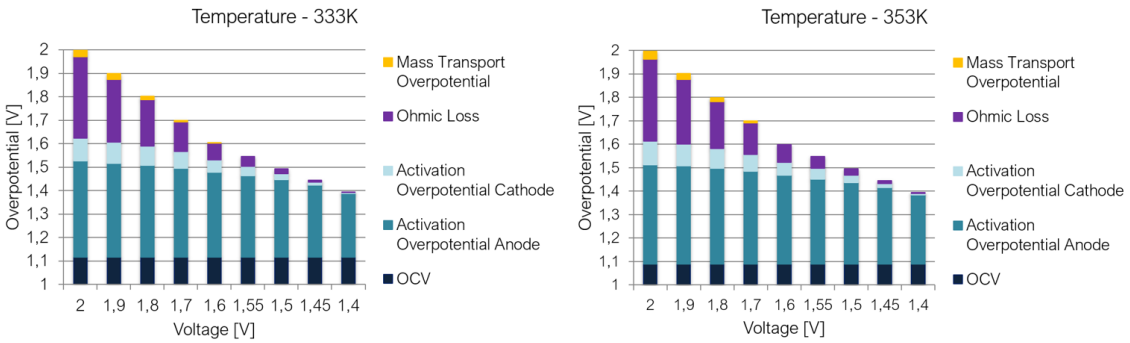

Figure 44 - Overpotentials break-up analysis for 333 K and 353 K.

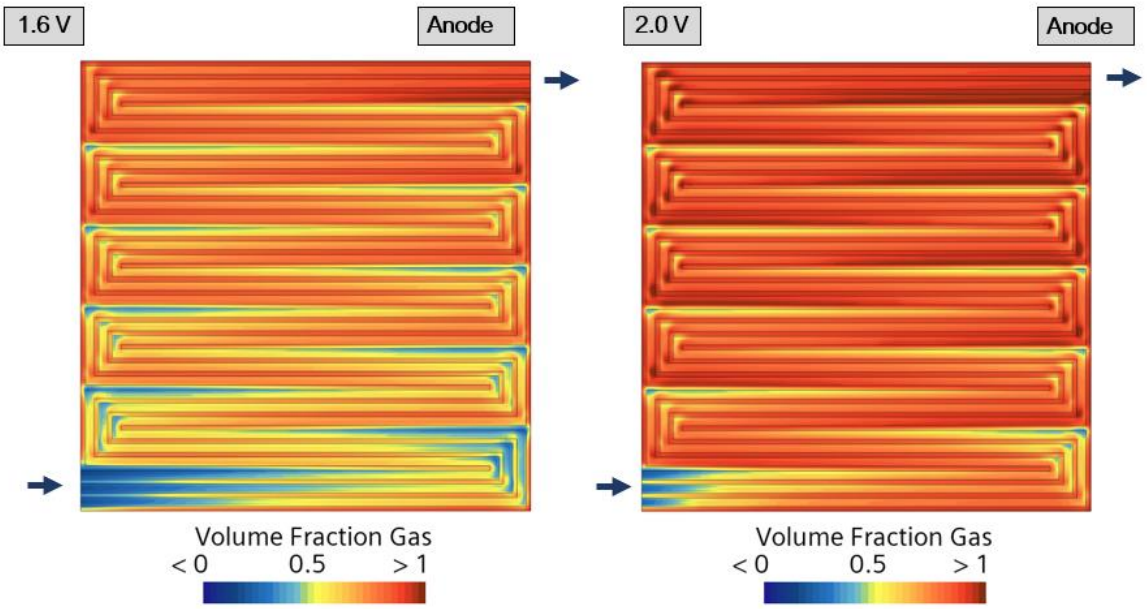

Figure 45 - Volume fraction of gas in the GDL/anode channel interface (353 K).

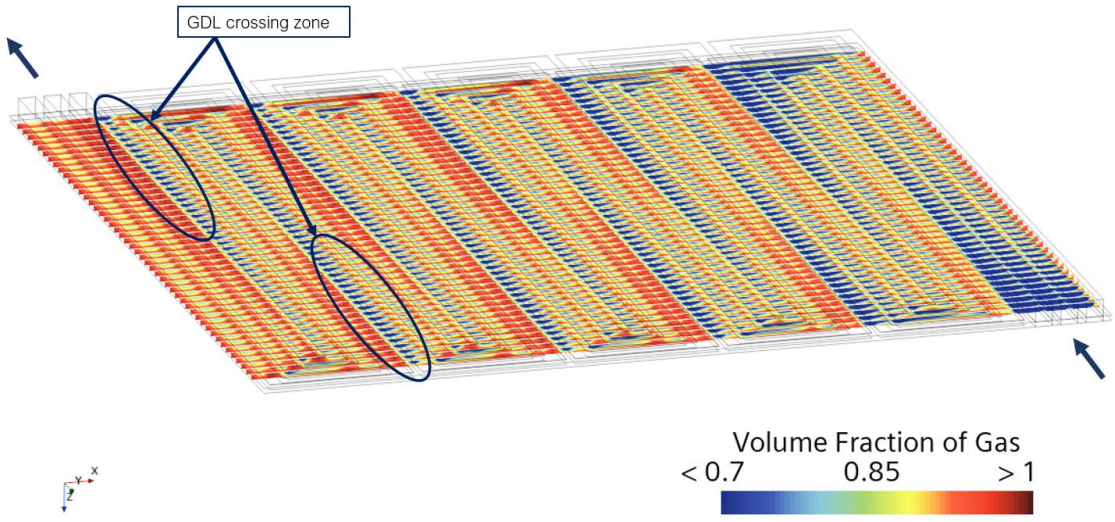

Figure 46 - Volume fraction of gas in the anode gas diffusion layer sections (353 K).

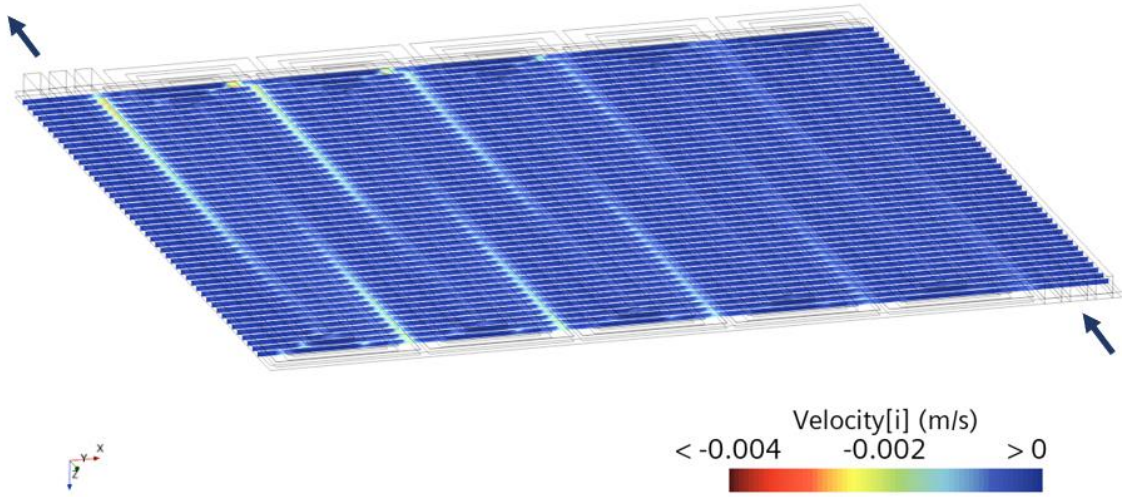

Figure 47 - Mixture velocity in x-direction in the anode gas diffusion layer sections (353 K).

To deepen the understanding of how gas-phase products influence cell performance, the analysis of the gaseous volume fraction is extended to include the gas channels. The substantial specific volume of these gases alters the volumetric flow rate, thereby affecting the flow regime within the cell. Figure 48 presents the distribution of gas volume fraction on both the anodic and cathodic sides at operating voltages of 1.6 V and 2.0 V. As the voltage increases, indicating higher electrical power input, the production of oxygen and hydrogen intensifies. This elevated gas production leads to an accumulation toward the outlet of the electrolysis cell. Since reactions occur across the entire active surface, removing gas from the catalyst layers (CLs) and gas diffusion layers (GDLs) becomes increasingly challenging.

The more pronounced presence of gas on the cathode side is attributed to its lower inlet flow rate, as specified in Table 15, which promotes gas-phase buildup. Figure 49 illustrates the gas volume fraction in transverse sections, highlighting the local stratification of gas within the anodic CL and GDL. This stratification results in the gradual filling of channels along the flow path, potentially impacting the efficiency of the gas removal process.

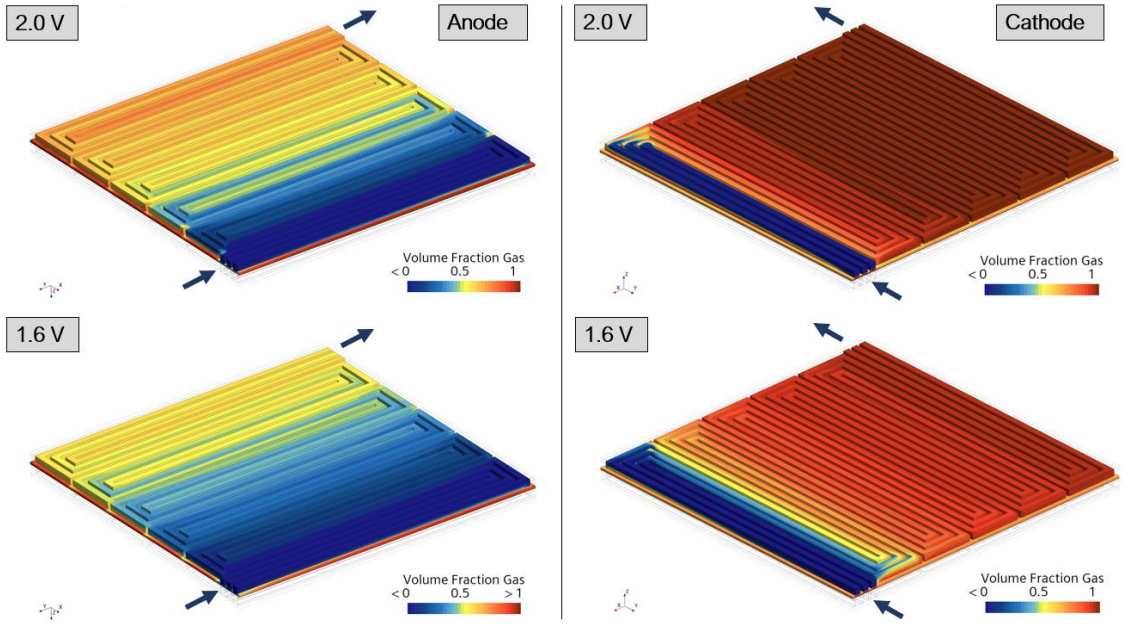

Figure 48 - Volume fraction of gas in the anode and cathode side for three operating voltages (353 K).

An intriguing consequence of the multiphase flow nature in a Proton Exchange Membrane Electrolysis Cell (PEMEC) is the production of gas phases and the resultant reduction in liquid fraction. This reduction leads to a lower mixture density, which induces flow acceleration to maintain the mass flow rate. Figure 50 *a) and b)* display the velocity distributions at operating voltages of 1.6 V and 2.0 V, respectively. The higher voltage of 2.0 V results in increased flow velocities due to greater gas production. This acceleration causes an increased pressure drop, as shown in Figure 50 *c) and d),* for high-voltage operation, leading to higher energy requirements for the water pumps.

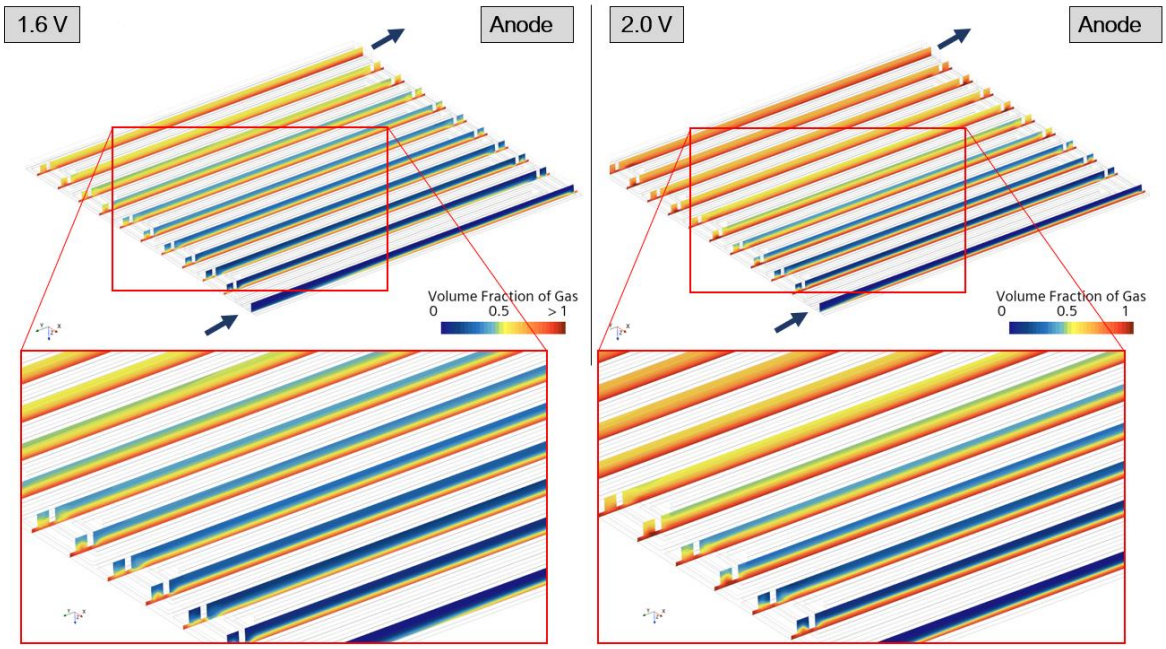

Figure 49 - Gas phase stratification on the anodic CL surface for 1.6 V (left) and 2.0 V (right) operation (353 K).

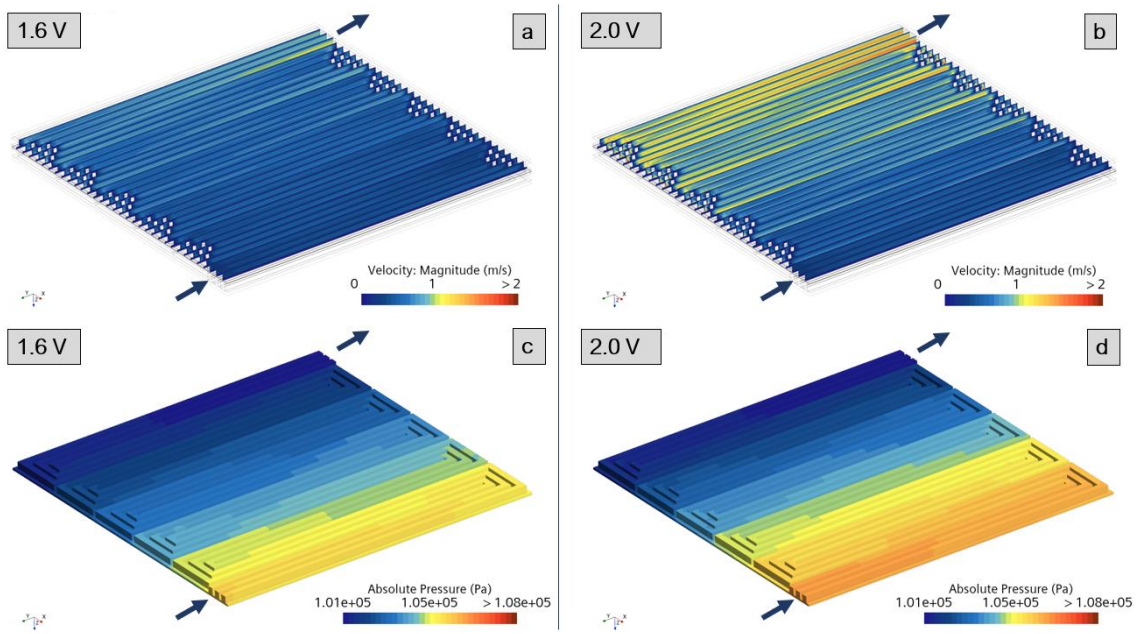

Figure 50 - a) and b) Velocity magnitude field in sections along the channels, c) and d) Absolute pressure field in the anode side (353 K).

Figure 51 illustrates the temperature distribution at the interface between the gas diffusion layer (GDL) and the anode-side channels. The average temperature rises with increasing operating voltage because of the higher amount of power dissipated by the cell. Notably,

areas of maximum temperature coincide with regions of maximum gas volume fraction shown earlier in *Figure 45*.

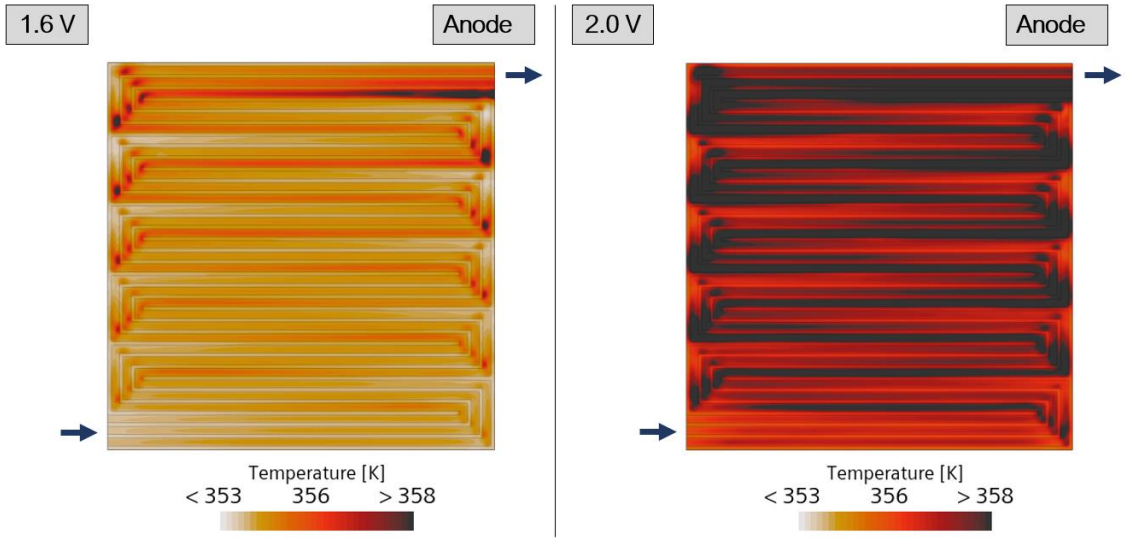

Figure 51 - Temperature in the GDL/anode channel interface (353 K).

To complete the validation of the modelling methodology, the hydrogen production rate ($\dot{m}_{H_2}$) obtained from the 3D-CFD simulations is compared with the theoretical value predicted by Faraday's law of electrolysis (Eq. 92). The results, presented in Figure 51, confirm that the correct amount of hydrogen is produced at all voltages and temperatures, thereby reinforcing the accuracy of the CFD-based detailed analysis discussed in previous sections. Finally, the PEMEC efficiency (η), calculated as per Equation 93, is shown in Figure 52.

$$\dot{m}_{H_2} = \frac{M_{H_2} \cdot P_e}{2 \cdot V_{cell} \cdot F} \qquad \text{Eq. 92}$$

$$\eta = \frac{\dot{m}_{H_2} \cdot LHV_{H_2}}{P_{el}} \qquad \text{Eq. 93}$$

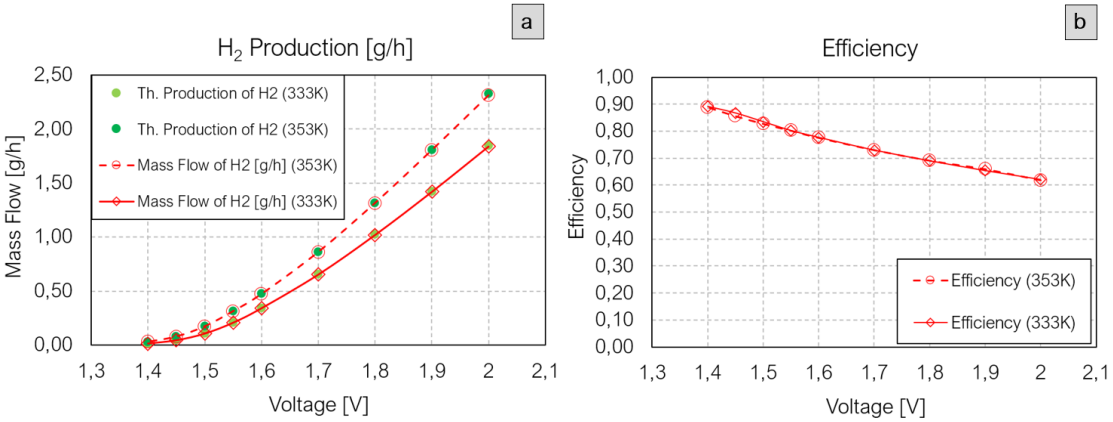

Figure 52 - a) Hydrogen production rate at the cathode [g/h], b) efficiency of the electrolysis cell.

6.3 Conclusions

An in-house developed model for macro-homogeneous catalyst layers is applied to PEM electrolysis. This approach enables the deconstruction of contributions to overpotentials and their dependence on temperature, as well as providing detailed insights into gas-liquid stratification from cell inlet to outlet and the variation of flow regimes due to gas-phase generation. The polarization curves are validated against experimental results, and the hydrogen production rates align with theoretically calculated values across all voltages and temperatures.

This study presents a validated, comprehensive, multi-dimensional model for PEM electrolysis simulation, offering an industry-relevant and ready-to-use methodology for investigating the interaction between fluid dynamics and electrochemical phenomena in PEM electrolysers.

7 Final Remarks and Perspectives

This research represents a significant advancement in understanding and numerically modelling PEM fuel cells and PEM electrolyzers, offering a comprehensive and highly flexible three-dimensional framework for analyzing the involved phenomena. While building on a well-established state of the art, the innovative aspect of this thesis lies in the integrated consideration of multiphase models, electrochemical phenomena, mechanical deformation of porous materials, and full-scale thermal management. By coherently combining these various elements, the work transcends traditional analyses—often constrained to simplified conditions—and provides a more systemic view aligned with real-world engineering challenges.

The usefulness of this study emerges on multiple levels. From an applied perspective, the ability to more accurately predict electrochemical and fluid-dynamic behavior, accounting for compression effects and thermal management, assists engineers in developing devices that are more efficient, reliable, and durable. This leads to more rational design approaches, reducing both development time and cost by decreasing the need for extensive experimental testing, and enabling the fine-tuning of key parameters (such as channel-to-rib ratios, cooling circuit geometries, or the structural properties of porous media). Moreover, the application of these modelling methodologies to large-scale cells and complex configurations ensures that the findings can be readily translated to the industrial context, a critical factor for clean energy technologies.

From a scientific perspective, the integrated approach adopted here constitutes an original methodological contribution. The use of a macro-homogeneous model for the catalyst layers, combined with three-dimensional multiphase simulations and mechanical deformation correlations for porous materials, enables the precise isolation, quantification, and understanding of individual contributions to overpotentials and limiting phenomena. This capability is crucial not only for enhancing the performance of current technologies but also for guiding future innovation in materials, device architectures, and system-level control strategies.

In conclusion, this work goes beyond merely describing modelling methodologies, offering an integrated framework to holistically address the complexities of PEM fuel cells and electrolyzers. In doing so, it provides a valuable tool for directing both fundamental research toward new scientific horizons and industrial development toward more competitive and sustainable products in a sector that is strategic for the energy transition. These insights set the stage for future explorations and refinements, encouraging ongoing dialogue and investigation, and thus providing a fertile ground for future perspectives and ongoing innovation in the field.

Nomenclature

a: activity

BP: Bipolar Plate

c: concentration [mol m^{-3}]

C_p: specific heat [J kg^{-1} K^{-1}]

CL: Catalyst Layer

CFD: Computational Fluid Dynamics

D: diffusivity [m^2 s^{-1}]

EW: Equivalent molecular weight of dry membrane [kg mol^{-1}]

F: Faraday constant [C mol^{-1}]

$\bar{\boldsymbol{f}}$: force [N]

FCEV: Fuel Cell Electric Vehicle

G: Gibbs free energy [J mol^{-1}]

GDL: Gas Diffusion Layer

HOR: hydrogen oxidation reaction

i: current density [A m^2]

j: volumetric current [A m^{-3}]

K: permeability [m^2]

k: thermal conductivity [W m^{-1} K^{-1}]

M: millions

MPL: Microporous layer

n_d: electro-osmotic drag coefficient [H_2O/H^+]

ORR: oxygen reduction reaction

p: pressure [Pa]

PEM: Proton Exchange Membrane

PEMEC: Proton Exchange Membrane Electrolysis Cell

PEMFC: Proton Exchange Membrane Fuel Cell

R: universal gas constant [J mol^{-1} K^{-1}]

RH: Relative humidity

S: entropy, source terms

T: temperature [K]

$\bar{\boldsymbol{u}}$: velocity [m s^{-1}]

Greek Symbols

α: charge transfer coefficient; volume fraction

γ: pressure scaling coefficients; membrane water absorption/desorption rate [s^{-1}]

δ: thickness [m]

ε: porosity

ζ: specific active surface of the catalyst [m^{-1}]

η: overpotential [V]

θ: contact angle [°]

κ: electric conductivity [S m^{-1}]

λ: water content

μ: dynamic viscosity [kg m^{-1} s^{-1}]

ρ: density [kg m^{-3}]

σ: ionic conductivity [S m^{-1}]; surface tension [N m^{-1}]

τ: tortuosity

φ: potential [V]

Subscripts and superscripts

a: anode

c: cathode

d: dissolved water phase

e: electrolyte

eff: effective

eq: equilibrium

g: gas

gd: phase transfer between gas and dissolved phase

i: ionomer

in: inertial

l: liquid

ld: phase transfer between liquid and dissolved phase

m: membrane

n: the n*th* phase

p: porous

pt: platinum

ref: reference

rl: relative

s: solid

sat: saturation

v: viscous

w: water

8 Bibliography

[1] Barbir, F. (2012). *PEM fuel cells: theory and practice*. Academic press.

[2] d'Adamo, A., Haslinger, M., Corda, G., Höflinger, J., Fontanesi, S., & Lauer, T. (2021). Modelling methods and validation techniques for CFD simulations of PEM fuel cells. *Processes*, *9*(4), 688.

[3] Versteeg, H. K. (2007). *An introduction to computational fluid dynamics the finite volume method, 2/E*. Pearson Education India.

[4] Ferziger, J. H. (2002). Computational methods for fluid dynamics.

[5] Darwish, F. M. L. M. M. (2016). *The finite volume method in computational fluid dynamics*.

[6] Yeoh, G. H., & Tu, J. (2019). *Computational techniques for multiphase flows*. Butterworth-Heinemann.

[7] Carcadea, E., Varlam, M., Marinoiu, A., Raceanu, M., Ismail, M. S., & Ingham, D. B. (2019). Influence of catalyst structure on PEM fuel cell performance–A numerical investigation. *International Journal of Hydrogen Energy*, *44*(25), 12829-12841.

[8] Tabuchi, Y., Kotaka, T., & Wang, C. Y. (2013). Multi-physics numerical analysis of PEMFC for automobile application. *SAE International Journal of Alternative Powertrains*, *2*(1), 68-73.

[9] Nie, J., & Chen, Y. (2010). Numerical modeling of three-dimensional two-phase gas–liquid flow in the flow field plate of a PEM electrolysis cell. *International Journal of Hydrogen Energy*, *35*(8), 3183-3197.

[10] Patankar, S. (2018). *Numerical heat transfer and fluid flow*. CRC press.

[11] Toghyani, S., Baniasadi, E., & Afshari, E. (2019). Numerical simulation and exergoeconomic analysis of a high temperature polymer exchange membrane electrolyzer. *International Journal of Hydrogen Energy*, *44*(60), 31731-31744.

[12] Toghyani, S., Afshari, E., Baniasadi, E., & Atyabi, S. A. (2018). Thermal and electrochemical analysis of different flow field patterns in a PEM electrolyzer. *Electrochimica acta*, *267*, 234-245.

[13] Toghyani, S., Afshari, E., & Baniasadi, E. (2019). Three-dimensional computational fluid dynamics modeling of proton exchange membrane electrolyzer with new flow field pattern. *Journal of Thermal Analysis and Calorimetry*, *135*, 1911-1919.

[14] Sasmito, A. P., Birgersson, E., & Mujumdar, A. S. (2012). A novel flow reversal concept for improved thermal management in polymer electrolyte fuel cell stacks. *International Journal of Thermal Sciences*, *54*, 242-252.

[15] Alizadeh, E., Rahgoshay, S. M., Rahimi-Esbo, M., Khorshidian, M., & Saadat, S. H. M. (2016). A novel cooling flow field design for polymer electrolyte membrane fuel cell stack. *International Journal of Hydrogen Energy*, *41*(20), 8525-8532.

[16] Hirsch, C. (2007). *Numerical computation of internal and external flows: The fundamentals of computational fluid dynamics*. Elsevier.

[17] Toro, E. F. (2013). *Riemann solvers and numerical methods for fluid dynamics: a practical introduction*. Springer Science & Business Media.

[18] Berger, M. J., & Colella, P. (1989). Local adaptive mesh refinement for shock hydrodynamics. *Journal of computational Physics*, *82*(1), 64-84.

[19] Blazek, J. (2015). *Computational Fluid Dynamics: Principles and Applications* (3rd ed.). Elsevier.

[20] Succi, S. (2001). *The Lattice Boltzmann Equation for Fluid Dynamics and Beyond*. Oxford University Press.

[21] Ishii, M., & Hibiki, T. (2010). *Thermo-fluid dynamics of two-phase flow*. Springer Science & Business Media.

[22] Yeoh, G. H., & Tu, J. (2019). *Computational techniques for multiphase flows*. Butterworth-Heinemann.

[23] Manninen, M., Taivassalo, V., & Kallio, S. (1996). On the mixture model for multiphase flow.

[24] Zhang, G., & Jiao, K. (2018). Three-dimensional multi-phase simulation of PEMFC at high current density utilizing Eulerian-Eulerian model and two-fluid model. *Energy Conversion and Management*, *176*, 409-421.

[25] ANSYS Inc. (2013). *ANSYS Fluent Theory Guide*.

[26] Weber, A. Z., & Newman, J. (2004). Modeling transport in polymer-electrolyte fuel cells. *Chemical reviews*, *104*(10), 4679-4726.

[27] Wang, Y., Chen, K. S., Mishler, J., Cho, S. C., & Adroher, X. C. (2011). A review of polymer electrolyte membrane fuel cells: Technology, applications, and needs on fundamental research. *Applied energy*, *88*(4), 981-1007.

[28] Pasaogullari, U., & Wang, C. Y. (2005). Two-phase modeling and flooding prediction of polymer electrolyte fuel cells. *Journal of the Electrochemical Society*, *152*(2), A380.

[29] Berning, T., & Djilali, N. (2003). Three-dimensional computational analysis of transport phenomena in a PEM fuel cell—a parametric study. *Journal of Power Sources*, *124*(2), 440-452.

[30] Rao, R. M., Bhattacharyya, D., Rengaswamy, R., & Choudhury, S. R. (2007). A two-dimensional steady state model including the effect of liquid water for a PEM fuel cell cathode. *Journal of Power Sources*, *173*(1), 375-393.

[31] Gostick, J. T., Fowler, M. W., Pritzker, M. D., Ioannidis, M. A., & Behra, L. M. (2006). In-plane and through-plane gas permeability of carbon fiber electrode backing layers. *Journal of Power sources*, *162*(1), 228-238.

[32] Fuller, T. F., & Newman, J. (1993). Water and thermal management in solid-polymer-electrolyte fuel cells. *Journal of the Electrochemical Society*, *140*(5), 1218.

[33] Wang, Y., & Wang, C. Y. (2006). A nonisothermal, two-phase model for polymer electrolyte fuel cells. *Journal of the electrochemical society*, *153*(6), A1193.

[34] Meng, H., & Wang, C. Y. (2005). Model of two-phase flow and flooding

dynamics in polymer electrolyte fuel cells. *Journal of the Electrochemical Society*, *152*(9), A1733.

[35] Li, H., Tang, Y., Wang, Z., Shi, Z., Wu, S., Song, D., ... & Mazza, A. (2008). A review of water flooding issues in the proton exchange membrane fuel cell. *Journal of Power Sources*, *178*(1), 103-117.

[36] Ishii, M., & Hibiki, T. (2010). *Thermo-fluid dynamics of two-phase flow*. Springer Science & Business Media.

[37] Hirt, C. W., & Nichols, B. D. (1981). Volume of fluid (VOF) method for the dynamics of free boundaries. *Journal of computational physics*, *39*(1), 201-225.

[38] Wang, Y., Basu, S., & Wang, C. Y. (2008). Modeling two-phase flow in PEM fuel cell channels. *Journal of Power Sources*, *179*(2), 603-617.

[39] Brackbill, J. U., Kothe, D. B., & Zemach, C. (1992). A continuum method for modeling surface tension. *Journal of computational physics*, *100*(2), 335-354.

[40] Rider, W. J., & Kothe, D. B. (1998). Reconstructing volume tracking. *Journal of computational physics*, *141*(2), 112-152.

[41] Noh, W. F., & Woodward, P. (2005, July). SLIC (simple line interface calculation). In *Proceedings of the fifth international conference on numerical methods in fluid dynamics June 28–July 2, 1976 Twente University, Enschede* (pp. 330-340). Berlin, Heidelberg: Springer Berlin Heidelberg.

[42] Tryggvason, G., Scardovelli, R., & Zaleski, S. (2011). *Direct numerical simulations of gas–liquid multiphase flows*. Cambridge university press.

[43] Lopez, J., Hernandez, J., Gomez, P., & Faura, F. (2005). An improved PLIC-VOF method for tracking thin fluid structures in incompressible two-phase flows. *Journal of Computational Physics*, *208*(1), 51-74.

[44] Rudman, M. (1997). Volume-tracking methods for interfacial flow calculations. *International journal for numerical methods in fluids*, *24*(7), 671-691.

[45] Lv, X., Zou, Q., & Reeve, D. (2011). Numerical simulation of overflow at vertical weirs using a hybrid level set/VOF method. *Advances in Water*

Resources, *34*(10), 1320-1334.

[46] Wang, Y., & Chen, K. S. (2013). *PEM fuel cells: thermal and water management fundamentals*. Momentum press.

[47] Bazylak, A. (2009). Liquid water visualization in PEM fuel cells: A review. *International journal of hydrogen energy*, *34*(9), 3845-3857.

[48] Leverett, M. (1941). Capillary behavior in porous solids. *Transactions of the AIME*, *142*(01), 152-169.

[49] Carcadea, E., Varlam, M., Ismail, M., Ingham, D. B., Marinoiu, A., Raceanu, M., ... & Ion-Ebrasu, D. (2020). PEM fuel cell performance improvement through numerical optimization of the parameters of the porous layers. *International Journal of Hydrogen Energy*, *45*(14), 7968-7980.

[50] Adamson, A. W., & Gast, A. P. (1967). *Physical chemistry of surfaces* (Vol. 150, p. 180). New York: Interscience publishers.

[51] Gennes, P. G., Brochard-Wyart, F., & Quéré, D. (2004). *Capillarity and wetting phenomena: drops, bubbles, pearls, waves* (pp. 7-9). Springer New York.

[52] Natarajan, D., & Van Nguyen, T. (2003). Three-dimensional effects of liquid water flooding in the cathode of a PEM fuel cell. *Journal of power sources*, *115*(1), 66-80.

[53] Das, P. K., Li, X., & Liu, Z. S. (2010). Effective transport coefficients in PEM fuel cell catalyst and gas diffusion layers: Beyond Bruggeman approximation. *Applied Energy*, *87*(9), 2785-2796.

[54] Looyenga, H. (1965). Dielectric constants of heterogeneous mixtures. *Physica*, *31*(3), 401-406.

[55] Bruggeman, V. D. (1935). Berechnung verschiedener physikalischer Konstanten von heterogenen Substanzen. I. Dielektrizitätskonstanten und Leitfähigkeiten der Mischkörper aus isotropen Substanzen. *Annalen der physik*, *416*(7), 636-664.

[56] Zamel, N., Li, X., & Shen, J. (2012). Numerical estimation of the effective electrical conductivity in carbon paper diffusion media. *Applied Energy*, *93*, 39-44.

[57] Springer, T. E., Zawodzinski, T. A., & Gottesfeld, S. (1991). Polymer electrolyte fuel cell model. *Journal of the electrochemical society*, *138*(8), 2334.

[58] Tabuchi, Y., Shiomi, T., Aoki, O., Kubo, N., & Shinohara, K. (2010). Effects of heat and water transport on the performance of polymer electrolyte membrane fuel cell under high current density operation. *Electrochimica Acta*, *56*(1), 352-360.

[59] Kulikovsky, A. A. (2019). *Analytical modelling of fuel cells*. Elsevier.

[60] Bear, J. (2013). *Dynamics of fluids in porous media*. Courier Corporation.

[61] Tamayol, A., & Bahrami, M. (2011). In-plane gas permeability of proton exchange membrane fuel cell gas diffusion layers. *Journal of Power Sources*, *196*(7), 3559-3564.

[62] Tamayol, A., McGregor, F., & Bahrami, M. (2012). Single phase through-plane permeability of carbon paper gas diffusion layers. *Journal of Power Sources*, *204*, 94-99.

[63] Tomadakis, M. M., & Robertson, T. J. (2005). Viscous permeability of random fiber structures: comparison of electrical and diffusional estimates with experimental and analytical results. *Journal of Composite Materials*, *39*(2), 163-188.

[64] Van Doormaal, M. A., & Pharoah, J. G. (2009). Determination of permeability in fibrous porous media using the lattice Boltzmann method with application to PEM fuel cells. *International journal for numerical methods in fluids*, *59*(1), 75-89.

[65] You, L., & Liu, H. (2001). A parametric study of the cathode catalyst layer of PEM fuel cells using a pseudo-homogeneous model. *International Journal of Hydrogen Energy*, *26*(9), 991-999.

[66] Hao, L., & Cheng, P. (2009). Lattice Boltzmann simulations of anisotropic permeabilities in carbon paper gas diffusion layers. *Journal of Power Sources*, *186*(1), 104-114.

[67] Eikerling, M., & Kornyshev, A. (1998). Modelling the performance of the cathode catalyst layer of polymer electrolyte fuel cells. *Journal of Electroanalytical Chemistry*, *453*(1-2), 89-106.

[68] Xing, L., Liu, X., Alaje, T., Kumar, R., Mamlouk, M., & Scott, K. (2014). A two-phase flow and non-isothermal agglomerate model for a proton exchange membrane (PEM) fuel cell. *Energy*, *73*, 618-634.

[69] Khajeh-Hosseini-Dalasm, N., Fesanghary, M., Fushinobu, K., & Okazaki, K. (2012). A study of the agglomerate catalyst layer for the cathode side of a proton exchange membrane fuel cell: Modeling and optimization. *Electrochimica Acta*, *60*, 55-65.

[70] Xing, L. (2018). An agglomerate model for PEM fuel cells operated with non-precious carbon-based ORR catalysts. *Chemical Engineering Science*, *179*, 198-213.

[71] Chen, W. H., Tu, Y. J., & Sheen, H. K. (2010). Impact of dilute acid pretreatment on the structure of bagasse for bioethanol production. *International Journal of Energy Research*, *34*(3), 265-274.

[72] Nam, J. H., & Kaviany, M. (2003). Effective diffusivity and water-saturation distribution in single-and two-layer PEMFC diffusion medium. *International Journal of Heat and Mass Transfer*, *46*(24), 4595-4611.

[73] Zhang, J., Tang, Y., Song, C., Xia, Z., Li, H., Wang, H., & Zhang, J. (2008). PEM fuel cell relative humidity (RH) and its effect on performance at high temperatures. *Electrochimica Acta*, *53*(16), 5315-5321.

[74] Sun, W., Peppley, B. A., & Karan, K. (2005). An improved two-dimensional agglomerate cathode model to study the influence of catalyst layer structural parameters. *Electrochimica acta*, *50*(16-17), 3359-3374.

[75] Song, C., Tang, Y., Zhang, J. L., Zhang, J., Wang, H., Shen, J., ... & Kozak, P. (2007). PEM fuel cell reaction kinetics in the temperature range of 23–120 C. *Electrochimica Acta*, *52*(7), 2552-2561.

[76] Ju, H., Luo, G., & Wang, C. Y. (2006). Probing liquid water saturation in diffusion media of polymer electrolyte fuel cells. *Journal of the Electrochemical Society*, *154*(2), B218.

[77] Wu, H., Li, X., & Berg, P. (2009). On the modeling of water transport in polymer electrolyte membrane fuel cells. *Electrochimica Acta*, *54*(27), 6913-6927.

[78] Carcadea, E., Varlam, M., Ingham, D. B., Ismail, M. S., Patularu, L., Marinoiu, A., & Schitea, D. (2018). The effects of cathode flow channel size and operating conditions on PEM fuel performance: A CFD modelling study and experimental demonstration. *International Journal of Energy Research*, *42*(8), 2789-2804.

[79] Ferreira, R. B., Falcão, D. S., Oliveira, V. B., & Pinto, A. M. (2017). 1D+ 3D two-phase flow numerical model of a proton exchange membrane fuel cell. *Applied Energy*, *203*, 474-495.

[80] Wu, H., Li, X., & Berg, P. (2009). On the modeling of water transport in polymer electrolyte membrane fuel cells. *Electrochimica Acta*, *54*(27), 6913-6927.

[81] Choopanya, P., & Yang, Z. (2016). An effective mesh strategy for CFD modelling of polymer electrolyte membrane fuel cells. *International Journal of Hydrogen Energy*, *41*(15), 6445-6456.

[82] Nitta, I., Hottinen, T., Himanen, O., & Mikkola, M. (2007). Inhomogeneous compression of PEMFC gas diffusion layer: Part I. Experimental. *Journal of Power Sources*, *171*(1), 26-36.

[83] Hottinen, T., Himanen, O., Karvonen, S., & Nitta, I. (2007). Inhomogeneous compression of PEMFC gas diffusion layer: part II. Modeling the effect. *Journal of Power Sources*, *171*(1), 113-121.

[84] Wang, C. Y. (2004). Fundamental models for fuel cell engineering. *Chemical reviews*, *104*(10), 4727-4766.

[85] Iranzo, A., Gregorio, J. M., Boillat, P., & Rosa, F. (2020). Bipolar plate research using Computational Fluid Dynamics and neutron radiography for proton exchange membrane fuel cells. *International Journal of Hydrogen Energy*, *45*(22), 12432-12442.

[86] D'Adamo, A., Riccardi, M., Locci, C., Romagnoli, M., & Fontanesi, S. (2020). *Numerical simulation of a high current density PEM fuel cell* (No. 2020-24-0016). SAE Technical Paper.

[87] Baek, S. M., Yu, S. H., Nam, J. H., & Kim, C. J. (2011). A numerical study on uniform cooling of large-scale PEMFCs with different coolant flow field

designs. *Applied Thermal Engineering*, *31*(8-9), 1427-1434.

[88] Yu, S. H., Sohn, S., Nam, J. H., & Kim, C. J. (2009). Numerical study to examine the performance of multi-pass serpentine flow-fields for cooling plates in polymer electrolyte membrane fuel cells. *Journal of Power Sources*, *194*(2), 697-703.

[89] Ma, Z., Witteman, L., Wrubel, J. A., & Bender, G. (2021). A comprehensive modeling method for proton exchange membrane electrolyzer development. *International Journal of Hydrogen Energy*, *46*(34), 17627-17643.